Impact of macro-turbulent structures from mooring anchors and rough riverbeds on the performance of a horizontal axis hydrokinetic turbine

by

Sixtus C. Ekezie

A Thesis Submitted to the Faculty of Graduate Studies of
the University of Manitoba
in Partial Fulfilment of the Requirements of the Degree of

MASTER OF SCIENCE

Department of Mechanical Engineering
The University of Manitoba
Winnipeg

Copyright © Sixtus C. Ekezie. 2018. All rights reserved.

Abstract

Reported are laboratory and field measurements obtained to characterize the flow structures caused by mooring anchors and rough river beds on the performance of hydrokinetic turbines. Series of flow velocity profile in-situ measurements characterize the energetic flow at the Canadian Hydrokinetic Turbine Test Centre (CHTTC) located on the Winnipeg River. Using an acoustic doppler velocimeter, a novel method was applied to obtain the flow velocity through the water column to contribute in the design and optimization of power production from a hydrokinetic turbine. The acoustic doppler velocimeter measures the mean and fluctuating velocity components at a frequency of 64 Hz. Tests were performed between 2.1 and 2.7 m/s upstream and downstream of turbine mooring anchors. Anchors occupy 12% of the water column height. Near surface measurements shows a 9.9% increase in turbulence intensity and 8.8% increase in free-stream velocity due to the upstream turbine mooring structures while the profile measurements show a temporal variation in the velocity and turbulence intensity profiles. In a more detailed laboratory investigation, four different scaled geometries of turbine mooring anchors were designed, fabricated and tested, including a 19.8 cm diameter horizontal axis turbine in a water tunnel. Tests are first performed at a steady velocity of 1.1 m/s and at an unobstructed Reynolds number of 2.17×10^5 based on rotor diameter. During this testing, velocity measurements were taken at different locations upstream of a scaled horizontal turbine to determine the optimum operating conditions in a steady free-stream velocity. Furthermore, 25 surface roughness and four mooring anchor geometries were tested and located 2 and 3 rotor diameter upstream of the turbine in the water tunnel. Results show a 14% to 36% increase in turbine performance due to the impact of mooring anchor geometries and surface roughness. These results are useful in choosing a turbine mooring anchor design, geometry, and location to enhance turbine

performance and obtain an understanding of a rough riverbed at energetic river sites.

Acknowledgements

First, I would like to use this opportunity and medium to thank my advisor, Dr. Eric Bibeau for providing me with this opportunity to complete my thesis, his teaching, patience, and also for allowing me share in his wisdom and experience. I would like to thank Mr. Zeev Kapitanker for his unalloyed support and assistance throughout my research. Mr. Zeev was always there to provide me with every needed tool and assistance both at site and in the laboratory. I would also like to thank Mr. Kirk Dyson for his assistance with safe boat driving during data collection and boat driving teachings at the CHTTC. I would like to thank my colleagues in the research group - Obiajulu Nnaemeka, Samuel d'Auteuil, Jody Soviak, Kaisar Bhuyan, Raul Vaid, Jermaine Hovern for their constructive criticisms, assistance and support throughout this research for a better result. Also, I would like to thank GETS and NSERC discovery for providing the funding for this research.

Contents

List of Tables

List of Figures

Nomenclature

ADV	Acoustic Doppler Velocimetry
CHTTC	Canadian Hydrokinetic Turbine Test Centre
GHG	Green House Gas
HKT	Hydrokinetic Turbine
HAT	Horizontal Axis Turbine
RPM	Revolution Per Minute
VAT	Vertical Axis Turbine
PA	Projected Area
TKE	Turbulent Kinetic Energy
TI	Turbulence Intensity
VAT	Vertical Axis Turbine
H	Height
H_t	Tunnel height
H_r	Rock height
H_a	Anchor height
H_w	Water height
A	Cross sectional area
U, V, W	Instantaneous streamwise, spanwise and vertical velocity, respectively
X, Y, Z	Streamwise, spanwise and vertical directions, respectively
U_∞	Free-stream velocity
R_h	Hydraulic radius
Re	Reynolds number
Fr	Froude number
λ	Tip speed ratio
ρ	Fluid density
ν	Kinematic viscosity
μ	Dynamic viscosity
u, v, w	Fluctuating components of streamwise, spanwise and vertical velocities
$\overline{U}$, $\overline{V}$, $\overline{W}$	Mean streamwise, spanwise and vertical velocities respectively
$\overline{u^2}$, $\overline{v^2}$, $\overline{w^2}$	Reynolds normal stresses
$\overline{uv}$, $\overline{uw}$, $\overline{vw}$	Reynolds shear stresses

Chapter 1

Introduction

Addressing the growing demand for renewable energy is a concern worldwide as the present generation will soon be confronted with a 500 ppm atmospheric CO_2 world, as shown in Figure 1.1. Fossil fuels are major contributors to the increase in atmospheric CO_2. With the world population growing, energy consumption increases yearly [5]. The 18 TW of energy presently consumed is sourced mainly from fossil fuel, which is limited in capacity and non-renewable [6].

Effect of CO_2 emissions such as environmental pollution and greenhouse effect are some of the consequences of relying mainly on fossil fuels [7]. This makes the reduction in the use of fossil fuel a necessity in energy generation and can be achieved by using renewable energy sources [8] resulting in a sustainable future with the majority of the energy portfolio derived from renewable energy sources [9, 10].

Amongst other factors, world population is a significant contributor to high energy demand as it is projected to exceed 8.3 billion in 2030 according to the United Nations secretariat [2]. With this projection, the energy demand of the world will increase from 510 TWh to 678 TWh [11], as illustrated in Figure 1.2.

Thus, with the rate of electrical energy consumption in the world today, it is possible

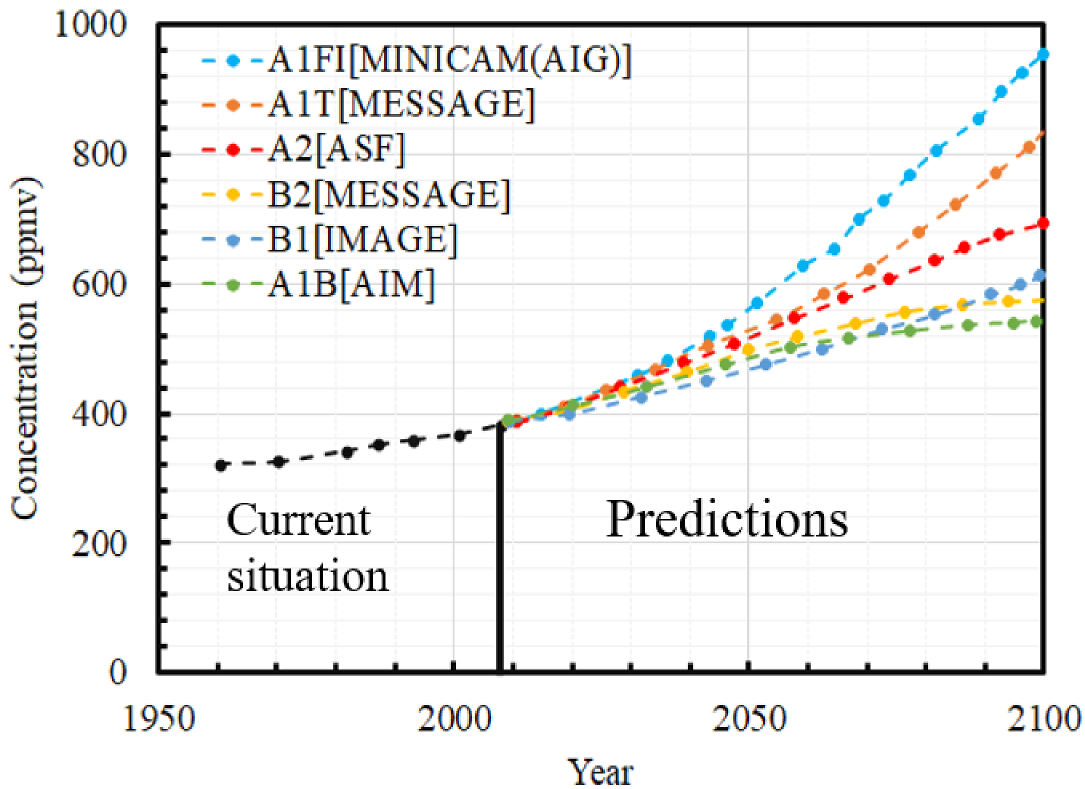

Figure 1.1: Atmospheric CO_2 levels from 1980 to present and projections under the 6 Special Report on Emissions Scenarios marker and illustrative scenarios as reported by Mauna Loa Observatory [1]

that the global fossil fuel reserve becomes depleted in the near future. Hydropower, including hydrokinetic, is a renewable energy resource that can contribute to move away from fossil fuels [5], providing base load power.

1.1 Hydrokinetic energy usage

A hydropower resource which can help in meeting the world's electrical energy demand using renewable is hydrokinetic energy from rivers and tides. Tidal-stream, ocean current and river hydrokinetic are examples of marine energy technologies [5]. Extraction of kinetic energy is achieved using a Hydrokinetic Turbine (HKT) which can be a cross-flow, horizontal or vertical axis type. HKTs uses similar operation

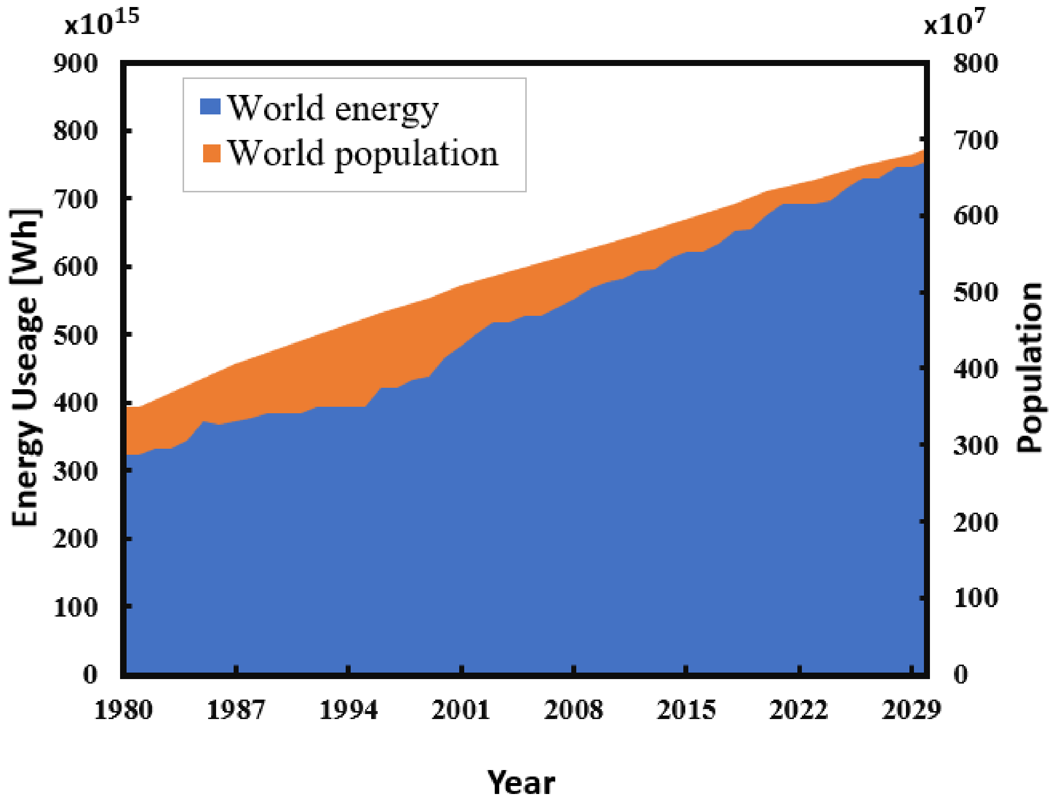

Figure 1.2: World population and energy demand predictions from 1980 to 2029 [2] showing energy demand increases as world population increases

principles of a wind turbine in kinetic energy extraction from water currents, though power generation from HKTs are more predictable compared to wind applications [12]. The slight slope of a river, or the gravitational effect of the moon, provides reliable and predictable power than wind which is caused and affected by atmospheric changes [13]. In contrast to the conventional hydroelectric turbine which generates electricity by converting the potential energy of water in the reservoir of a dam, a HKT generates electricity with potentially less environmental impacts [14]. Micro application of HKT's started more than a century ago when it was used for pumping water and generating electricity in Egypt. Research and development of the technology started in the early 21st century [15] and since then, has spread too many countries across the world including Canada.

Canada is one of many countries in the world that has an abundant hydrokinetic resource. Canada's Marine Renewable Energy Technology Roadmap [16] expects Canada to be a global leader in river current energy production systems. The extractable mean potential resource from hydrokinetic in Canada exceeds the total electrical energy capacity in Canada [17]. A vital element in achieving the marine renewable energy technology vision is to build 2 GW by 2030 power generating capacities which in 2030 will be worth 2 billion dollars [16]. To achieve this, a large portion of the anticipated electrical energy to be generated can be provided from a farm of HKTs [18].

Following the energy crisis in 1970, research on improving the performance of wind turbines began. During this time, researchers focused their attention in improving the design specifications of wind turbines for a better utilization of their working principles with little attention to HKTs. Due to global warming and the environmental impacts created by fossil fuel usage in the twenty-first century, the attention of researchers began focusing on HKTs. Hydrokinetic energy is a predictable resource with relative high energy density that can address base loads. Hence, the desire of Canada and US to commercialize the technology as stated in their recent technological roadmaps [19, 20].

The total hydrokinetic power available, P, is a function of the flow's mean velocity, V, the water density, ρ, the total swept area of the rotor blade area, A, given by

$$P = \frac{1}{2}\rho C_P V^3 A \tag{1.1}$$

where C_P is the coefficient of performance of the selected turbine and a non-linear function of the tip speed ratio: the ratio of the circumferential velocity of the tip of the rotor blade to the velocity of flow given by

$$TSR = \frac{R\omega}{V} \tag{1.2}$$

where R is the radius of the blade, ω is the angular velocity of the turbine, and V is the velocity of the flow. Of the available power, 59% is achievable as derived by Albert Betz [21]. This is known as the Betz limit, which provides a theoretical limit irrespective of turbine design.

1.2 Macro-turbulent structures

River and channel flow patterns are impacted by natural and man-made structures such as bridge piers, bathymetry, rocks, anchor blocks, upstream turbines etc. The impacts caused by these in-stream structures leads to generation of macro-turbulent structures in the flow. Macro-turbulent structures in this research is limited to large scale river flow structures that are over a meter in size and visible when viewed from the surface. Examples of such macro-turbulent structures include eddies, wakes, and boils. Other sources of macro-turbulent structures include profile changes of river bed and banks, ice floes, boulders and other man-made activities in rivers and channels [17]. Studies have shown that macro-turbulent structures affects the performance of HKTs. Example of such is the study by Birjandi [17] who investigated the impact of macro-turbulent structures caused by an upstream cylinder on the performance of a vertical HKT. The study showed that the macro-turbulent structures generated by the upstream cylinder improved the power generated from the turbine. However, this research focuses on 2 structures: mooring anchors and riverbed rocks on the performance of a horizontal HKT.

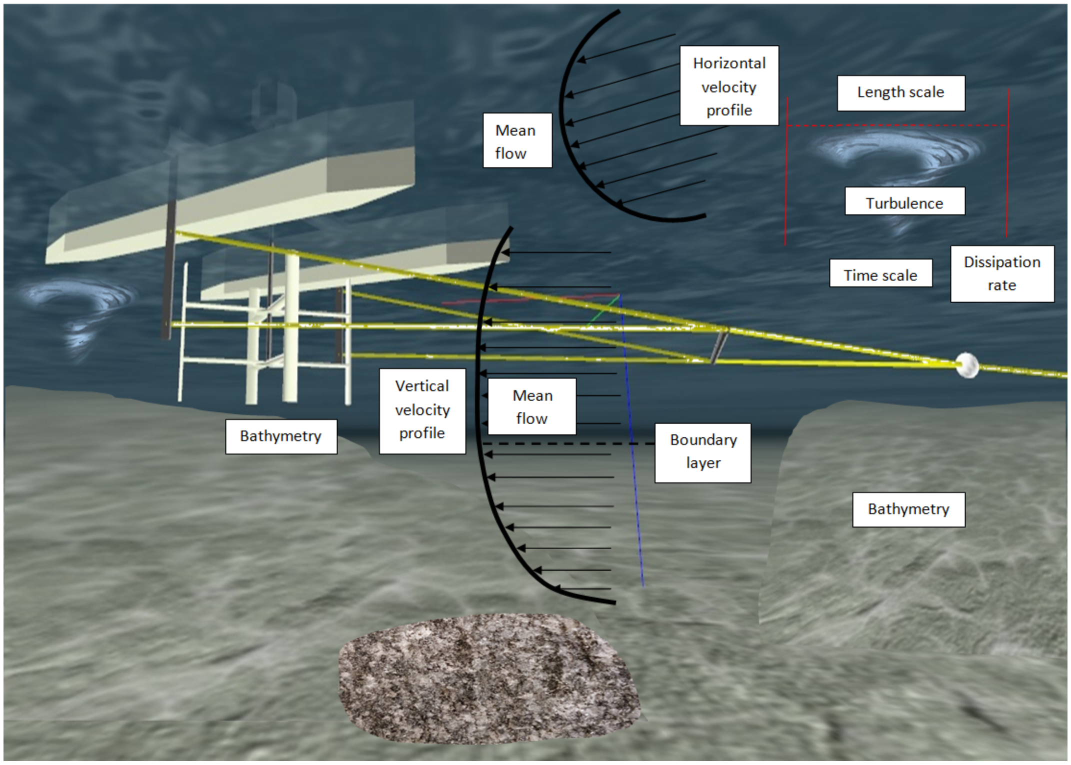

Figure 1.3: Hydrokinetic flow characterization requirements in an energetic flow showing riverine features and the type of flow structures that lead to macro turbulence. Use of figure is permitted by D' Auteuil [3]

1.2.1 Turbine mooring anchors

In high energetic river sites like the Canadian Hydrokinetic Turbine Test Centre (CHTTC), HKTs employ anchor systems for mooring. With studies on turbine development and its power production enhancement methods on the rise, choosing mooring anchors that can keep a turbine in a desired position and contribute to enhancing power generation from the turbine is important. HKTs deployed in the boundary layer or bed of rivers and channels are impacted by boundary layer power loss, which can be attributed to the rivers cross-sectional area or the channel bathymetry. Boundary layer power-loss is not limited to hydrokinetic turbines alone, as wind turbines also experience boundary layer power loss. Though wind turbine heights can be adjusted to mitigate this loss, river and channel depths are fixed. To mitigate this, a technique of using upstream obstructions to alter the flow downstream

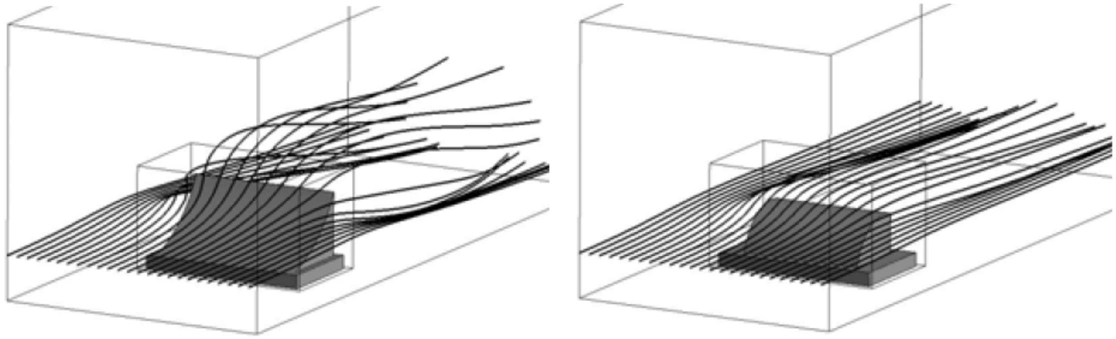

Figure 1.4: Different anchor geometries having different effects on flow velocity as demonstrated by Gaden and Bibeau [4]

can be used in a beneficial manner as proposed by Gaden and Bibeau [4]. Such obstructions can also be used as turbine mooring anchors to keep HKTs in the desired location. Mooring procedures and methods are important factors to consider in the design, manufacture, deployment and operation of a HKT, as the affect various flow components, as shown in Figure 1.3. Furthermore, a study on enhancing flow velocity by Gaden [4] using different shaped anchors showed that different anchor geometries can increase local flow velocity by over 25%. Figure 1.4 shows two examples of anchor geometries used by Gaden [4] and their effects on flow velocity. Results show moorings can increase flow velocity to create more power from a HKT for river application.

The turbine mooring anchors at the CHTTC Site are shown in Figure 1.5. This system comprises of three weight anchor blocks, mooring chains, cables, buoys and a metal ring. The mooring chains and cables, are connected to the shackles on the anchor blocks, to a metal D ring, and to the attachment point at the surface. These buoys are subjected to yearly harsh winter conditions with some of them shearing-off from the mooring cable during the winter season. Figure 1.6 shows a buoy replacement activity at the CHTTC. HKTs deployed at the CHTTC are connected to a mooring cable and moored to the turbine mooring system. The CHTTC is used to test HKTs on river environment. Appendix A details the CHTTC.

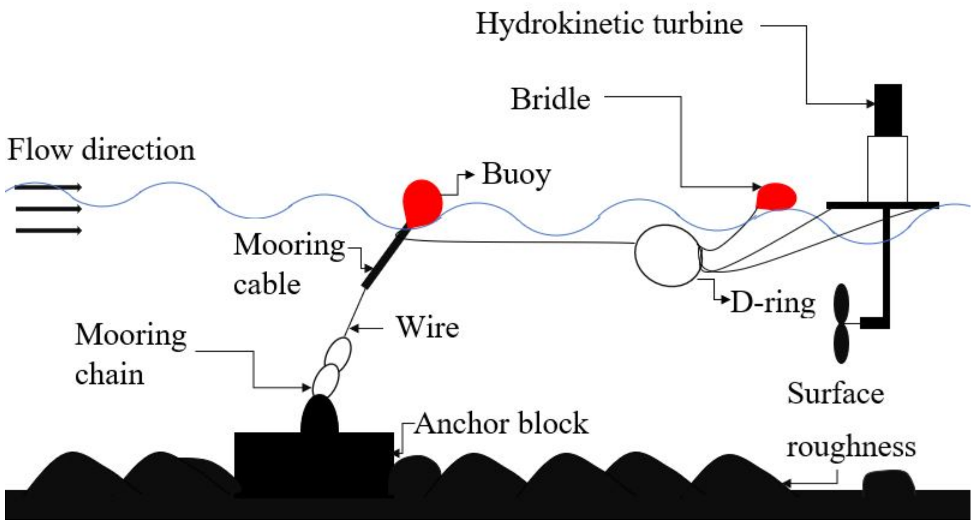

Figure 1.5: Schematic view of the anchoring and mooring system at the CHTTC. This study investigates the flow structures caused by this system on the performance of a turbine.

These turbine mooring anchors impact the flow while causing macro-turbulent structures. This impact by the turbine mooring anchors results in turbulent inflows into a HKT deployed downstream which can in-turn impact the power production from the turbine depending on the separation distance between the turbine mooring anchors and the turbine.

There is no literature on the experimental study to determine the impacts of turbine mooring anchors on the performance of a horizontal HKT deployed downstream of such anchors. Characterizing the flow upstream and downstream of turbine mooring anchors would be beneficial in designing and optimizing power production for the marine industry.

1.2.2 Surface roughness

Surface roughness, or simply roughness, can be described as the surface texture quantified based on its deviation from its ideal form. In a situation where the

Figure 1.6: Buoy replacement activity at the CHTTC. The orange buoys are replaced with the white buoys at the end of the winter season. The figure also shows the CHTTC crew detaching the mooring lines from the orange buoys on-board the measurement platform.

deviation on the surface is large, the surface is regarded as a rough surface, but when the deviations are small, the surface is regarded as smooth surface. River or channel bed structures such as bed ridges, slopes, boulders, hills and large rocks not optimally located in the velocity boundary layer of rivers and channels induce local velocity changes which impacts the performance of HKTs deployed in such areas. These structures exhibits stability and resistance against flow. At high flow velocities, such loose structures can be transported in river and channel beds. This makes proper understanding of the impacts of such structures a necessity when planning a HKT project. There are various studies on the impact of bed roughness on flow velocities and are reviewed in Chapter 2. However, with power extraction using HKTs attracting significant interests from researchers and developers, studies on environmental impacts on HKTs continues to grow to enhance HKT performance.

1.3 Objectives

Considering the potential impacts of mooring anchors and surface roughness as highlighted when planning a turbine project, the objectives of this research are listed below.

1. Determine performance improvement design of turbine mooring anchors that can be used when planning a turbine project.
2. Evaluate experimentally the impact of macro-turbulent structures caused by turbine mooring anchors and rough river beds on the performance of a HKT.
3. Test a scaled HKT in a steady inflow and determine the performance characteristics for various surface roughness and Reynolds number.

1.4 Methodology

The methodology used in achieving the research objectives is shown in Figure 1.7 and consists of laboratory tests at the University of Manitoba and field tests conducted at the CHTTC.

1.4.1 Laboratory testing

The laboratory test quantifies the performance of a scaled HKT in a uniform and non-uniform inflow in a water tunnel. To create the non-uniform inflow in the water tunnel, 25 surface roughness, and four different anchor geometries were located upstream of the turbine and tested to quantify their impacts on turbine performance. These anchor geometries were tested at different free-surface clearance height and separation distance from a scaled turbine. Testing these geometries within a controlled environment allows quantifying the impact of these geometries on HKT performance. The optimum performance test is carried out for uniform and non-uniform inflow with the anchor geometries and surface roughness simulating the non-uniform inflow into the turbine. The HKT operates based on two main operating conditions in these tests: large surface roughness and Reynolds number. The Reynolds number is a function of rotor diameter and free stream velocity. The turbine is tested at flow velocity of 1.1 m/s resulting to an unobstructed Reynolds number of 2.17×10^5.

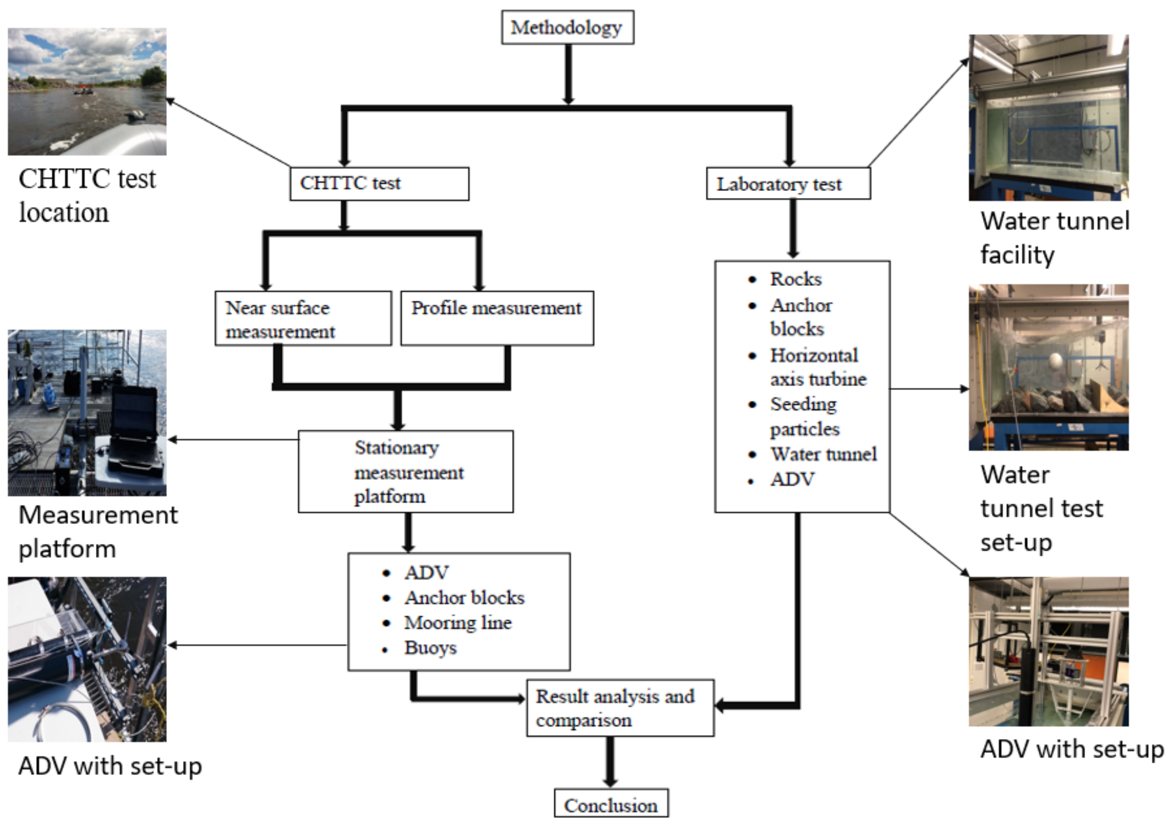

Figure 1.7: Schematic description of the methodology used in this research showing the CHTTC and laboratory test facilities as well as the ADV used to measure velocity and turbulence statistics

1.4.2 Field testing

Flow velocity measurements were taken at a length to diameter ratio of 15 and 16 upstream and downstream, respectively of in-service mooring anchors at the CHTTC as described in Appendix A. The field test identifies the macro-turbulent structures upstream and downstream of turbine mooring structures. Measurements were taken using an ADV which measures mean and fluctuating flow velocities up to 64 Hz sampling rate. ADV data are associated with spikes because of entrainment of air bubbles during testing. Due to this, the mean and fluctuating velocity data obtained from these points are filtered using a post-processing code, as discussed in Chapter 3. The code was developed for filtering these spikes in the ADV data set and compensating motion during measurement. These filtered data are further analysed and the difference in variation quantified to obtain the order of magnitude of the macro-turbulent structures upstream and downstream of the turbine mooring anchors.

1.5 Research contributions

Experimental data is obtained on the impact of turbine mooring anchors and rough riverbed in a highly energetic flow. The results obtained provides a better understanding of how turbine mooring anchors impacts flow pattern, mean velocity and turbulence intensity. The result obtained can help in improving designs of turbine mooring anchors when planning a turbine project. Deployment procedures for the ADV during field tests have also been improved because the observations made in this study.

A conference poster on hydrokinetic energy and macro-turbulent structures assessment in a high energetic river site has been published using the data obtained from the field test at the Offshore Energy Research Association (OERA) 2017 annual conference. The poster was awarded the OERA 2017 best research poster at this conference.

1.6 Outline

Chapter 2 covers literature review, which includes literature review on macro-turbulent structures, turbine mooring anchors and surface roughness. Boil generation and dissipation literature is also reviewed in Chapter 2. Chapter 3 details the laboratory and field testing facilities, instrumentation and other devices used during the laboratory and field test, as well as the test matrix and procedures. In Chapter 4, laboratory and field measurement results are presented. Research conclusion and recommendations based on observations as well as the extended research topics for future work are presented in Chapter 5.

Chapter 2

Literature Review

Turbine performance is an important factor to consider when designing, deploying, and operating a HKT. Turbine performance is evaluated based on the power output from the turbine and is affected by a number of factors. Research on the performance of HKTs has identified a number of factors that affects the performance of HKTs. Some of these factors include but are not limited to:

1. Macro-turbulent structures [17, 22]
2. Anchoring and mooring [4, 23]
3. River bed formation and structure [24]
4. Inlet flow velocity and conditions [12, 17]

In this chapter, literature relating to macro-turbulent structures, turbine mooring anchors, and surface roughness is presented while literature pertaining to fluid mechanics is reviewed in Appendix B.

2.1 Macro-turbulent structures

Research in fluid mechanics has primarily been devoted to micro-turbulence while macro-turbulent structures has received less attention especially for highly energetic river sites. Macro-turbulence in this research is used to denote large scale turbulent structures whose size is of the order of the characteristic dimension of the flow and larger than the turbine chord.

Mathes [25] classified macro-turbulent structures into six categories, namely:

- rhythmic and cyclic surge,
- rotary and continuous,
- upward vortex, intermittent,
- downward vortex, sustained,
- transverse oscillation, and
- helicoidal and continuous.

These macro-turbulent structures includes, but not limited to, eddies, boils, wakes etc. A rotating fluid motion that possesses continuity with the prevalence of the flow pattern creating it is denoted as an eddy [25]. Depending on the topography of the channel, deposition of materials in suspension can be caused by eddies. Eddies occurs at bays due to excessive channel width and presence of upstream obstructions such as bridge piers, buoys, boats, instruments, turbine mooring anchors and cables that causes velocity deficit while the flow reattaches some distance behind the cause of obstruction. Eddies play an important role in turbulent flows with their sizes in order of magnitude of the flow location. They can be categorized into large and small scale eddies depending on magnitude. However, large scale eddies can cascade into smaller eddies if they are unstable. The turbulence Reynolds number for a given eddy size is given by

$$R_l = \frac{\upsilon_\lambda * \lambda}{\nu}, \tag{2.1}$$

where λ, is its magnitude, and υ_λ, is its velocity order of magnitude.

The larger the turbulence Reynolds number, the larger the magnitude of the eddy. Large Reynolds numbers are associated with low viscosity because of no appreciable energy dissipation in large eddies unlike small scale eddies whose turbulence Reynolds number is comparable to unity, have energy dissipation. The above energy dissipation conception shows that dimensional arguments determines the order of magnitude of energy dissipation. It is found that energy dissipation is proportional to the third power of the largest eddies velocity, and inversely proportional to its size.

Power production from a HKT is impacted by velocity deficit, non-uniform inflow, and macro-turbulent structures. Birjandi [17] while investigating the impact of flow structures on turbine performance demonstrated that macro-turbulent structures caused by an upstream cylinder could enhance the power production from the turbine. They further stated that measurements upstream of the turbine showed a reduction in the mean velocity and the disintegrations of the large eddies into smaller sizes, which resulted in an increase in the turbulence intensity of the flow into the turbine. While the performance of horizontal HKTs about its axis of rotation is symmetrical, they are subjected to non-uniform inflow velocity and large-scale turbulent eddies while in operation. In an experiment on turbine fatigue, Sutherland and Kelly [26] demonstrated that large-scale eddies contained in turbulent inflows impose cyclic loads on the blades of a horizontal wind turbine, thereby inducing fatigue but that did not have much effect on the turbine's performance. Studies are currently ongoing in identifying the effects of non-uniform inflow including the study by the National

Renewable Energy Laboratory [26, 27].

Yokosi [24] in a study on river turbulence demonstrated that the order of magnitude of large scale eddies is determined by the river depth and width, upstream structures and unpredictable river bed changes. This, in a HKT farm site, amongst other constraints, makes the adequate spacing of HKTs of critical importance to avoid undue interactions. These interactions lead to reduced performance of HKTs located downstream due to their location within the wake of an upstream turbine or structure. Power losses from a turbine can be up to 23% due to wake effects depending on the distance between them and the pattern of arrangement in a wind farm [28, 29]. In such a condition, the turbine behind the upstream turbine or structure is the most affected by the upstream wake while others turbines are less affected [29].

Reviewing aerodynamics of wind turbine wakes, Sanderse [30] stated that the life span of a wind turbine rotor blade is shortened because of fatigue loads, which are increased up to 80% in the wake region. Similarly, Adaramola et al. [22] in an experiment on wake effects on a horizontal wind turbine found that the wakes generated because of the upstream turbine affected the power extracted from the downstream turbine. Furthermore, they stated that separation distance was one of the factors that contributed to the loss of power which was between 20% to 46% for the downstream turbine relative to the unobstructed upstream turbine. However, when these turbines were operated in a yawed condition-a condition were the turbine is rotated at an angle, the total power produced from both turbines increased by 12% as a result of less obstruction caused by the upstream turbine. They concluded that the separation distance between turbines in a turbine farm or behind upstream structures should be enough to have the downstream turbines away from the wake region.

Modelling terrain effects on a single and two inline turbine Meada et al. [31] stated

Table 2.1: Summary of literature review on operating factors that affects the performance of a HKT

Author	Study type	Region	Results
Mathes [25]	Experimental	Stream	Macroturbulence occurs in a natural stream. They are continuous, cyclic and rhythmic and are not related to microturbulence. They are caused as a result of channel roughness and flow separation.
Birjandi [17]	Experimental	River	Macroturbulent structures affect the performance of a HKT. Mean velocity reduction leads to eddies breaking down into smaller sizes.
Kelly and Sutherland [26]	Experimental	Wind	Large-scale eddies contained in a turbulent flow causes fatigue loads on wind turbine blades
Yokosi [24]	Experimental	River	Depth and width of a channel contribute to the generation of meter sized eddies in flowing water bodies.
Hand et al [27]	Experimental	Wind	Unsteady flow affects the performance of horizontal axis wind turbines.
Barthelmie [28]	Experimental	Wind	Wakes affect horizontal wind turbine performance. Due to wakes, performance dropped by 20%. Separation distance should be enough to reduce wake effect.
Beyer [29]	Experimental	Wind	Wakes affected the power production from the wind turbines. Power reduction traits compared to Lissaman and Riso prediction model
Sanderse [30]	Experimental	Wind	Wake affects the life span of rotor turbine blades due to increase in fatigue load
Adaramola et al [22]	Experimental	Wind	Wakes affect the turbine performance. Lack of proper separation distance caused power loss between 20 to 46%
Maeda et al [31]	Experimental	Wind	Wakes affected horizontal axis wind turbine in an array.Turbulence intensity and inflow velocity also contributed to power reduction.
Eduardo et al [32]	Numerical	N/A	Optimization of hydrokinetic turbines. Separation distance affects the capacity factor of turbines both in inline operation and staggered positions.
Troldborg et al [33]	Numerical	N/A	Wake remains unstable one rotor diameter downstream of HKTs operating in turbulent inflow. Separation distance affects power generation.
Michelsen [34]	Numerical	N/A	Developed a multi-block solver
Sorensen [35]	Numerical and experimental	N/A	Developed 2D and 3D finite volume code based on RANS equation. Flow simulation over hill shows good agreement with measurement.
Mann [36]	Numerical	N/A	Large eddy simulated
Sorensen et al [37]	Numerical	N/A	Developed actuator line model for large eddy simulation.

that power output from a wind turbine is not determinant on the actual wind profile but rather an increase in turbulence intensity on the velocity profile leads to a power drop from the first turbine. They also stated these wakes recover faster due to increased diffusion, thereby leading to an increase in power from the second turbine. They concluded that separation distance is a very import factor for turbines in a turbine farm. Eduardo et al. [32] also identified separation distance amongst other parameters as an important function in approximating the capacity factor of arrays of turbines.

There have been numerous studies on the shapes and properties of wakes caused by kinetic turbines, such as the one by Barthelmie et al. [38]. They carried out a study at the horizontal wind turbine farm at Middelgriden offshore on the effect of power losses because of wakes generated by upstream turbines. They stated that the wind farm had an overall performance efficiency of less than 10% compared to an individual turbine due to wakes while turbines in the second row, separated from the first row by 2.4 diameters, had 20% efficiency. They concluded that even though the efficiency increases from the third row of turbines, the wind velocity in the wake region was 80% of the free-stream velocity and was constant throughout the array of turbines.

Further studies on wake effects on kinetic turbines include such study by Troldborg et al [33] where they compared the wake of turbines operating in a uniform inflow with that of the simulated wake and found that for a turbine operating in a turbulent inflow, the wake is observed to be unstable one rotor diameter downstream of the operating components of the turbine, compared to a turbine operating in a uniform inflow whose wake remains stable almost five rotor diameter downstream of the operating turbine. They achieved this by coupling the large eddy simulation solver developed by Michelsen [34] and Sorensen [35] with the method of an actuator line developed by Sorensen and Shen [37] and finally adding the turbulence to the simulation by

Mann algorithm [36]. They concluded that, compared to the wake generated from turbines operating in a uniform inflow, the wakes from a turbine operating a non-uniform inflow have a smaller tail and hence tends to recover faster. Thus, in terms of spacing, this means that the spacing between turbines in a turbulent inflow is much smaller compared to that in a uniform inflow. These studies are of interest as we focus on macro-turbulence generated by mooring anchors in which there are relative few studies. However, many studies like the study on macro-turbulent flow interaction with vertical HKT by Birjandi et al. [17] have show that HKT is affected by macro-turbulent structures.

2.2 Turbine mooring anchors

Power production using a HKT is a function of the third power of the flow velocity, V^3, as shown in Equation 1.1. This shows the importance of turbine mooring anchors when planning a turbine project. With most of the kinetic energy in a river or channel flow stored in the upper half of the flow [12], the boundary layer region, which is the region with flow velocity lower than the freestream velocity, is associated with powerloss when a HKT is deployed there [4]. To improve the power generation capacities of turbines deployed in boundary layers of flows Gaden [4] proposed altering the geometries of the anchor blocks deployed upstream of the turbine. An anchor block is a component deployed at the river beds or shores used in mooring HKTs or floating structures and keeping them at desired locations. Though there are other methods of securing HKTs to riverbeds as proposed by Segergren [39] including the use of mooring lines or cables which enables the deployment and retrieval of HKTs to and from the desired locations.

The cross-section or river width, affects the design specifications of a HKT in terms of deployment that in turn affects the performance of the turbine. This has led to specific technological questions such as the benefits of duct augmentation, best converter types, turbine mooring anchor design, deployment method and environmental monitoring, [40] being raised when turbine design and deployment is discussed. While mooring lines help to align a HKT with the incoming flow [23], anchor blocks keep the device at the deployment location while withstanding forces from the environment. With research and development of HKTs on the rise, their turbine mooring anchors should also be given upmost attention if optimum performance is to be guaranteed from the HKTs. Clarke [41] acknowledges that if the full benefits of a HKT is to be obtained, cost effective, single riser, tensional turbine mooring anchors should be employed. With majority of the kinetic energy located in the upper part of the water column [12], turbine-mooring anchors that will allow HKTs to operate in this region [41] is suggested.

Furthermore, researchers and developers have long identified river or channel depth as an important parameter in turbine mooring anchor design. This is because it is believed that river or channel depth will impact the mooring cable length, configuration and geometry. Many approaches have been used in designing and analysing turbine mooring anchors that can withstand environmental impacts of rivers and channels flow while keeping the floating structures connected to them at the desired location. Depending on the depth of river or channel, couple of analysis have been carried to determine the impacts of mooring cable tension on floating structures and flow patterns. Ormberg et al. [42] showed that water depth and distance of moored floating structure from mooring point are important parameters in analysing mooring structures.

To demonstrate the importance and impact of turbine mooring anchors in turbine development and deployment, VanZwieten et al. [43] in a study on anchor selection, stated that HKTs need turbine mooring anchors to keep them in energy dense locations, while surviving environmental effects. They also stated that with the development of HKTs on the rise, single or multi turbine mooring anchors should be designed to keep up with this developmental rise. In locations were positive buoyancy can not be used to produce lift for the turbines, they suggested a design which utilises lifting surfaces for variable depth operation which can be seen in VanZwieten [44]. Similarly, to also demonstrate the importance and impacts of turbine mooring anchors in HKT development, Frankel [45] found that bi-directional mooring system is crucial in ocean applications having tried and failed with several turbine mooring anchor designs and methods. A 130 metric-ton unit was cemented to the bed of the English Channel off Devor coast, South-West England. Due to the anchoring method employed in this location, the rotor was designed in a such a way that it can be rotated to accept flow in both directions. With this deployment type, 100 and 300 kW average and peak power respectively was produced from the turbine.

2.3 Riverbed surface roughness

Bed of rivers and channels are known to have boulders, large and small gravel rocks, sediment grains, debris of various kinds that results to surface roughness of the river and channel bed. Surface roughness of rivers and channels impact boundary layer transitions and hydrodynamic predictions in the boundary layer due to complex interaction between the bed surface materials and the approaching turbulent flow especially in highly energetic rivers and channels. The interaction between these bed surface materials and approaching turbulent flow impacts the near-bed turbulent flow field [46] and ultimately sediment transport timing and magnitude [47] which in turn impact any HKT deployed in that area. Papanicolaou et al. [48] while investigating the mean and turbulent flow fields near a submerged boulder within an array of boulders, through systematic comparison of time-averaged streamwise velocity profiles acquired around the boulder using an acoustic Doppler velocimeter, showed that recorded flow around the boulder affected flow modification and pattern around the boulder arrays. Similarly, Tsakiris [49] in a study on influence of boulders on time averaged and turbulent flow fields showed that individual boulders impacted the time averaged and turbulence intensity within their immediate vicinity both in streamwise and vertical directions. They concluded that outside of the boulders immediate vicinity, their impacts on the time-averaged streamwise velocity decelerated due to drag generated by the boulder array.

Furthermore, it has been shown that shear flow generated in near-bed of gravel bed river and channels generate macro-turbulent flow structures. Though, laboratory and field experiments have shown that such flows contain flow structures that are coherent and steady, their turbulent characteristics, origin and evolution have remained misunderstood. However, interaction with heterogeneous sedimentary gravel bed is one of the key features that determine river flow characteristics pattern. These interactions leads to the creation of shear instabilities in the boundary layer of rivers and channels playing a vital role in the formation of macro-turbulent flow structures [50]. These shear instabilities were investigated by Hardy et al. [51] in a study on coherent flow structures in a depth-limited flow over a gravel surface. They found that they are generated by flow separation because of flow over multi-scale bed topography in the boundary layer as well as the wake of each of the bed formation.

Turbulence in rivers and channels is not a simple random field; measurement and flow visualization have shown that it can decompose into elementary spatial and temporal structures from multi-scaled, quasi-random and complex flow fields [52].

Rivers and channels with gravel beds are associated with shallow flows with $10 - 20$ mean depth to roughness height ratio in high flow conditions and less than 5 in low flow conditions [53]. In flows with such high roughness heights, field and laboratory experiments as well as numerical predictions have shown that bed structures significantly impact the generation and dissipation of macro-turbulent structures [51, 54]. Flow visualization and quantitative measurements have been combined in several studies in other to understand the generation and dissipation of macro-turbulent structures over rough and smooth surfaces [51, 55, 56]. The size and morphology of these macro-turbulent structures has been found to be proportional to a list factors which includes but not limited to:

1. bed roughness [56]
2. river or channel depth [57]
3. Reynolds number [51]

Klaven et al. [58] while investigating flow turbulent structure over smooth and unstable gravel beds using a visualization technique showed the existence of large macro-turbulent structures with their vertical sizes close to the depth of the river, h. They stated that the length of the macro-turbulent structures exceed the water depth and varied from 4h to 7h for the smooth and rough beds, respectively. These macro-turbulent structures have been hypothesized from a structural standpoint, to be similar to a bursting phenomenon [59]. Kline et al. [60] detected that away from the wall using hydrogen bubble visualization, repetitive ejections of fluid with high-speed in rushes of fluid towards the wall sweeping away the low-speed fluid remaining from ejections. Since then, several studies on bursting processes in open-channel flows have been carried out near rough and smooth beds [61, 62]. However, it has been found that these fluid ejections are not limited to the bed region. Talmon et al. [63] in a study on flow visualization and measurement in turbulent boundary layer, stated that not only that they are not restricted to the bed region, they impact the entire flow field irrespective of the bed roughness with the low-momentum fluid travelling the entire flow depth to the water surface and the high momentum fluid moving down to the bed [61].

Despite studies on turbulent flow in gravel beds, knowledge on the impact of River rocks flows is lacking. Though agreement on the bursting phenomenon pattern in gravel beds have been reached [62], there still various opinions pertaining to depth scale motions in open-channel flows. This, Yalin [64] in a study on river mechanics, argued that macro-turbulent structures are not permanent as well as do not emanate in their full sizes. He stated that though macro-turbulent structures generate from near the beds, they grow in their sizes until they get to their biggest sizes and thereafter, cascade into smaller structures. Though, consistent with laboratory and field experiments, complete life cycle of macro-turbulent structures generated in river or channels occurs over a distance of $6h$, quasi-stable large scale macro-turbulent structure existences is still disputable. However, in laboratory and field experiments, evidence of velocity fluctuations that corresponds to the spatial scale of the flow depth exists [65] while some do not state a regular period in velocity fluctuations [66]. This, Nikora et al. [67] postulated that macro-turbulent structures generated in river and channel beds in time and space are distributed randomly up to the water surface. Studies have shown that coherent macro-turbulent structures contribute to the growth of pressure fluctuations and turbulent shear stress in rivers and channels [63] which impacts bed particles and control motion of sediments. This, therefore, creates a need for more studies on macro-turbulent structures and their impacts on flow patterns especially in regards to impacts of large river rocks on HKT.

2.4 Flow effects on HKTs

Flow properties affects the power production from a HKT. However, these impacts are dependent on a number of factors such as the flow velocity, channel bathymetry and HKT type amongst others. Using a PIV and a dye injection technique to test flow effects around a vertical axis wind turbine, Fujisawa et al [68] observed the formation of two pairs of counter-rotating vortices in the wake generated by the turbine blades. They stated that flow separation due to high angle of attack as the flow moves across the leading edge, was the cause of the vortex formation. As seen in the Von Karman street, the rolling-up of the second vortex pair, helps in reattaching the separated flow while both pairs of the vortex have similarities with the vortices.

Birjandi and Bibeau [69] demonstrated that the Reynolds number, inlet flow conditions and frequency of vortex shedding affect the power production from a vertical HKT. They also demonstrated in their study that the Reynolds number impacts the power coefficient at low Reynolds number; at high Reynolds number, the power coefficient is less sensitive to the Reynolds number. In addition, the power production from the HKT was affected by the frequency of the vortex shedding and that while power was seen to have increased at frequency occurring between two prime frequencies - the principal frequency integer factor frequencies, power production from the HKT decreased at prime frequencies.

2.5 Boil investigations

Bathymetry, rocks, bed structures and shapes are features associated with rivers and channels. Meter sized coherent structures, often referred as boils, responsible for sediment, momentum, nutrient and temperature redistribution and transportation, are a function of these river and channel features. Understanding the characteristics of boil kinematics in rivers, channels and estuarine is an important factor modelling river flow [25]. In a laboratory experiment by Muller and Gyr [70], boil generation is described as the interaction of span-wise vorticity caused by flow separation due to bed topography or flow instability.

These boils deform into a hairpin spanwise vorticity loop and due to downstream bends in the water body, erupt and self-advect at the water body surface [62]. Advection is a type of transportation by a substance by means of bulk motion where the properties of that substance are carried along with it.

Flow separation is observed behind obstructions and hills in fluid studies. In a comprehensive field study and laboratory model of flows over dunes, flow separation was observed at the crest of the dunes while at the wake of the mixed-layer, Kelvin-Helmoltz instabilities were generated [71]. Kelvin-Helmoltz instability is a type of hydrodynamic instability observed when inviscid fluids are in an irrational motion. Boil-like structures are seen to be generated at the point of flow reattachment at the downstream bend of the channel during these experiments that Best [54] suggested is because of the interaction between the water surface and a hair pin like vortex.

Boil observation in laboratory settings and their numerical models are not substantiated or validated due to lack of detailed boil in-situ measurement. Boils observed at the water surface begins with an up-welling or self-advection from the bed. Chickadel et al [74] carried out a study in a submerged estuarine sill on vertical boil propagation. They created a two-dimensional model for vertical boil propagation using boil disruption location and surface diameters. Velocity over the sill, depth of sill and vertical velocity were used in obtaining a prediction of boil disruption location during the study. Their prediction from the vertical velocity model agreed with the measured distance from the point of generation to the point of eruption of the boils. They concluded that, boils observed through measurement agree with a boil-surfacing

Table 2.2: Summary of literature review on flow effects on HKTs and boil investigation

Author	Study type	Region	Results
Fujisawa [68]	Experimental	River	Two pairs of counter-rotating vortices were observed in the wake of a blade. Flow separation occurred due to the high angle of attack.
Birjandi et al [69]	Experimental	Laboratory	Reynolds number increases with power coefficient at low Reynolds number. Macroturbulent structures affects power production from VAT
Muller and Gyr [70]	Experimental	River	Boil generation is a function of span-wise vorticity interaction caused by flow separation due to bed topography
Nezu [62]	Experimental	River	Boils deforms into hairpin spanwise vorticity loop. Boils erupt and self-advect at the water body surface.
Venditti [71]	Experimental	River and laboratory	Flow separation observed at the crest of dunes and Kelvin-Helmholtz instabilities observed in the wake of mixing-layers.
Best [54]	Experimental	River	Boils generate at the point of flow reattachment downstream. They are consistent with a the result of the interaction between the water surface and a hairpin-like the vortex
Coleman [72]	Experimental	River	Unsteady nature of rivers leads to kinematics of boils in river bodies.
Kostaschuk [73]	Experimental	River	Dunes were observed to generate macro-turbulence. Obtained data didn't support boil generation from micro-turbulence but from macro-turbulence.
Chickadel et al [74]	Experimental	Numerical and river	Boils caused by rocky sills results in surface disruptions as observed using a thermal infrared camera. Vertical propagation model agrees to surface disruptions by boils.

model from wakes of a turbulent mixing layer observed in a laboratory setting. Boils have been physically observed in the CHTTC during experiments. However, its point of generation and causes are part of this experiment and flow measurements.

2.6 Non-uniform inflow

Power production by a HKT is affected by non-uniform flow through the turbine. Kelley et al [26] demonstrated that the blades of horizontal wind turbines are subjected to heavy loads and fatigue as a result of the unsteady and turbulent meter scaled eddies they are subjected to. In a similar study, Sutherland et al. [75] found that the blade joint of a 34 m diameter vertical axis wind turbine is affected during operation due to the unsteady wind, gravity and gyroscopic loadings it was exposed to. In a study on the structure of river turbulence at the Uji river and the Sosui canal using a propeller type current meter, Yokosi [24] proved that the river width and depth contribute to the generation of meter-sized eddies in the river, hence the need to design, manufacture and deploy turbines in comparison to the river width and depth. Apart from river depth and width, unpredictable river bed changes, anchor blocks, mooring lines, floating buoys and upstream turbines are some other factors that contribute to unsteady flows and meter-sized eddy generation. The presence of these meter-sized eddies, affects the flow velocity required for the blades to function as expected. This condition most times, when steady flow is not restored, leads to dynamic stalling of the blades which, which usually occurs when the blade stall angle is exceeded [76].

Bathymetry is also important when selecting a site for a HKT deployment and testing. Bathymetric features such as rocks with magnitude in the order of the rotor diameter can cause unpredicted velocity profile changes in the boundary layer. In a study, Evan et al. [77] observed that the local bathymetry and magnitude of the velocity in the flow direction were the two main factors that influenced the wake recovery behind the submerged pinnacle. Using large eddy simulation and an actuator disc as an array of HKTs, Soto and Escauriaza [78] found that bathymetric features caused velocity boundary layer changes upstream the disc, which affected the arrays performance. Researchers have been lead to the analysis of simple bathymetric features due to the high cost of computation in analysing both temporal and spatial real bathymetric features. Performance of HKTs can be improved if an optimal location point of operation is chosen given the local bathymetry of the strait [79].

To achieve optimum performance, HKTs are deployed in locations with optimum flow velocity. Doing this requires well-designed turbine mooring anchors capable of withstanding various weather conditions while keeping the HKT in the desired location. Research on the impact created by the turbine mooring anchors on HKTs deployed downstream of such structures could not be found by the author, hence the importance of this research as it is expected that mooring will make the flow less uniform.

Chapter 3

Instrumentation, water tunnel tests, and field testing at the CHTTC

To quantify the impact of macro-turbulent structures caused by mooring anchors and rough riverbeds on the performance of a HKT, laboratory and field tests were carried out as shown in Figure 1.7. A scaled horizontal HKT designed and manufactured by Mohammed [12] is used for the laboratory testing. Details of the mooring anchors designed and fabricated as well as the experimental facilities, instrumentation and set-up are described in this chapter. The instrumentation used for measurements, laboratory testing facility, turbine mooring anchors, test matrix and procedure used for laboratory testing are first described, followed by the field testing facility, measurement locations, points of interest and test procedure. The laboratory tests were conducted at the University of Manitoba's water tunnel facility. The ADV used to measure flow velocity is first presented.

3.1 ADV

Flow velocities are measured using an ADV. The ADV is a Nortek Vector AS which can measure flow velocities in the laboratory and field settings and is shown in Figure 3.1. High temporal and spatial resolution is required in carrying out fluid measurements in these settings. The ability of the ADV to perform in applications associated with flow impurities, or where the user has no control over the flow, makes the ADV the technique of choice in these settings compared to other Doppler instruments. Other factors considered in choosing the ADV over other Doppler instruments includes its small sampling volume, relatively low cost and ability to record at very high frequencies. The sampling volume of the Nortek Vector is 15.7 cm away from the probes while the sampling height can be adjusted from $5-20$ m based on users' preference.

To improve the quality of the velocity data obtained, the size of the sample volume is increased, but this leads to increase in the signal-to-noise ratio (SNR). Based on

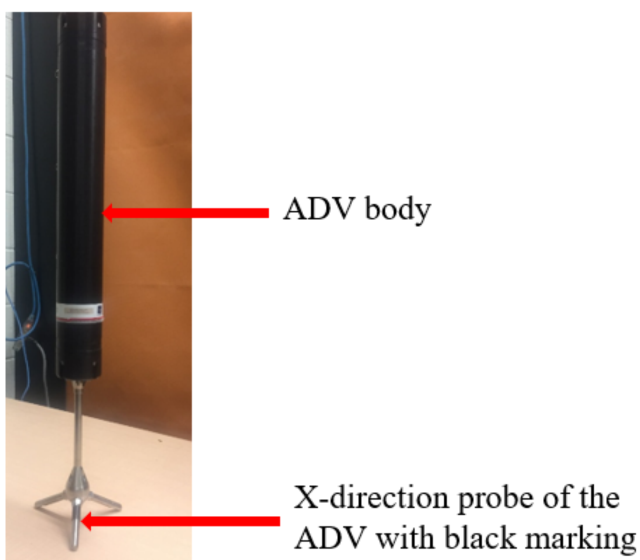

Figure 3.1: Nortek Vector AS ADV used during the laboratory and field tests. The ADV measures flow velocities in three dimensions measuring U, V, W, and from these $\overline{u^2}$, $\overline{v^2}$, $\overline{w^2}$, $\overline{uv}$, $\overline{uw}$ and $\overline{vw}$ are evaluated.

manufacturers recommendation, velocity data with an SNR above 10 is valid but to guarantee quality turbulence measurement, an SNR above 19 should be obtained [17]. Even with its low sampling volume, the ADV is able to capture the Turbulent Kinetic Energy (TKE) when deployed [80]. Using the principle of Doppler shift, the ADV measures flow velocities in three dimensions and consists of three-receivers, a signal conditioning module and a pulse transmitter. Other specifications of the vector ADV are as shown in Table 3.1

During operation, the ADV through its transmitter generates acoustic signals, which are reflected back by sound scattering particles in the water, and moves at the same speed as the water velocity. Flow velocities in radial or beam directions are calculated from the Doppler phase shift computed because of the scattered sound signal obtained by the three ADV sound receivers. The vector ADV used in this study is a bi-static sonar and measures velocity components parallel to its three beams. Data obtained from the ADV is reported in XYZ coordinate system. Irrespective of the how the ADV is deployed, the XYZ coordinates remains the same for they are reflective to the three probes, as seen in Figure 3.1. From the figure, the positive X-direction probe is the probe with a black marking, which is aligned with the flows stream-wise direction, the positive Z-direction is towards the instrument itself while the positive Y-direction is across the spanwise direction. The ADV probe is used for both laboratory and field tests.

Table 3.1: Nortek Vector AS ADV specifications

Velocity range	0.01, 0.1, 0.3, 1, 2, 4, 7 [m/s] (software selectable)
Sampling rate	1 - 64 Hz
Internal sampling rate	100 - 250 Hz
Uncertainty	1 % of velocity range
Acoustic frequency	6 MHz
Accuracy	+ or - 0.05 % of measured value
Pressure range	0 - 20 m (standard)

3.2 Water tunnel

Figure 3.2a shows the vertical configuration, recirculation design-type water tunnel facility at the University of Manitoba with internal test section dimensions of 183 $\times$ 61 $\times$ 62 cm used for laboratory tests. The water tunnel facility allows a maximum water height of 60 cm in the test section and is driven by a single stage, axial flow propeller pump which delivers 362 l/s flow rate during operation. Surrounded with Plexiglas by the sides, bottom and back of the test section, flow video recording and observation is made possible when in operation. A Toshiba induction motor of 30 HP, 60 Hz, 3 phase, 460 VAC and $1,800$ rpm drives the pump belt with the flow speed adjusted using an inverter type variable speed controller. The inverter as shown in Figure 3.2a, is graded from 0 to 60 Hz, providing water velocities up to 1.1 m/s in test section of the tunnel.

A relation between the inverter frequency and the test section flow speed at water height of 60 cm is shown in Figure 3.2b. The large eddies and vortices generated by the water tunnel facility pump are broken down by series of honeycombs located

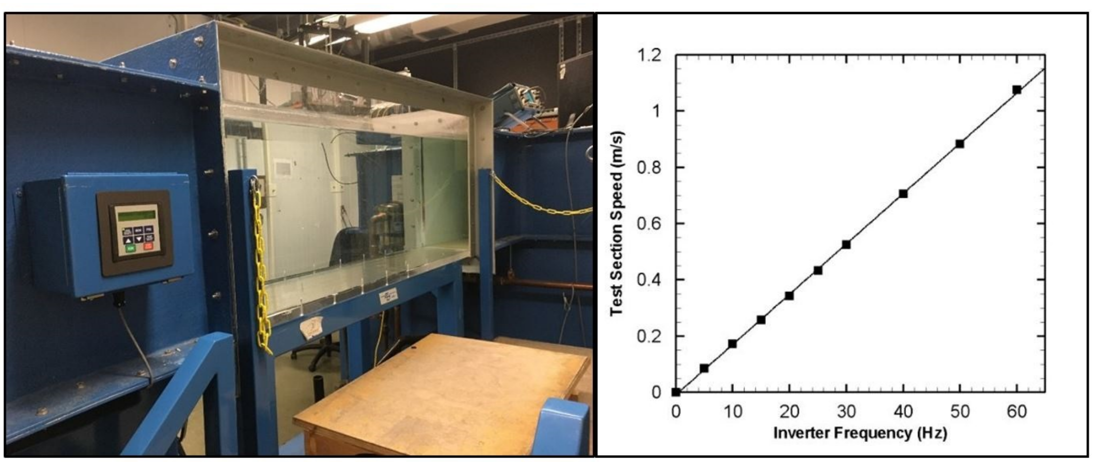

(a) (b)

Figure 3.2: Laboratory test facility: (a) water tunnel with inverter, and (b) relationship between water tunnel inverter frequency and test section flow speed at maximum water height

before the test section and for flow velocities of 1.1 m/s, these honeycombs help to keep the turbulence intensity in the test section between 1% to 3%. Different water heights are achieved in the test section using a drain.

3.2.1 Seeding particles

To enhance the SNR in a water tunnel experiment with water devoid of impurities and particles, suspended particles are introduced. In this research, 50 μm diameter DANTEC Polyamide seeding particles was used which has a density close to that of water to enable them to remain suspended in water flow and for 3 to 4 hrs in the absence of flow. About 40 counts per second is the number of particles required by the ADV to achieve the noise threshold. For a more accurate ADV measurement 80 counts and above is suggested [81]. The seeding particles are as shown in Figure 3.3.

Figure 3.3: Seeding particles used during the laboratory tests to improve the SNR

3.3 Scaled mooring anchor geometries

Four different scaled turbine mooring anchor geometries were designed and made out of 3/8 ” marine plywood. The plywoods were glued together with titebond wood glue and coated with total boat penetrating epoxy to prevent them from absorbing water and getting soggy. They were tested to study their impact on the turbine performance through manipulation of their wake structure and increased flow velocities.

Figure 3.4 show anchors A and B, adapted from Gaden [4], which were designed with the aim of maximizing its flow obstruction characteristics in the boundary layer and based on a wind turbine contraction cone function, respectively. Furthermore, anchor C was designed to reduce the re-circulation observed in anchor A, while anchor D was designed to quantify the impact of a dead-weight anchor observed at the CHTTC.

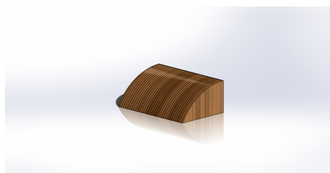

(a) Anchor A

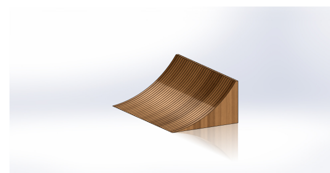

(b) Anchor B

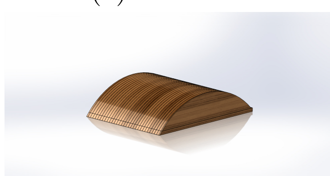

(c) Anchor C

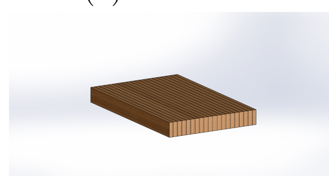

(d) Anchor D

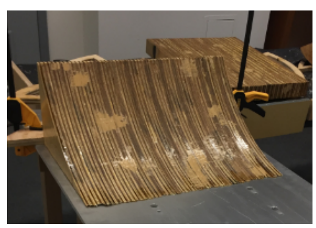

(e) Anchor E

Figure 3.4: Figures (a) to (d) shows anchor geometries tested in the water tunnel to determine their impact on the performance of HKT while (e) shows the anchor fastened to the stainless flat plate before been deployed into the water tunnel

From a deployment standpoint, the anchors are fastened to a $160 \times 60 \times 3$ cm aluminium flat metal plate as shown in Figure 3.4e before been deployed into the water tunnel to ensure the remain in the desired position when operating at high flow velocities. The dimensions of the scaled mooring anchor geometries are shown in Table 3.2.

Table 3.2: Dimensions of the scaled mooring anchor geometries

Anchors	Height (cm)	Length (cm)	Width (cm)
A	20	35	54
B	20	35	53
C	16	69	53
D	6	44	55

3.4 Scale model turbine

Figure 3.5 shows the scaled horizontal HKT designed by Mohammed [12] used in this study. The turbine has a flat base plate which enables it to sit on the water tunnel facility upper rim while having its rotor hub located at the center of the flow cross section. The location of this rotor hub at the center of the flow cross section, guarantees a 1 rotor diameter clearance between the turbine, the test section walls and the free surface. The rotor blade of the turbine is attached to the horizontal shaft which is coupled to a vertical shaft with a right angle 1 : 11 bevel gear box.

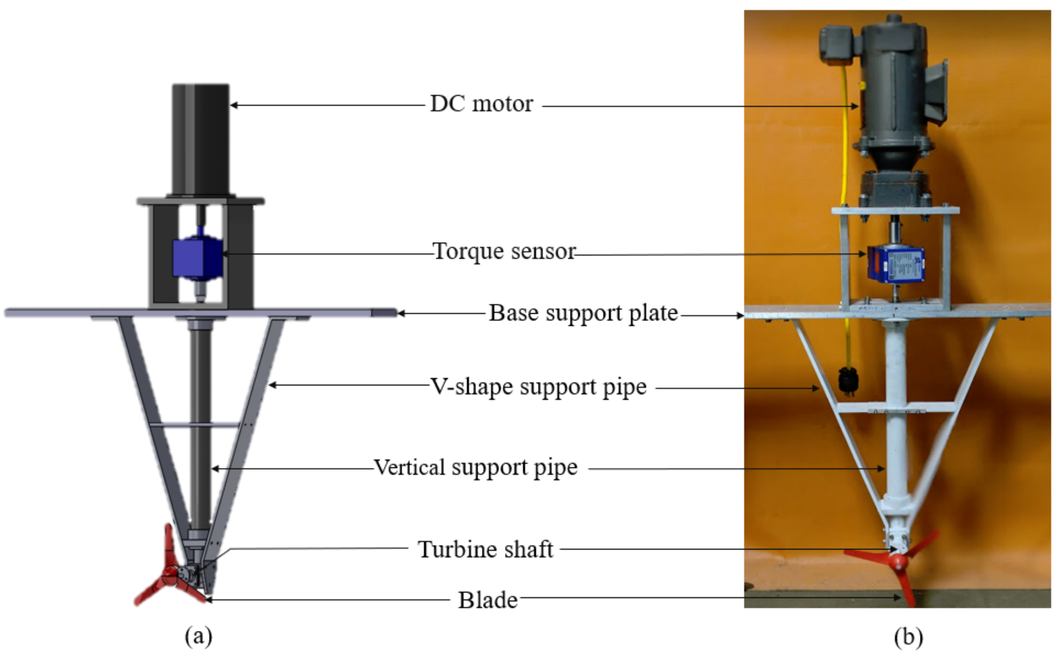

Figure 3.5: Scaled HKT model used for research in the water tunnel facility: (a) schematics, and (b) built system

The connection of the horizontal shaft to the instrumentation at the top of the flat base plate is made possible by a vertical shaft and ball bearings inside a vertical support pipe. One radius of the vertical support pipe, the horizontal shaft align the rotor blade upstream perpendicularly to the flow direction while the V-shaped flat plate secures the horizontal and vertical support shaft to the flat base plate. These arrangements eliminates and minimizes the effects of flow fluctuations, vibrations of the turbine and shaft speeds at high velocities, on the performance of the turbine.

3.4.1 Blades

A three bladed $H0127$ KidWind Project Inc. rotor blade of 19.8 cm diameter is used in this research as shown in Figure 3.6. These blades have flat bottom airfoils and 19% of the rotor blade diameter as their hub diameter as observed from the physical geometric observation and measurement of the rotor blade using a calliper of 0.02 mm accuracy.

Figure 3.6: KidWind rotor blade with diameter 19.8 cm

They also have a solidity of total blade area to swept area of blade of 0.13 while a circular curve of r/R = 0.96 at 0.7 mm radius, makes at the blade tip, a rounded end. These blades can be purchased commercially if needed for further experiment and usage.

3.4.2 Torque transducers

As shown in Figure 3.5, a Torqsense Rayleigh waiver rotary torque transducer is placed between the vertical turbine shaft and the motor. This torque transducer with a maximum speed of 500 rpm and a maximum torque range of 1 Nm measures between the turbine and motor the torque for the power curve entire range. The torque transducer has a 100 Hz and + or - 0.25% response frequency and accuracy, respectively. Power extraction from scaled HKTs in water tunnel experiments is achieved using the driving motor method [82] for the performance curve range instead of the generator and variable resistance method often used in this type of experiments [83], which is faced with the limitation of power capturing at low speeds as a result of blade stalling. The torque transducer is shown in Figure 3.7.

In the driving method, a 0.25 HP AC motor coupled with a 1:2 speed reducer that reduces the motor rpm while providing the required torque, drives the turbine at constant speed during the experiment. The motor rpm and the rotational speed values of the turbine is achieved with an AC motor speed controller system. The torque transducer has both analog and digital system output and guarantees direct turbine power measurements due to its user adjustable rotational speed sensor range. The torque transducer is connected electrically and to prevent any damage to its driving installation process, it is connected and operational during installation. The torque transducer has a connection cable with which is connected to a computer. To prevent axial load, its body, using flexible strap, transducer shaft ends, and connection couplings is prevented from rotating.

During operation, a negative torque reading shows that the turbine spins the motor faster thereby generating power while a positive torque reading shows that the motor is spinning the turbine due to blade stalling thereby generating less power.

Figure 3.7: Torque transducer placed between the turbine vertical shaft and motor to measure the torque on the turbine shaft

3.5 Test matrix

Having identified and described the devices and instruments needed to achieve the research objectives, a test matrix for laboratory tests was developed and shown in Table 3.3 while Table 3.4 shows the summary of the surface roughness parameters used in this study. From Table 3.4 we conclude that the average Hr_{ave}/H_w is 0.20.

Test 1 was used both as a base experiment to determine the optimum performance parameters such as R.P.M, Cp, overall clearance coefficient of the turbine in an unobstructed flow velocity. In Test 2, 3, and 4, turbine mooring anchors, surface roughness and turbine mooring anchors with surface roughness were introduced and their impacts tested on the performance of the turbine.

In all test conditions, flow frequency on the water tunnel inverter was kept constant and flow velocity measurements obtained using the ADV from the measurement points listed on the test matrix. Due to lack of impurities in the water tunnel, seeding particles as described in Section 3.2.1 were added in all test conditions to improve the SNR and sampling rate of the ADV. All rocks used in simulating surface roughness in this study were placed on the $160 \times 60 \times 3$ cm aluminium flat metal plate and arranged in an ascending order based on their average height.

Table 3.3: Test matrix for water tunnel experiment showing locations where measurements were taken, and parameters measured at those locations. Xd are the measurement locations in the streamwise direction, Yd are measurement locations in the spanwise direction, and Zd are the measurement locations in the vertical direction.

Experiment	**Experimental hardwares**	**Tunnel height (H_t)**	**Velocity**	**Xd**	**Yd**	**Zd**	**Parameters measured**
Test 1	Turbine only	60 cm	1 m/s	1D	0	$0.25H_t$	Power and clearance coefficient
				2D	0.5D		
				3D	-0.5D	$0.50H_t$	
Test 2	Turbine and mooring anchors	60 cm	1 m/s	1D	0	$0.25H_t$	Power, velocity and turbulence
				2D	0.5D	$0.50H_t$	
				3D	-0.5D		
Test 3	Turbine and surface roughness	60 cm	1 m/s	1D	0	$0.25H_t$	Power, velocity and turbulence
				2D	0.5D		
				3D	-0.5D	$0.50H_T$	
Test 4	Turbine, mooring anchors and surface roughness	60 cm	1 m/s	1D	0	$0.25H_t$	Power, velocity and turbulence
				2D	0.5D		
				3D	-0.5D	$0.50H_t$	

3.6 Clearance coefficient

Experimental testing of scaled HKTs have blockage effects amongst other factors to contend with. In classifying free-blockage effects, clearance coefficient, a non-dimensional parameter is used, and it is defined as

$$C = \frac{H_w}{L}, \tag{3.1}$$

where H_w is water height, L is rotor diameter for horizontal HKT, and H is the blade height for a vertical HKT.

A positive or negative clearance coefficient is obtained when the water height is above or below the turbine blade tip, respectively.

Table 3.4: Summary of the surface roughness used in simulating rough surface in the water tunnel showing rock parameters. Three random samples were taken to obtain the height and projected area of each rock.

Rocks	**Weight, W (N)**	**Volume, V (cm^3)**	**Rock height, H_r (cm)**			Hr_{ave}	Hr_{ave}/H_w	**Projected area, PA (cm^2)**			PA_{ave} **(cm^2)**
			1	**2**	**3**			**1**	**2**	**3**	
1	33.76	1276.03	13.50	15.10	14.20	14.27	0.24	159.20	154.70	257.20	190.37
2	28.70	1084.62	10.50	12.20	11.50	11.40	0.19	216.30	90.44	116.56	141.10
3	16.88	638.01	10.50	12.10	8.30	10.30	0.17	127.20	90.00	75.65	97.62
4	50.65	1914.04	15.30	11.50	10.50	12.43	0.21	132.50	217.92	237.65	196.02
5	50.65	1914.04	14.70	10.50	14.20	13.13	0.22	305.00	233.00	111.36	216.45
6	33.76	1276.03	14.60	9.50	16.50	13.53	0.23	111.50	121.20	116.00	116.23
7	25.32	1276.03	8.50	18.50	21.50	16.17	0.27	118.75	386.72	61.40	188.96
8	25.32	957.02	10.30	10.50	10.80	10.53	0.18	164.60	145.20	184.74	164.85
9	37.14	1403.63	15.10	7.50	8.50	10.37	0.17	71.34	228.00	85.00	128.11
10	16.88	638.01	15.10	6.50	18.10	13.23	0.22	79.76	71.50	240.25	130.50
11	42.20	1595.04	13.90	10.20	12.50	12.20	0.20	93.88	202.35	117.05	137.76
12	33.76	1276.03	13.50	9.50	13.50	12.17	0.20	102.20	152.00	104.75	119.65
13	33.76	1276.03	13.40	10.50	11.30	11.73	0.20	135.92	152.72	126.65	138.43
14	23.63	893.22	14.30	11.50	10.50	12.10	0.20	94.00	165.50	159.50	139.67
15	25.32	957.02	14.50	7.50	14.50	12.17	0.20	77.80	195.80	85.40	119.67
16	33.76	1276.03	17.70	7.50	17.50	14.23	0.24	93.50	57.30	149.72	100.17
17	33.76	1276.03	11.20	10.50	14.10	11.93	0.20	108.11	103.68	98.00	103.26
18	8.44	319.01	14.50	5.90	20.50	13.63	0.23	60.56	274.56	20.25	118.46
19	33.76	1276.03	13.20	7.50	12.20	10.97	0.18	141.20	160.34	260.48	187.34
20	25.32	957.02	12.50	6.50	14.50	11.17	0.19	77.50	156.05	62.70	98.75
21	8.44	319.01	5.50	7.50	11.50	8.17	0.14	114.45	90.10	17.38	73.98
22	16.88	638.02	12.10	9.50	11.50	11.03	0.18	118.25	82.65	179.55	126.82
23	33.76	1276.03	13.50	10.20	13.50	12.40	0.21	114.60	180.40	96.08	130.36
24	25.32	957.02	15.50	5.50	7.50	9.50	0.16	61.60	263.88	152.05	159.18
25	25.32	957.02	14.20	15.50	20.50	16.73	0.28	228.14	404.74	91.25	241.38
Total	**722**	**27,626**									**3,565**

3.7 Laboratory test procedures

The laboratory test set-up as shown in Figure 3.8 consists of the ADV, water tunnel facility, model turbine, mooring anchors and surface roughness.

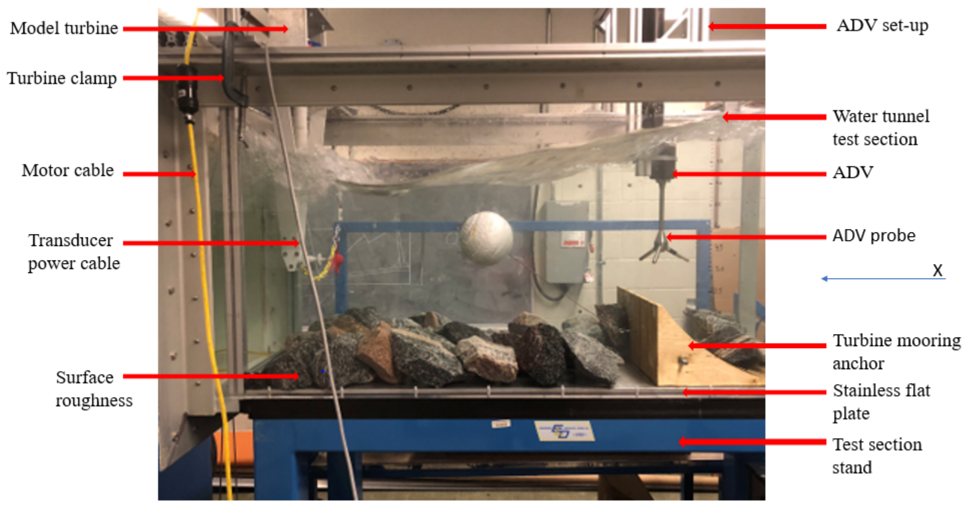

Figure 3.8: Laboratory test set-up showing ADV mounted on the set-up designed for water tunnel experiments, the model turbine clamped downstream of the water tunnel, turbine mooring anchor and surface roughness distributed on the bed of the water tunnel

The model turbine is first deployed downstream the water tunnel, tested in an unobstructed flow velocity of 1 m/s and the Cp and other parameters obtained. Thereafter, free-surface effect was tested by changing the water height and the clearance coefficient obtained. Having obtained the maximum Cp of the turbine in an unobstructed flow velocity and the ideal clearance coefficient, each of the turbine mooring anchor geometries were then fastened to a $160 \times 60 \times 3$ cm stainless flat plate which covers the entire bed surface of the water tunnel before been deployed to ensure the turbine mooring anchors remain in the desired location and avoid scratching of the bed surface. Thereafter, the four different turbine mooring anchor geometries were then deployed 2 and 3 diameters upstream of the turbine to determine the impact of the macro-turbulent structures they cause in the performance of the turbine. The

ADV set-up designed for tests in water tunnel as shown in Figure 3.9. This set-up was used to transverse through all the measurement points during the test.

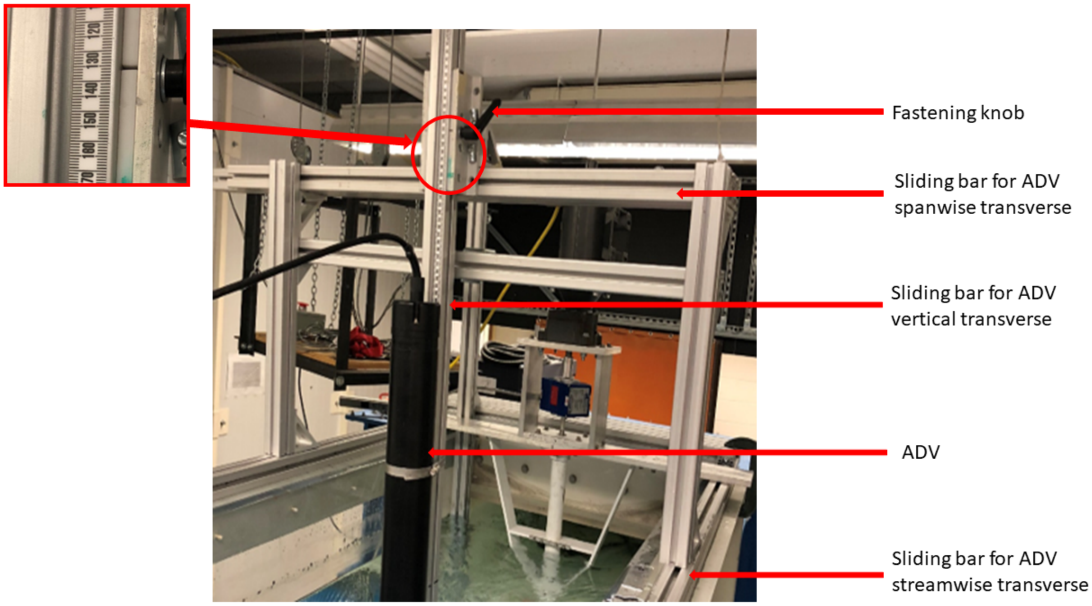

Figure 3.9: ADV laboratory set-up showing the ADV mounted and the sliding bars which enables the traversing of the ADV through the measurement points in the test section of the water tunnel

During these tests, flow velocity measurements were taken using an ADV as described in Section 3.1 at three streamwise locations along the tunnel; 1 diameter upstream, 1 and 2 diameters downstream of the mooring anchors. At these locations, measurements were obtained at 0.25 and 0.50 tunnel height, H_t along the vertical direction.

Furthermore, in Test 3, surface roughness was placed on the stainless flat plate and arranged in ascending order in the water tunnel as shown in Figure 3.10 to determine the impact of the macro-turbulent structures they cause on the performance of the turbine. Flow velocity measurements were also obtained using an ADV at the locations described above and Cp obtained from the turbine as well.

Finally, the turbine mooring anchors and the surface roughness were tested with

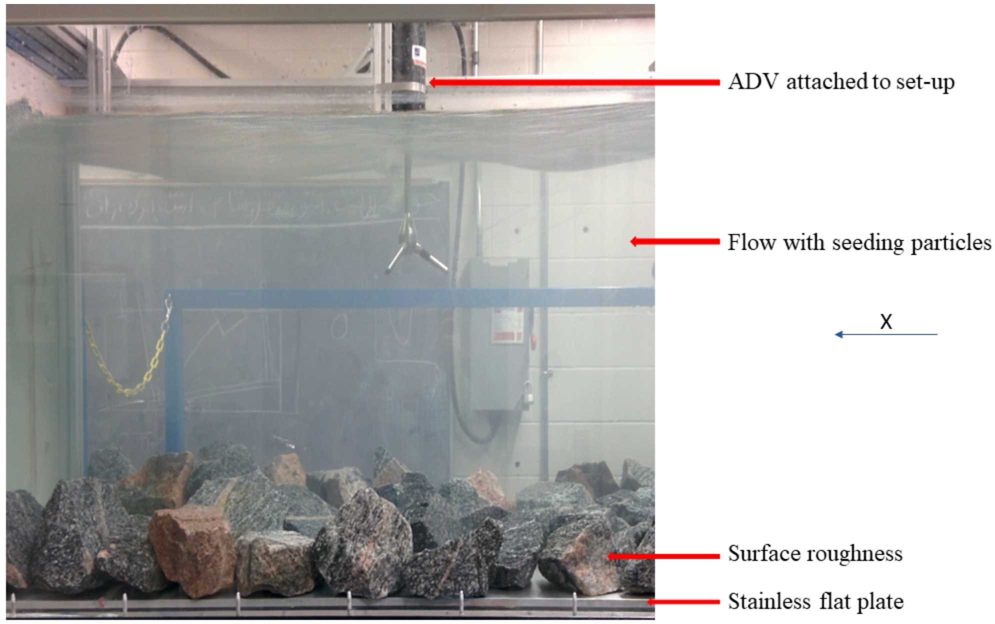

Figure 3.10: Surface roughness distribution on the bed of the water tunnel showing the stainless flat plate used in preventing the scratching of the plexiglass bed during test. Rocks were repositioned eight times to make results statistically representative.

the turbine in the Test 4 and measurements obtained in the locations described above. The surface roughness was rearranged for each test involving each of the mooring anchors resulting to surface roughness been rearranged eight times in this test. However, all experiments were carried out at maximum water height of 60 cm with flow measurements taken at locations and points described earlier.

3.8 Field test

Flow velocity measurements were carried out to quantify the macro-turbulent structures caused by turbine mooring anchors at the CHTTC. In carrying out these measurements, the procedures developed by D'Auteuil [3] for velocity and turbulence measurement in high energetic flows were employed. In this procedure, a measurement platform as shown in Figure 3.11 is equipped with velocity and turbulence measuring instruments such as ADV, horizontal acoustic Doppler current profiler, vertical acoustic Doppler current profiler and a laptop for real-time data observation as well as safety devices such life jackets, ring buoys etc. The data obtained using the ADV as described in Section 3.1 are filtered, compensated of motion during measurements and analysed to achieve research objectives.

3.8.1 Measurement locations

These refers to all the locations where data were obtained during the field tests as shown in Figure 3.12. These locations were selected based on the anticipated velocity at the locations but in such a way that the velocity and turbulence behavioural changes at the channel will be well captured. However, locations 15 and 16 length to diameter ratio upstream and downstream of the turbine mooring anchors at the CHTTC are considered in this research and are marked as CP-F and CP-G in

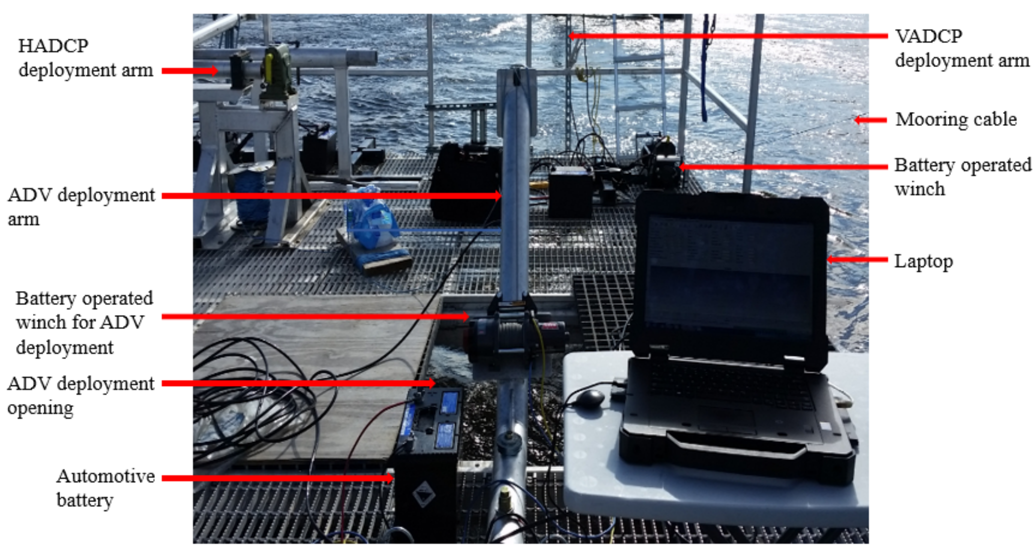

Figure 3.11: Fixed measurement platform with measuring instruments and safety devices during experiment at the CHTTC. The fixed measurement platform is anchored on both sides of the channel using a mooring cable and an automotive battery-operated winch.

Figure 3.12.

3.8.2 Points of interest

Points of interest are the points within the locations described in Section 3.8.1 ADV measurements were obtained. These points, marked as F1, F2, F3 and G1, G2 within locations CP-F and CP-G, respectively in Figure 3.12 were selected to ensure the flow velocities are well captured upstream and downstream the turbine mooring anchors, mooring cables and buoys in order to quantify their impacts on a HKT deployed downstream.

3.9 Field test procedures

The first step in the field test procedure is equipping the fixed measurement platform with the measuring instruments and safety devices listed in Section 3.8. Thereafter,

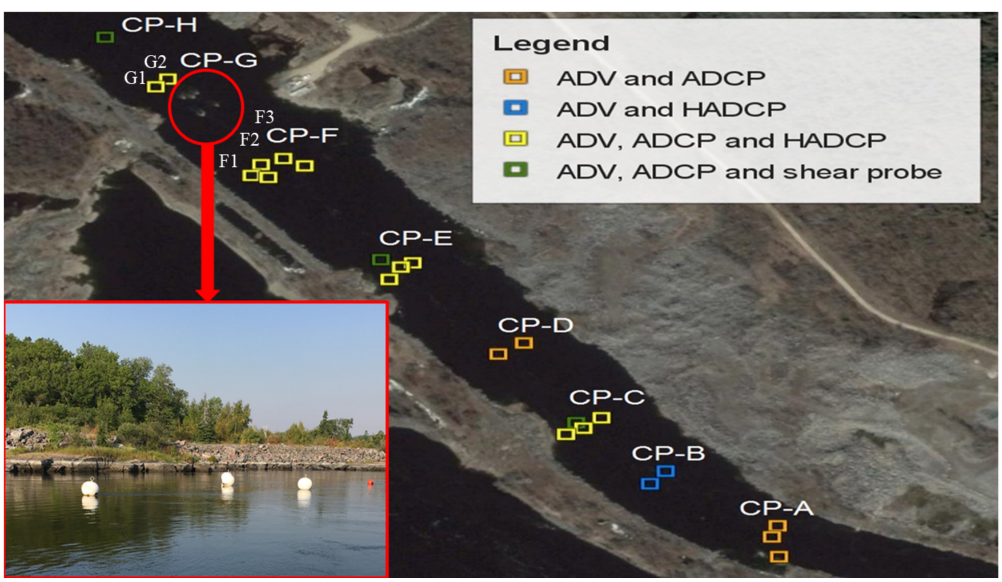

Figure 3.12: Goggle earth view of all measurement locations at the CHTTC. Locations CP-F and CP-G are the locations of interest while points F1, F2, F3, G1 and G2 were the exact points where measurements were taken during the test.

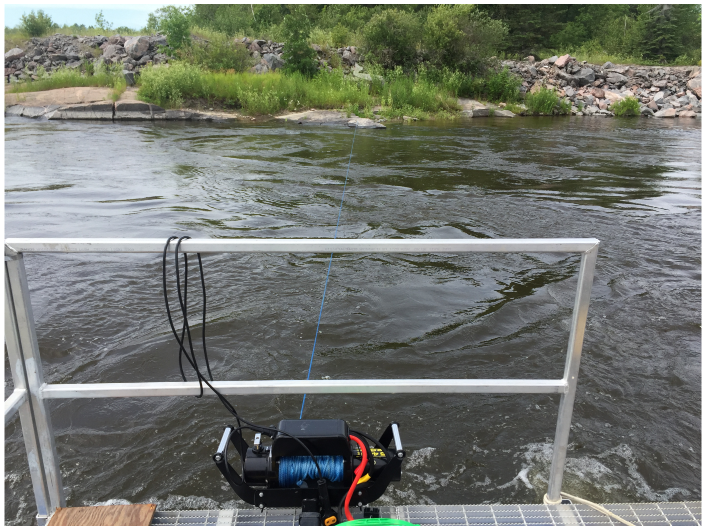

Figure 3.13: Fixed measurement platform anchored during measurement using an automotive battery operated winch and mooring cable

the boat operator, drives the fixed platform to the identified location. On getting to the location, the fixed measurement platform is anchored on both sides of the channel with a mooring cable and automotive battery-operated winches. Anchored fixed platform is as shown in Figure 3.13.

Next, the ADV and other instruments are then attached to their deployment set-up and deployed. To deploy the ADV through the ADV deployment opening as shown in Figure 3.11 on the measurement platform, three 25 kg blocks are connected to a steel cable and with the aid of an automotive battery-operated winch are deployed into the channel. These blocks help in straightening and aligning the steel cable perpendicular to the flow direction allowing the whole ADV set-up to travel through it to get to the desired channel depths while having the x-direction probe of the ADV aligning perpendicular to the flow direction with the help of the fin as seen in Figure 3.14. The ADV is then attached to the ADV deployment set-up as shown in Figure 3.14 and then deployed along the steel cable.

With the pressure sensor on the ADV, the depth at which the ADV is at is known once it is connected a laptop. To obtain the data at different channel depths in the highly energetic flow, the mooring cable attached to the ADV set-up as shown Figure 3.14 is used in deploying the ADV to the desired channel depths and in retrieving it at the end of the measurement. The ADV power and computer cables are then connected to a power source and a laptop, respectively. The anchor block at the CHTTC is shown in Figure 3.15 while the dimensions of mooring anchors at the CHTTC and the distance of measurement locations to mooring anchors are shown in Table 3.5.

Following the procedure and the test matrix as shown in Table 3.6, the ADV is deployed and used in obtaining flow velocity and turbulence data from the highly energetic flow upstream and downstream the turbine mooring anchors at the CHTTC. The data obtained were processed using the post processing code discussed in Section 3.8, analysed and the result of their impacts stated and discussed in Chapter 4.

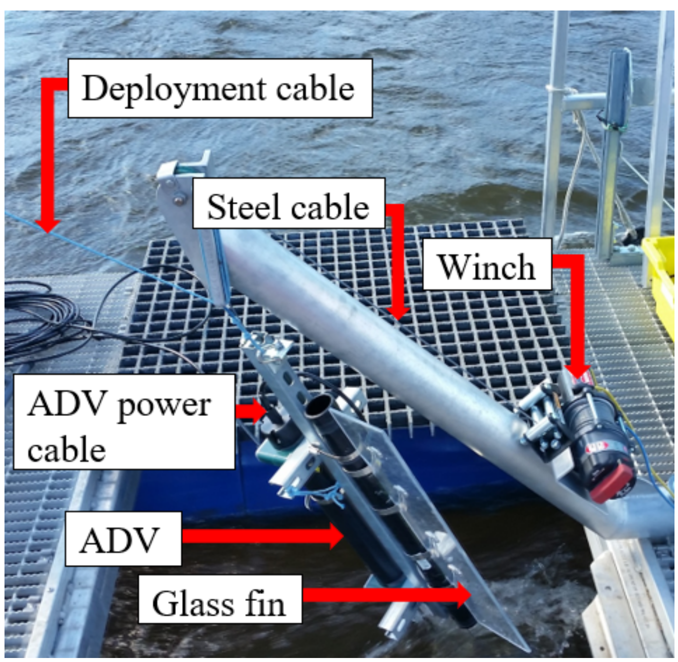

Figure 3.14: Field test ADV set-up with ADV attached to it ready to be deployed through the fixed measurement platform

Figure 3.15: CHTTC anchor block with mooring line attachment points

Table 3.5: Dimensions of mooring anchors at the CHTTC and the distance of measurement locations to mooring anchors

Anchor blocks	**Height (m)**	**Length (m)**	**Width (m)**
Block 1	0.9	2.5	1.1
Block 2	0.8	2.1	1.5
Block 3	0.9	2.9	0.9
Length to diameter ratio between CP-F and mooring anchors			15
Length to diameter ratio between CP-G and mooring anchors			16

Table 3.6: Test matrix used for CHTTC experiment showing measurement locations and points of interest where measurements were taken. Measurement locations and points of interest are as identified in Figure 3.12

Measurement location	**Points of interest**		**Parameters measured**
X-direction	**Y-direction**	**Z-direction**	
CP-A	0.25W	0.10H, 0.15H, 0.25H, 0.35H	Velocity and turbulence statistics
	0.50W	0.45H, 0.55H, 0.60H, 0.65H	
	0.75W		
CP-B	0.25W	0.10H, 0.15H, 0.25H, 0.35H	Velocity and turbulence statistics
	0.50W	0.45H, 0.55H, 0.60H, 0.65H	
	0.75W		
CP-C	0.25W	0.10H, 0.15H, 0.25H, 0.35H	Velocity and turbulence statistics
	0.50W	0.45H, 0.55H, 0.60H, 0.65H	
	0.75W		
CP-D	0.25W	0.10H, 0.15H, 0.25H, 0.35H	Velocity and turbulence statistics
	0.50W	0.45H, 0.55H, 0.60H, 0.65H	
	0.75W		
CP-E	0.25W	0.10H, 0.15H, 0.25H, 0.35H	Velocity and turbulence statistics
	0.50W	0.45H, 0.55H, 0.60H, 0.65H	
	0.75W		
CP-F	0.25W	0.10H, 0.15H, 0.25H, 0.35H	Velocity and turbulence statistics
	0.50W	0.45H, 0.55H, 0.60H, 0.65H	
	0.75W		
CP-G	0.25W	0.10H, 0.15H, 0.25H, 0.35H	Velocity and turbulence statistics
	0.50W	0.45H, 0.55H, 0.60H, 0.65H	
	0.75W		
W is the width of the channel and H is the height of the channel			

Chapter 4

Laboratory and field measurement results and discussions

4.1 Laboratory tests results and analysis

In this section, the results of the water tunnel experiments investigating the impact of mooring and surface roughness on turbine performance are presented. Comparisons are made with the results of other studies on turbine performance enhancements. Test matrix and procedures used in this study were detailed Sections 3.5 and 3.7, respectively.

4.2 HKT in an unobstructed flow

As stated in Section 3.5, the test with the turbine in an unobstructed flow without rocks and mooring anchors was conducted to serve as a control experiment for comparison and to determine the optimum performance parameters of the turbine for an unobstructed velocity. Figure 4.1 shows the performance curve obtained in an unobstructed flow velocity from the rotor in a break position with a TSR of 0, increasing to the maximum TSR of 3.9, and then decreasing to a TSR of 7.1 at a free-wheeling condition. Figure 4.1 also shows the peak TSR to be almost at the centre of the performance curve, a behaviour that has been observed and reported by other studies [12, 22].

For the unobstructed flow velocity of 1.1 m/s corresponding to a Reynolds number of 2.17×10^5 based on rotor diameter, the maximum C_P obtained is 0.43, which henceforth is referred to as the reference C_P. Furthermore, a clearance coefficient of 1.4 is set for the clearance coefficient to ensure a constant water height is maintained throughout the tests. Given the satisfactory nature of the values obtained, these

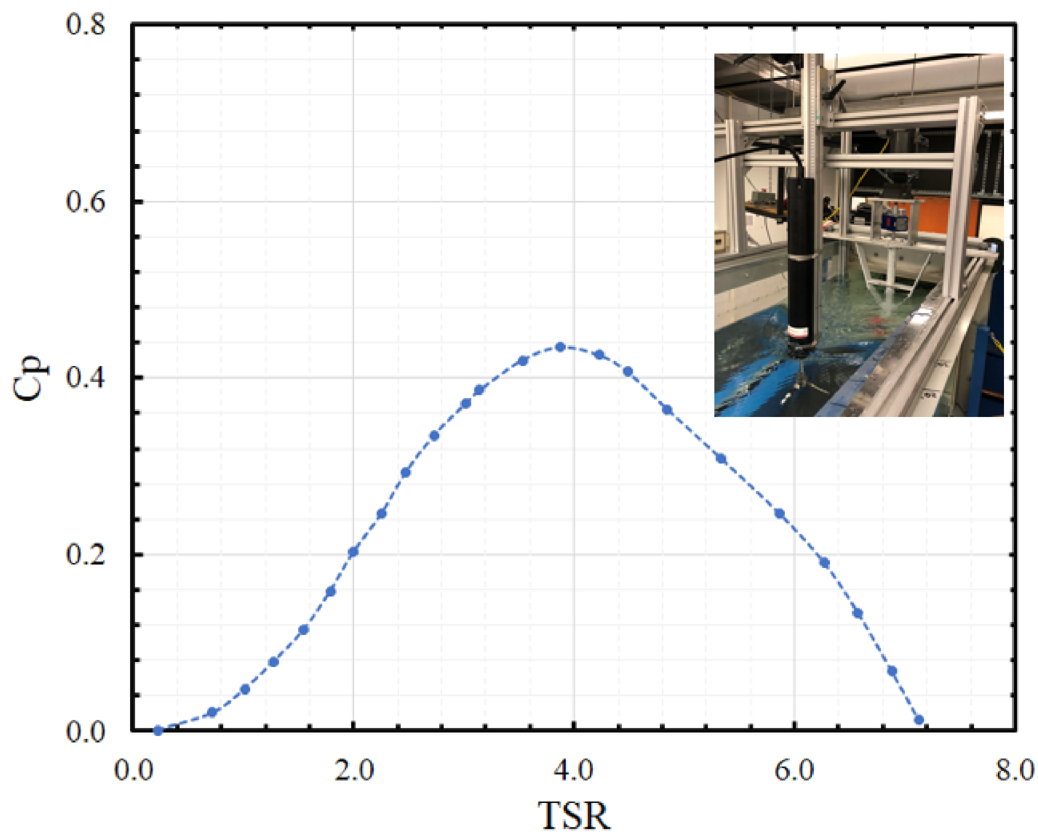

Figure 4.1: Performance curve obtained from the scaled HKT which shows the scaled turbine been tested in the water tunnel in an unobstructed flow velocity and the ADV attached to the frame

Table 4.1: Summary of parameters measured in the unobstructed flow test and the values obtained

Parameter	**Value**
Cp	0.43
U	1.1 m/s
V	0.01 m/s
W	0.02 m/s
TI	2.25%

conditions were used to evaluate the impacts of the mooring anchors and surface roughness on HKT performance. Measured values obtained for the unobstructed test are summarized in Table 4.1.

4.3 HKT mooring anchors

As stated in Section 3.7, impact of four different geometries of mooring anchors and their effect on turbine performance were tested. These turbine mooring anchors were deployed 2 and 3 diameters upstream of the turbine. Such proximately helps to place the turbine behind anchors to hide from debris during spring run-off.

4.3.1 Impact of turbine mooring anchors

With the turbine mooring anchors deployed 2 diameters upstream of the turbine, results show that the C_P obtained increased compared to the reference C_P, as shown in Figure 4.2. From the figure, it can be seen that the deployment of anchors A to D resulted to an increase in C_P of 0.58, 0.56, 0.50 and 0.45, respectively, from the 0.43 reference C_P. When compared to the reference C_P, this corresponds to 25%, 23%, 14% and 4% improvement in performance, respectively. Also, a closer look at Figure 4.2 shows performance curves starting from zero, peaking at a TSR between 3.7 and 4.3, and finally, descending to a TSR between 7.0 and 8.0.

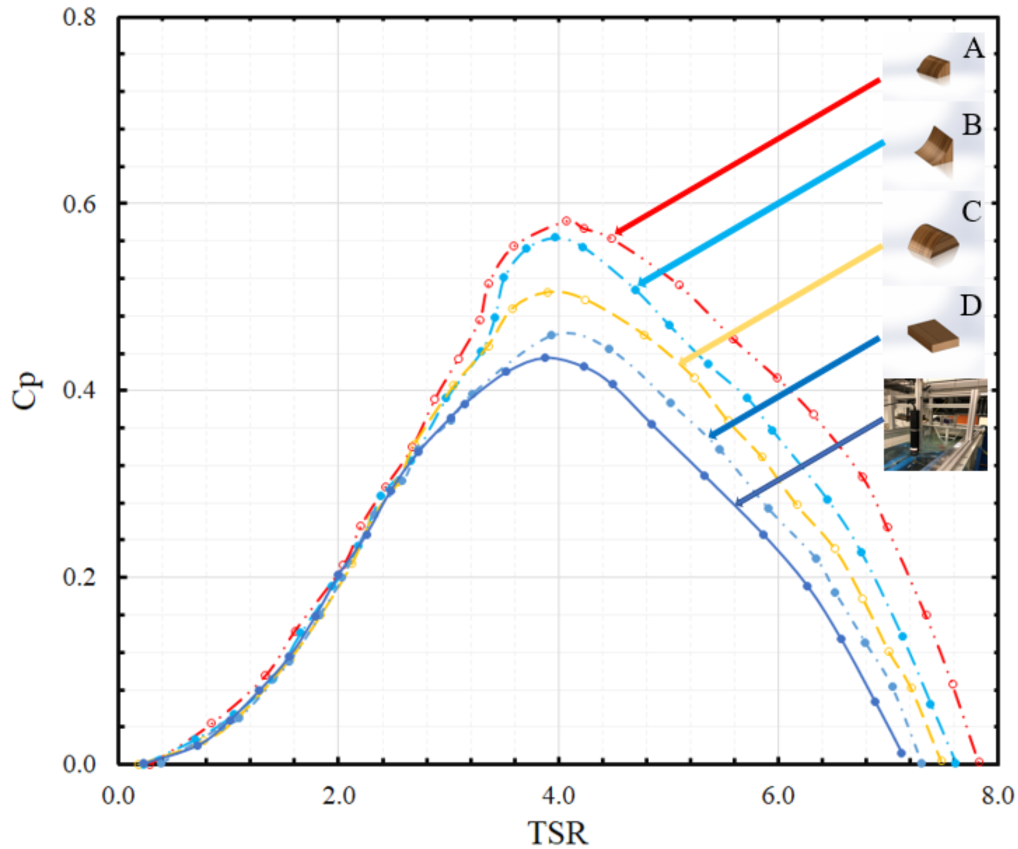

Figure 4.2: Performance curve obtained from the turbine with turbine mooring anchors deployed 2 diameters upstream of the turbine. Also showing are the turbine mooring anchor geometries: anchors A, B, C and D tested with the turbine.

Furthermore, from Figure 4.2, performance curves increase as the TSR increases until they get to their peak, and thereafter, descend with further increase in TSR. Krogstad [84] in a study on model turbine performance stated that, near the root of the blade at TSR equal to 4, the first stalling indication was observed while at TSR less than 3, the turbine blade was observed to be operating in a deep stall mode over the entire span. Stall development in the low TSR region leads to loss in lift, and consequently, power generation in this region. This explains the falling of the power curves on each other in this region as seen in Figure 4.2. However, at high TSR, the drag on the blade decreases as a result of the blade operating at the ideal and increased angle of attack which in turn leads to performance enhancement of the turbine.

The deployment of the mooring anchors at 2 diameters upstream of the turbine impacted the flow velocity and pattern in the water tunnel as shown in Figures 4.3 for anchors A to D. With the turbine mooring anchors deployed 2 diameters upstream of the turbine, average velocities of 1.41, 1.34, 1.25 and 1.23 m/s were obtained. Compared to the velocity obtained when the turbine was tested in an unobstructed flow as stated in Table 4.1, the deployment of the turbine mooring anchors resulted to a 21%, 17%, 12% and 10% increase in streamwise velocity corresponding to anchors A to D, respectively. This increase in streamwise velocity can be said to have contributed to the performance improvement observed from the turbine deployed downstream the mooring anchors.

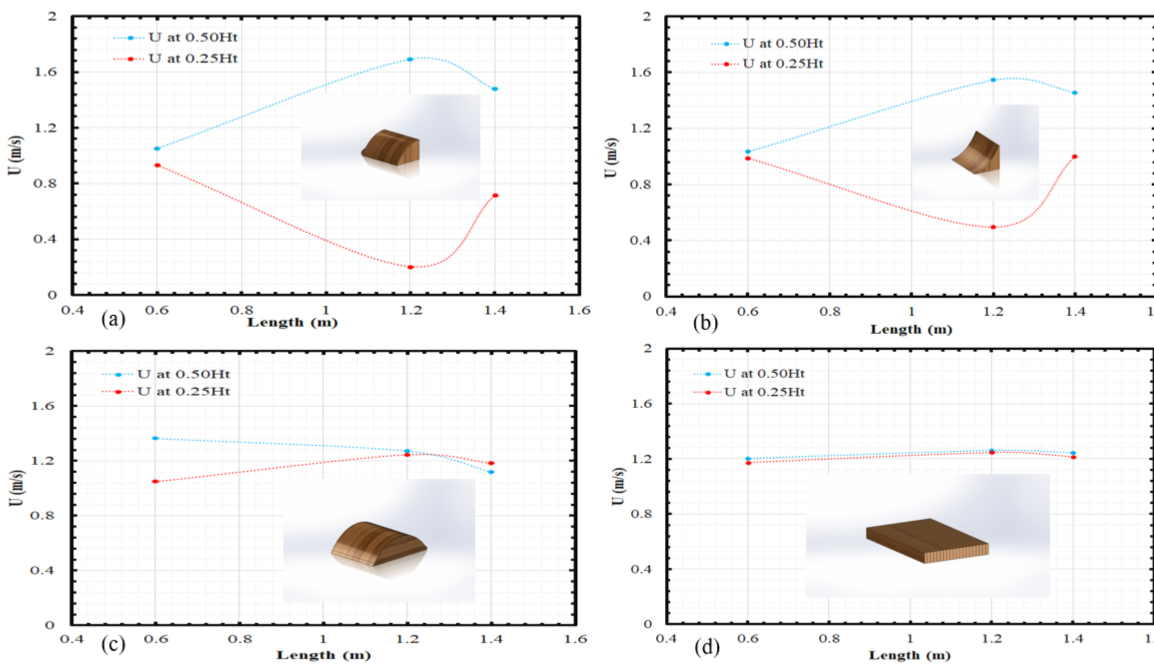

Figure 4.3: Streamwise flow velocity profiles obtained from the ADV with the turbine mooring anchors deployed 2 diameters upstream the turbine: (a) anchor A, (b) anchor B, (c) anchor C, and (d) anchor D

Figure 4.3 shows that anchors A and B are the best performing anchors compared to anchors C and D. This can be attributed to the height of the anchors as anchors A and B are the tallest of all the anchors as shown in Table 3.2. However, Figure 4.3a and b shows that the impact of the anchors occur in the upper column of the water tunnel as the figures shows velocity defect in the lower column of the water tunnel. If a HKT is deployed in this region, the benefit of these anchors will be mostly protection against debris, as power would reduce significantly.

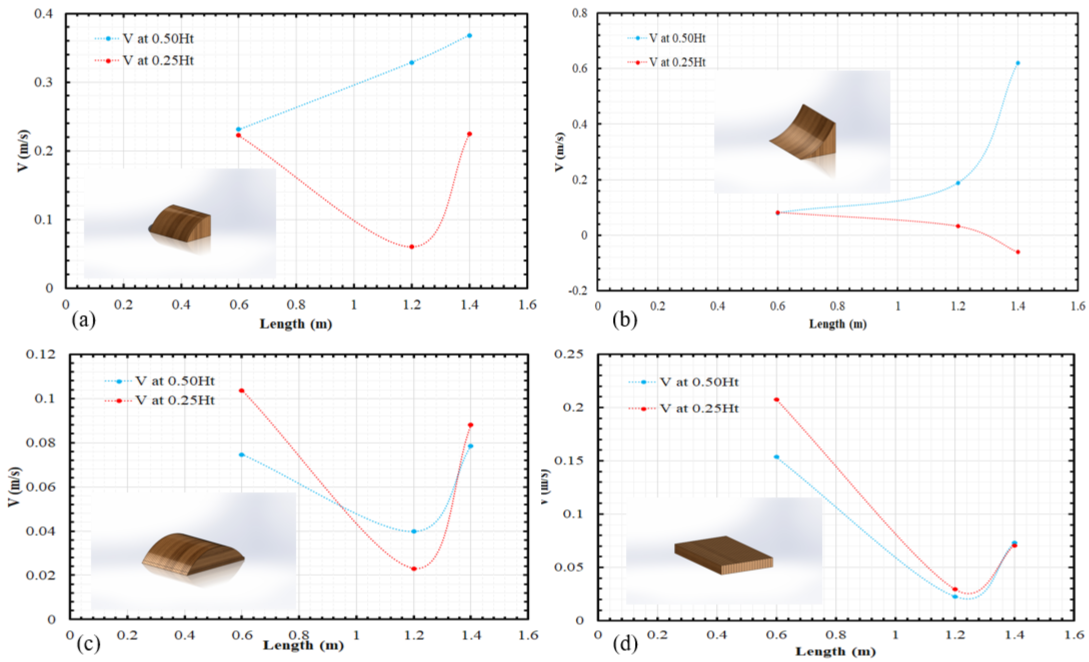

Figure 4.4: Spanwise flow velocity profiles obtained from the ADV with mooring anchors deployed 2 diameters upstream of turbine: (a) anchor A, (b) anchor B, (c) anchor C, and (d) anchor D

Figure 4.4 shows the spanwise velocity profile for anchors A to D, respectively, when deployed 2 diameters upstream of the turbine. From Figure 4.4a and b, the spanwise velocity increases in the upper column of the water tunnel as the flow progresses while in Figure 4.4c and d, the spanwise velocity decreases in the upper column. This behaviour is not only attributed to the height of the anchors but also to their geometries and cross sectional area. Figure 4.5 shows the vertical velocity profile for anchors A to D. From the figure, it can be seen that the vertical velocity profiles obtained with the turbine mooring anchors deployed 2 diameters upstream of the turbine shows the vertical velocity in the lower column increasing significantly for anchors A and B. This increase in their vertical velocity can be said to have contributed to the significant increase in streamwise velocity obtained from both anchors.

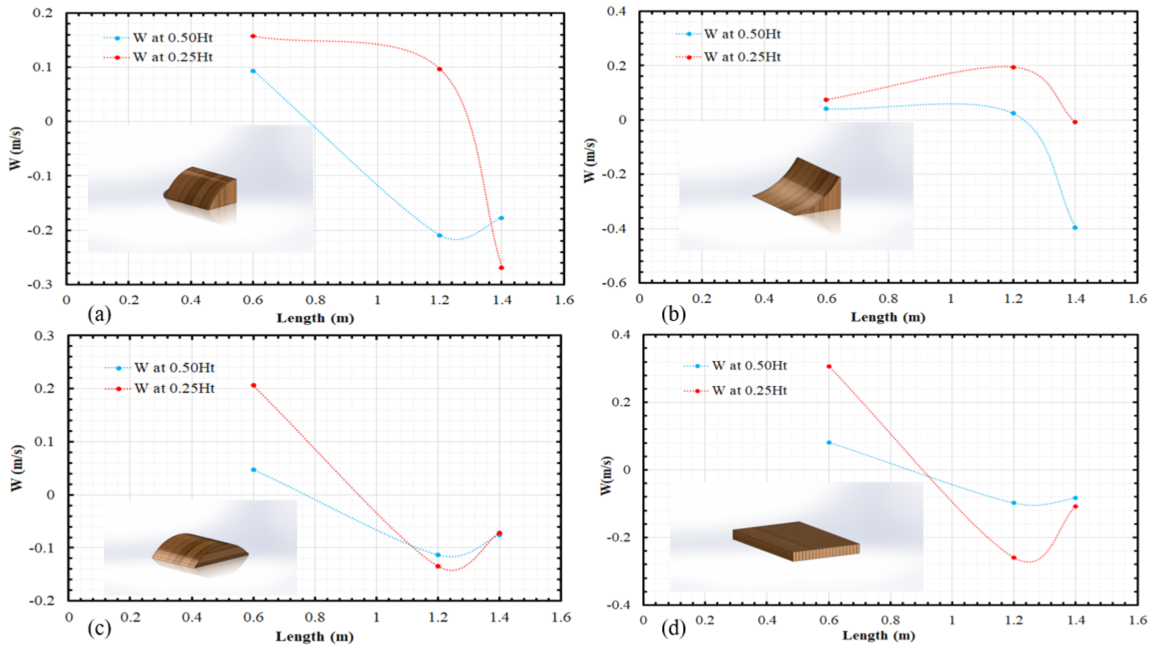

Figure 4.5: Vertical flow velocity profiles obtained from the ADV with mooring anchors deployed 2 diameters upstream of turbine: (a) anchor A, (b) anchor B, (c) anchor C, and (d) anchor D

4.3.2 Impact of mooring anchors at 3 diameters upstream of turbine

The performance curves obtained with the mooring anchors deployed 3 diameters upstream of the turbine show a similar trend with the performance curves obtained when the turbine mooring anchors were deployed 2 diameters upstream as shown in Figure 4.6. However, higher C_P values were obtained compared to when the mooring anchors were deployed 2 diameters upstream and when the turbine was tested in an unobstructed velocity. It was not possible to test 4 diameters upstream of the turbine and above due to geometrical tunnel constraints.

With the turbine mooring anchors deployed 3 diameter upstream, C_P values of 0.63, 0.61, 0.56 and 0.50 were obtained from the turbine corresponding to 31%, 29%, 23%

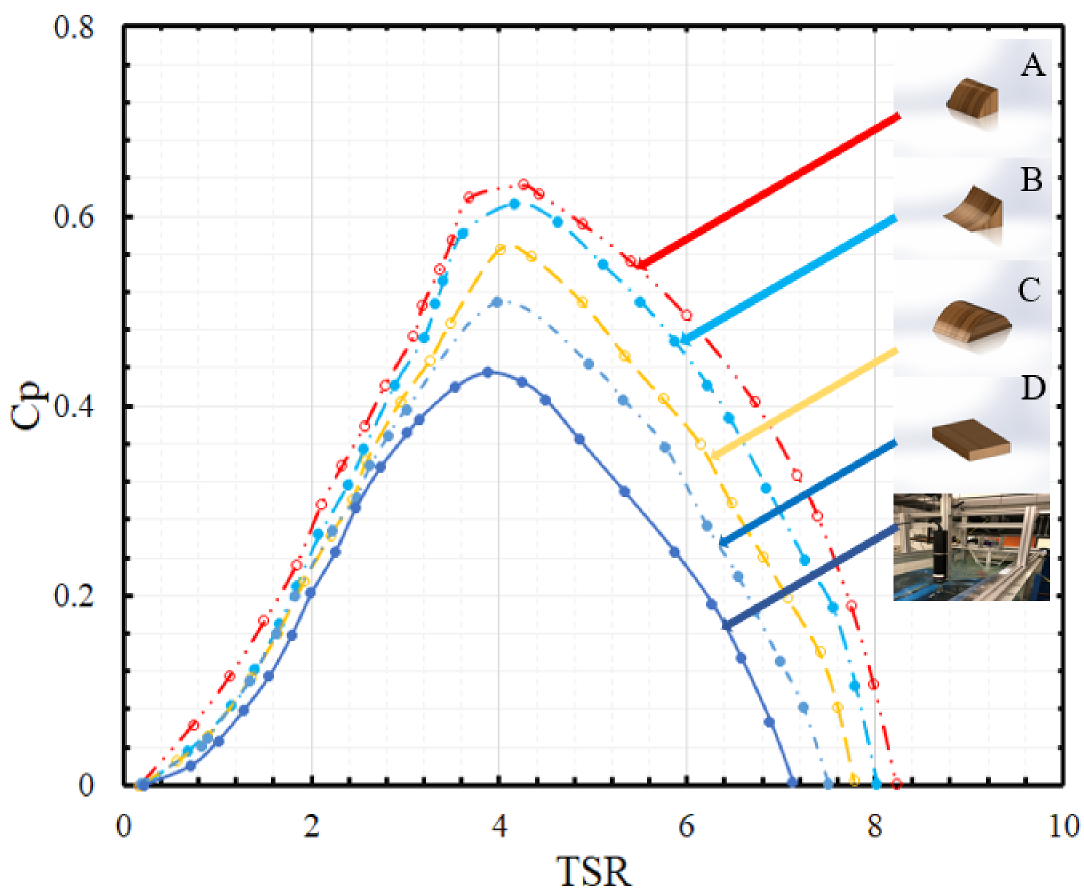

Figure 4.6: Performance curve obtained from the turbine with the mooring anchors deployed 3 diameters upstream. Figure also shows mooring anchor geometries: anchors A, B, C, and D tested with turbine.

and 14% improvement in performance for anchors A to D, respectively when compared to the C_P obtained from the turbine in an unobstructed velocity. This significant improvement can be attributed to significant increase in flow velocity caused by the upstream mooring anchors and the operation of the turbine well beyond the flow re-attachment point. A closer look at Figure 4.6 shows that, in agreement with literature and as described in Section 4.3.1, the performance curves partially fall on each other in the stall region of TSR less than 3. Also, the performance curves of the respective mooring anchors are observed to have peaked at a TSR higher than they peaked when deployed 2 diameters upstream of the turbine.

Average streamwise velocity of 1.47, 1.39, 1.30 and 1.29 m/s corresponding to anchors

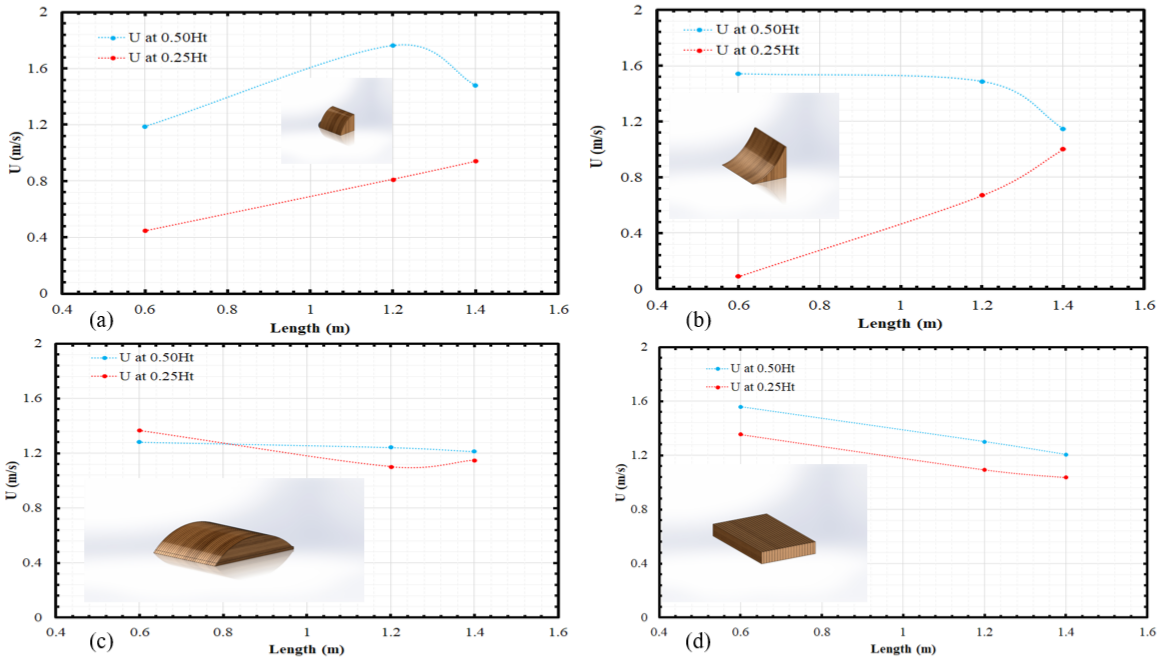

Figure 4.7: Streamwise flow velocity profiles obtained from the ADV with the turbine mooring anchors deployed 3 diameters upstream the turbine: (a) anchor A, (b) anchor B, (c) anchor C, and (d) anchor D

A to D, respectively were obtained with the mooring anchors deployed 3 diameters upstream of the turbine. Compared to the unobstructed velocity, the deployment of anchors A to D, 3 diameters upstream resulted to a 25%, 21%, 15% and 14% increase in streamwise velocity, respectively. Figure 4.7 shows the streamwise velocity profile for anchor A to D, respectively.

From Figure 4.7a and b, deploying the anchors 3 diameters upstream increases the velocity both in lower and upper column of the water tunnel. This behaviour is different compared to anchor C and D as seen in Figure 4.7c and d as figure shows the velocity decreasing as the flow progresses. This increase in streamwise velocity in the lower column using an anchor is consistent in trend with literature on topic of river kinetic turbine enhancement methods, such as the work done by Gaden and Bibeau [4]

Furthermore, higher spanwise velocity is observed in anchor A and B as shown in

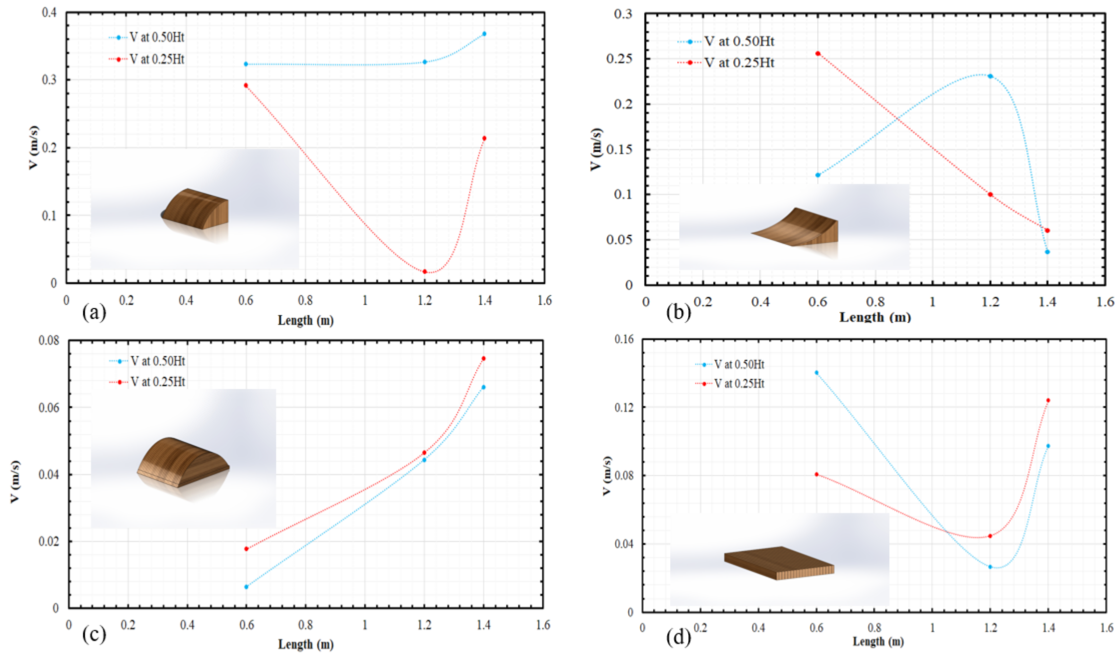

Figure 4.8: Spanwise flow velocity profiles obtained from the ADV with the turbine mooring anchors deployed 3 diameters upstream the turbine: (a) anchor A, (b) anchor B, (c) anchor C, and (d) anchor D

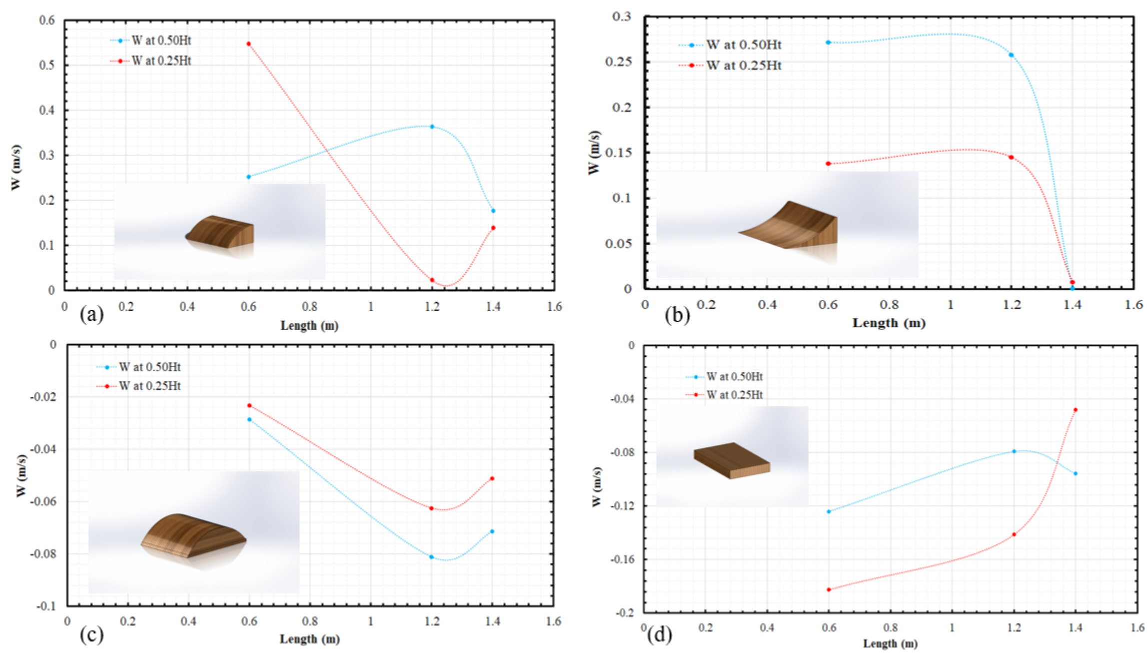

Figure 4.9: Vertical flow velocity profiles obtained from the ADV with the turbine mooring anchors deployed 3 diameters upstream the turbine: (a) anchor A, (b) anchor B, (c) anchor C, and (d) anchor D

Figure 4.8a and b compared to Figure 4.8c and d. This can be attributed to the difference in height and cross-sectional area of the anchors. Figure 4.9 shows the vertical velocity profile for anchor A to D, respectively obtained with the turbine mooring anchors deployed 3 diameters upstream. A closer look at the figure shows anchors A and B having the higher vertical velocities compared to anchor C and D. This can be attributed to anchors A and B having higher heights compared to the other anchors. Their high vertical velocities can also be said to have contributed to their higher streamwise velocity as well as higher performance from the turbine deployed downstream.

Table 4.2: Summary of results obtained with mooring anchors deployed 2 and 3 diameters upstream of the turbine and their percentage difference compared to the values obtained in the unobstructed flow test

Results with mooring anchors deployed 2-diameter upstream (without surface roughness)										
Anchor	**U(m/s)**	**V(m/s)**	**W(m/s)**	**TI(%)**	**Cp**	**Percentage increase (%)**				
						U	**V**	**W**	**TI**	**Cp**
A	1.41	0.31	0.09	6.39	0.58	21	97	78	65	25
B	1.34	0.29	0.11	5.02	0.56	17	97	81	55	23
C	1.25	0.07	0.04	4.80	0.50	12	86	50	53	14
D	1.23	0.08	0.03	3.91	0.45	10	88	33	42	4
Results with mooring anchors deployed 3-diameter upstream (without surface roughness)										
Anchor	**U(m/s)**	**V(m/s)**	**W(m/s)**	**TI(%)**	**Cp**	**Percentage increase (%)**				
						U	**V**	**W**	**TI**	**Cp**
A	1.47	0.34	0.26	4.39	0.63	25	97	92	49	32
B	1.39	0.12	0.18	3.98	0.61	21	92	89	43	29
C	1.30	0.06	0.06	3.02	0.56	15	83	67	25	23
D	1.29	0.08	0.11	2.98	0.51	14	88	82	32	14

From the results obtained, it can be seen that the mooring anchors had more positive impact on turbine when deployed 3 diameter upstream compared to when deployed 2 diameter upstream. Figure 4.10 shows graphically the difference in performance with the mooring anchors deployed while the summary of the results obtained with the mooring anchors deployed 2 and 3 diameter upstream and their rate of improvement when compared to the values stated in Table 4.1 are as shown in Table 4.2. From the result, it can be concluded that mooring anchors can used to increase turbine performance. Moreover, it could be possible that the C_p can be further increased beyond a diameter spacing of 3. In addition, more C_p could be potentially obtained by optimizing the height placement.

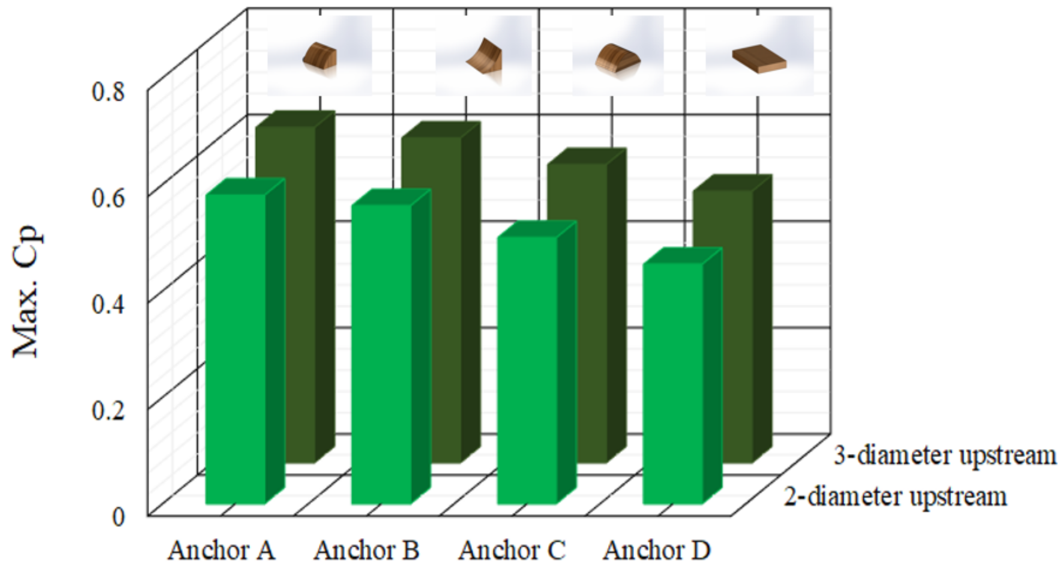

Figure 4.10: Chart of maximum C_p obtained with mooring anchors deployed 2 and 3 diameters upstream of the turbine

4.4 Surface roughness effect

Introduction of surface roughness into the water tunnel impacted the flow velocity and pattern due to macro-turbulence. With this introduction, an average velocity of 1.17 m/s was obtained from measurement using the ADV, which when compared to the unobstructed velocity, results to a 6% increase in streamwise velocity. Table 4.3 shows the summary of the parameters measured and values obtained with surface roughness distributed at the bed of the tunnel. For these tests, water height and pump power are kept constant to simulate river conditions.

Figure 4.11 shows the streamwise velocity profiles obtained with the surface roughness

Table 4.3: Summary of parameters measured and values obtained with surface roughness distributed at the bed of the water tunnel

Parameters	Values	Percentage increase (%)
Cp	0.45	4
U	1.17 m/s	6
V	0.02 m/s	50
W	0.35 m/s	94
T.I	5.50%	59

deployed in the water tunnel. From the figure, it can be seen that velocity increases and decreases in the upper and lower column of the tunnel, respectively as the flow progresses.

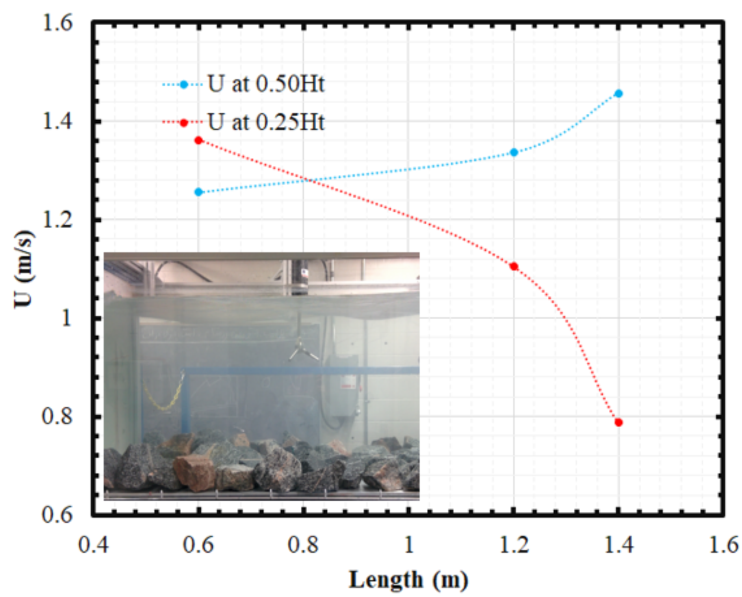

Figure 4.11: Streamwise flow velocity profiles obtained from the ADV with surface roughness of different sizes distributed at the bed of the water tunnel

The 6% velocity increase with surface roughness deployed in the water tunnel increased the C_p from 0.43 to 0.45. This performance improvement can be partially attributed to the macro-turbulent structures generated by the surface roughness in the lower column of the water tunnel, advecting to the upper column of the water tunnel. This shows that macro-turbulent structures generated by bluff bodies or objects in a flowing water can improve the performance of a HKT; a behaviour that has also been reported by Birjandi [17].

Furthermore, the introduction of surface roughness also impacted both the spanwise and vertical velocities. Figure 4.12a and b shows the spanwise and vertical velocities obtained with the surface roughness distributed at the bed of the water tunnel.

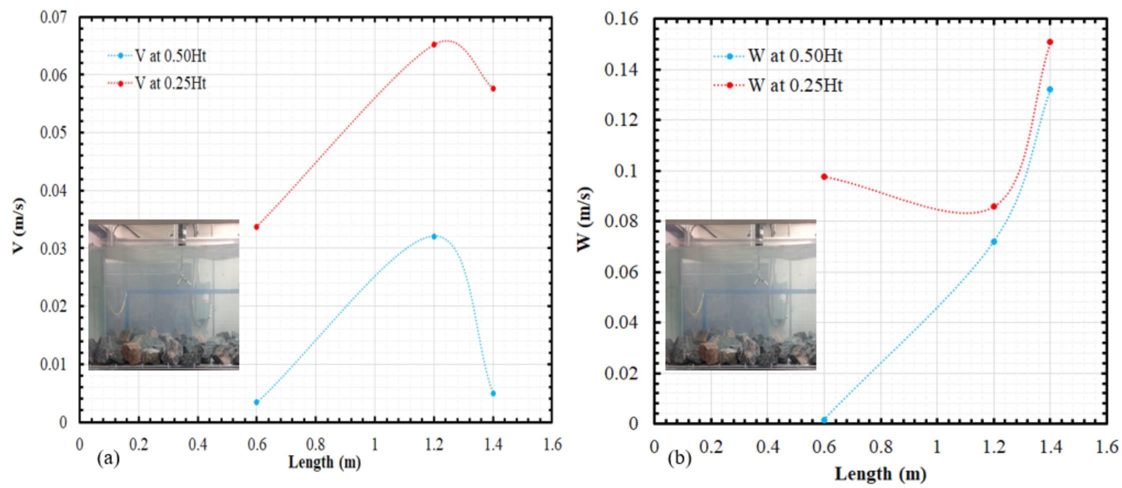

Figure 4.12: Spanwise and vertical velocity profiles with surface roughness distributed at the bed of the water tunnel: (a) spanwise velocity profile, and (b) vertical velocity profile

Interestingly, from Figure 4.12a, the spanwise velocity in the lower column of the water tunnel increases more than that of the upper column. This behaviour was also observed in the vertical velocity profile obtained as shown in Figure 4.12b. This can be attributed to increase in turbulence intensity and macro-turbulent structures due to the presence of surface roughness.

In terms of the Reynolds stresses, the impact of the surface roughness is also observed as shown in Figure 4.13. From the figure, the streamwise, spanwise and vertical velocity components of the Reynolds normal stresses agree in trend and magnitude both in the lower and upper column of the water tunnel. However, in terms of Reynolds shear stresses, there is disagreement amongst components. This can be attributed to difference in magnitude and size of the macro-turbulent structures due to different sizes and dimensions of the surface roughness as magnitude and size of

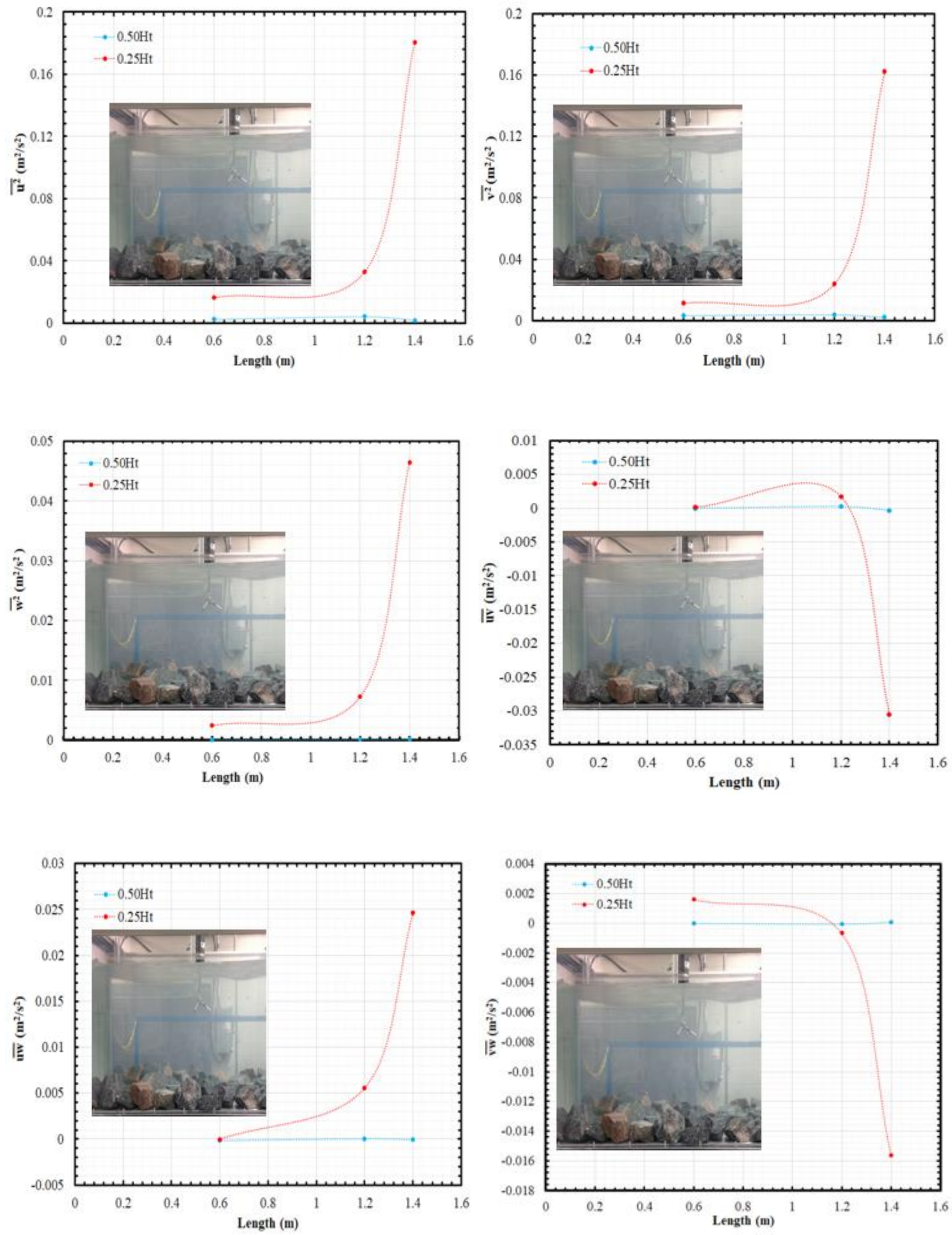

Figure 4.13: Reynolds stress profiles obtained from the ADV with surface roughness distributed at the bed of the water tunnel showing $\overline{u^2}$, $\overline{v^2}$, $\overline{w^2}$, $\overline{uv}$, $\overline{uw}$ and $\overline{vw}$

macro-turbulent structures are determined by the size and dimensions of the body or object causing it.

The surface roughness used in simulating a rough surface in the water tunnel were randomly selected. With an average Hr_{ave}/H_w ratio of 0.20 and total weight of 722.5 N, they were arranged in increasing height and weight in the water tunnel occupying 37% of the water tunnel bed area with the higher and heavier ones deployed downstream the tunnel to ensure the lighter ones are not swept away by the flow. However, for each test involving the mooring anchors, the surface roughness was rearranged using the same pattern resulting to eight different moves. Other parameters of the surface roughness used in this study are presented in Table 3.4.

4.5 Mooring anchors and bed surface roughness

Testing the scaled turbine with the mooring anchors deployed 2 and 3 diameters upstream and surface roughness distributed on bottom of the water tunnel impacts the flow velocity and in-turn the turbine performance. For these tests, rock placement and configuration employed in Section 4.4 was used as well as pump pressure and water height.

With the turbine mooring anchors deployed 2 diameters upstream, result show C_P values of 0.63, 0.60, 0.55 and 0.50 for anchors A to D, respectively, as shown in Figure 4.14. Compared to the reference C_P, these C_P values results to a 32%, 27%, 22% and 14% performance improvement for anchors A to D, respectively. This performance improvement observed can be attributed to the increase in streamwise velocity as results show average streamwise velocities of 1.48, 1.40, 1.30 and 1.27 m/s which corresponds to a 26%, 21%, 15% and 13% increase in streamwise velocity for anchors A to D, respectively. This increase in streamwise velocity can be attributed

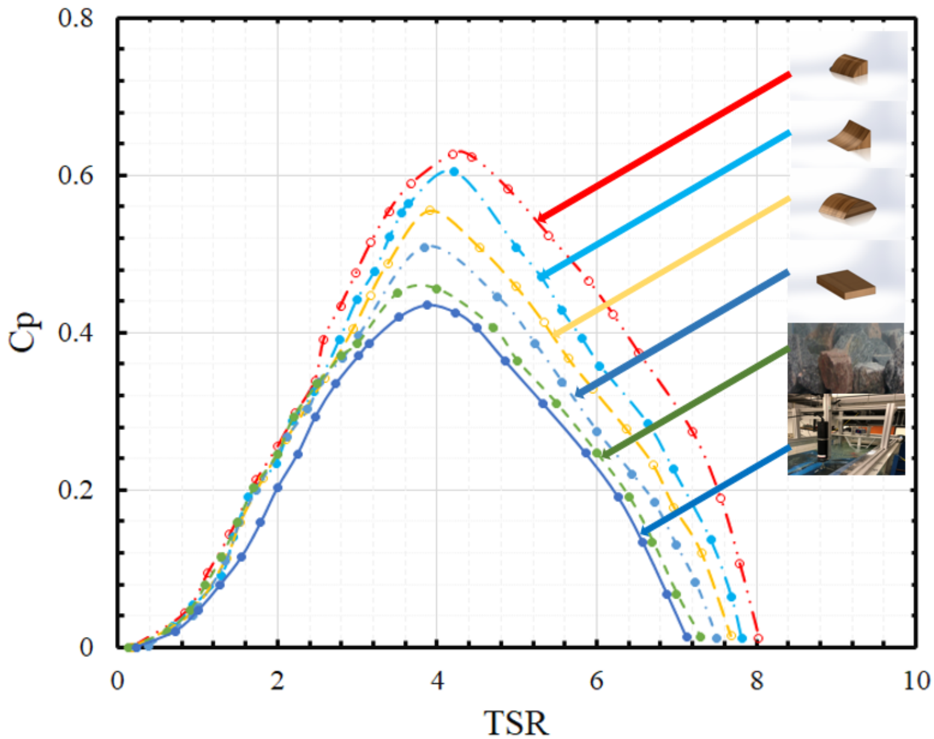

Figure 4.14: Performance curve obtained with the mooring anchors deployed 2 diameters upstream and surface roughness distributed at the bed of the water tunnel

to the geometries of the mooring anchors as well as the different sizes and magnitude of the macro-turbulent structures generated from bed surface roughness.

Furthermore, when the mooring anchors and surface roughness were deployed 3 diameters upstream, similar performance curves were obtained for the different turbine mooring anchors, as shown in Figure 4.15. However, higher C_P values were obtained compared to when the turbine mooring anchors were deployed 2 diameters upstream.

With anchors A to D deployed 3 diameters upstream, C_P values of 0.67, 0.64, 0.59 and 0.55, respectively were obtained which when compared to the reference C_P results to a 36%, 33%, 27% and 22% performance improvement for anchors A to D respectively. This increase in C_P obtained can be attributed to the increase in streamwise velocity and size of the macro-turbulent structures caused by the mooring anchors deployed

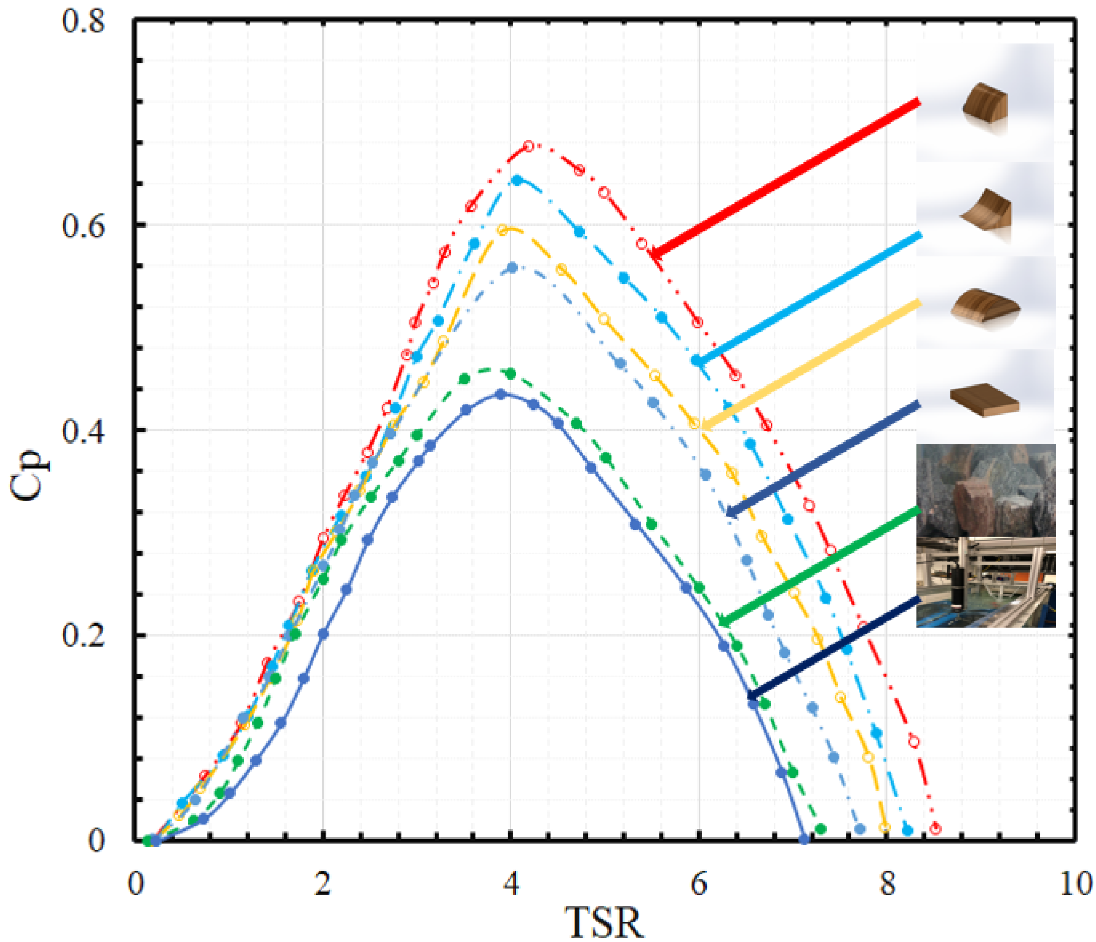

Figure 4.15: Performance curve obtained with the mooring anchors deployed 3 diameters upstream and surface roughness distributed at the bed of the water tunnel

at this location and the bed surface roughness distributed at the bed of the tunnel, respectively. Velocity result obtained showed an average streamwise velocity of 1.51, 1.47, 1.37 and 1.33 m/s for anchors A to D, respectively which when compared to the unobstructed flow velocity results to a 27%, 25%, 20% and 17% increase in streamwise flow velocity for anchors A to D, respectively.

From the results obtained as shown in Figure 4.16 and summarized in Table 4.4, it can be seen that the mooring anchors had more positive impact when deployed 3 diameters upstream compared to when they were deployed 2 diameters upstream, a behaviour that is consistent with and without the surface roughness distributed on

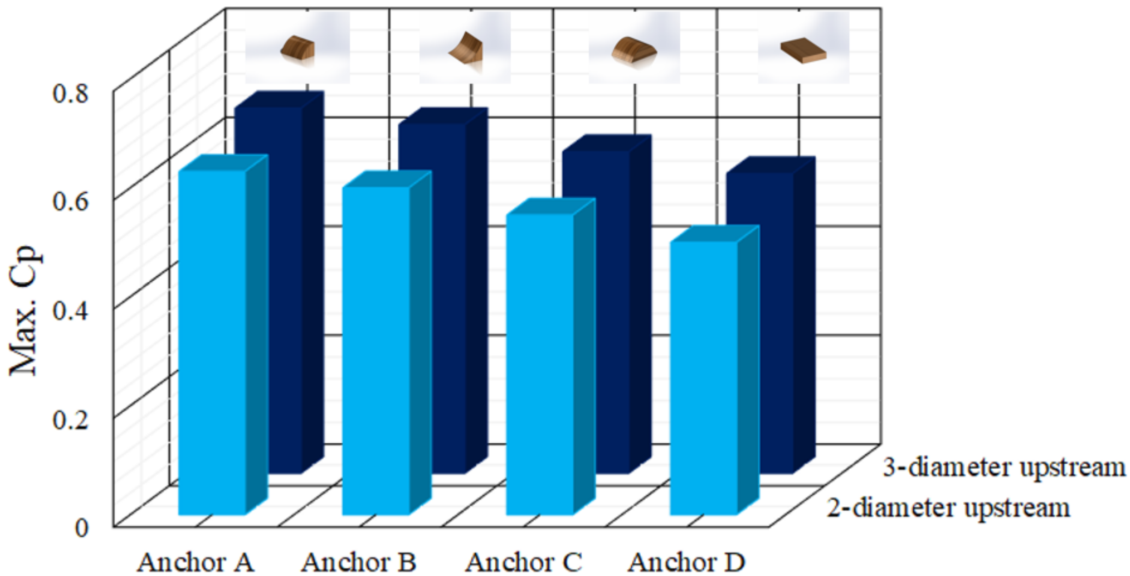

Figure 4.16: Chart of maximum C_p obtained with mooring anchors deployed 2 and 3 diameters upstream of the turbine with surface roughness distributed on the bed of the water tunnel

the bed of the water tunnel. This can be attributed to the turbine operating within the wake region of the mooring anchors deployed 2 diameters upstream and outside the wake region when deployed 3 diameters upstream. Furthermore, from the results obtained, it can be seen that apart from separation distance between the mooring anchors and the turbine, mooring anchor geometry and height as well as the size of the surface roughness impacted turbine performance.

From Table 4.4, it can be seen that the deployment of the turbine mooring anchors 2 and 3 diameter upstream and the distribution of surface roughness on the bed of the water tunnel resulted to a 14% to 36% turbine performance improvement. This shows that turbine performance can be enhanced if macro-turbulent structures are optimized. This behaviour was also observed in a numerical study by Gaden [4] on performance enhancement of river kinetic turbine using different mooring anchor geometries. Gaden identified anchors A and B used in this present study as the best performing anchors due to their geometry, height and separation distance from

Table 4.4: Summary of results obtained with mooring anchors deployed 2 and 3 diameters upstream of the turbine with surface roughness distributed at the bed of the water tunnel and their percentage difference compared to the values obtained in the unobstructed flow test

Results with mooring anchors deployed 2-diameter upstream (with surface roughness)										
Anchor	**U (m/s)**	**V (m/s)**	**W (m/s)**	**TI (%)**	**Cp**	**Percentage difference (%)**				
						U	**V**	**W**	**TI**	**Cp**
A	1.48	0.06	0.78	8.91	0.63	26	83	97	75	32
B	1.40	0.04	0.57	8.79	0.60	21	75	96	74	27
C	1.30	0.03	0.45	5.79	0.55	15	67	95	61	22
D	1.27	0.03	0.42	5.24	0.50	13	67	95	57	14
Results with mooring anchors deployed 3-diameter upstream (with surface roughness)										
Anchor	**U (m/s)**	**V (m/s)**	**W (m/s)**	**TI (%)**	**Cp**	**Percentage difference (%)**				
						U	**V**	**W**	**TI**	**Cp**
A	1.51	0.19	0.75	8.21	0.67	27	95	97	73	36
B	1.47	0.08	0.69	6.48	0.64	25	88	97	65	33
C	1.37	0.06	0.53	6.01	0.59	20	83	96	63	27
D	1.33	0.05	0.49	5.18	0.55	17	80	96	57	22

the turbine deployed downstream. The numerical study concluded that turbine improvement of 30% was observed when the mooring anchors were deployed 7.5 m upstream the turbine compared to when they were deployed 2.5 m upstream of the turbine.

Table 4.5 shows the Reynolds normal and shear stresses obtained with surface roughness distributed at the bed of the tunnel and the mooring anchors 2 and 3 diameters upstream of the turbine. From the table, it can be seen that $\overline{uw}$ has higher order of magnitude compared to the other shear stresses, $\overline{uv}$ and $\overline{vw}$, most especially with the mooring anchors deployed 2 diameters upstream. The higher $\overline{uw}$ observed with the mooring anchors deployed 2 diameter upstream can be attributed to the mooring anchors been closer to the larger size surface roughness while the higher $\overline{uw}$ obtained from both locations of the mooring anchors can be attributed to increase in streamwise and vertical velocity caused by the mooring anchors.

However, the order of magnitude of the streamwise, spanwise and vertical components

Table 4.5: Reynolds stresses obtained with mooring anchors deployed 2 and 3 diameters upstream of the turbine and surface roughness distributed at the bed of the tunnel

Reynolds stresses with mooring anchor 2 diameter upstream and surface roughness						
Anchors	$\overline{u^2}$ (m^2/s^2)	$\overline{v^2}$ (m^2/s^2)	$\overline{w^2}$ (m^2/s^2)	$\overline{uv}$ (m^2/s^2)	$\overline{uw}$ (m^2/s^2)	$\overline{vw}$ (m^2/s^2)
A	0.0448	0.0426	0.0695	-0.0003	0.2202	0.0002
B	0.0204	0.0445	0.0644	-0.1913	0.2245	0.0545
C	0.0504	0.0482	0.0592	0.0143	0.1029	-0.0245
D	0.0572	0.0354	0.0509	0.0931	0.1082	-0.0224
Reynolds stresses with mooring anchor 3 diameter upstream and surface roughness						
Anchors	$\overline{u^2}$ (m^2/s^2)	$\overline{v^2}$ (m^2/s^2)	$\overline{w^2}$ (m^2/s^2)	$\overline{uv}$ (m^2/s^2)	$\overline{uw}$ (m^2/s^2)	$\overline{vw}$ (m^2/s^2)
A	0.0424	0.0405	0.0453	-0.0014	0.0197	0.0014
B	0.0454	0.0499	0.0464	0.0027	0.0142	0.0040
C	0.0357	0.0320	0.0249	-0.0069	0.0086	-0.0001
D	0.0281	0.0250	0.0212	0.0010	0.0063	0.0034

of the Reynolds normal stresses remained the same at both locations of the mooring anchors though the vertical components seem to be higher which may be due to the height of the mooring anchors.

4.6 Field test results and analysis

A time-dependent series of velocity measurements were carried out to characterize the flow at the CHTTC located on the Winnipeg River downstream of the Seven Sisters Falls hydro plant dam. A novel method as discussed in Section 3.8 was applied to measure the velocity throughout the water column using an ADV to contribute to the design and optimization of power production from a HKT. The ADV measures mean and fluctuating velocity components at a 64 Hz frequency with data obtained from eight streamwise, three spanwise and an average of six channel depths across the channel. Tests were performed between 2.1 to 2.7 m/s water flow velocity while the data obtained were processed with the ADV post-processing code as discussed in Section 1.4.2 before further calculations and analysis are carried out.

With an average correlation of 88% and SNR of 25.95% obtained after post processing, the data is said to be of good quality and hence gives the confidence for further analysis.

4.6.1 Velocity profile

The result of the field test obtained using the ADV from the measurement locations as described in Section 3.8.1 yielded time-mean streamwise velocities in the range of 1.95 to 2.73 m/s, with measurement location CP-F having the lowest velocities and measurement location CP-G having the highest velocity. Table 4.6 shows the summary of the results obtained from the field test. With the result shown in Table 4.6, it is possible to identify the locations with the highest velocities for HKT deployment. However, at the end of the test period, an average velocity of 2.02 and 2.24 m/s were obtained from measurement location CP-F and CP-G, respectively with the average volumetric discharge from the dam during tests as 875.1 m^3/s. The volumetric discharge from the dam amongst other factors determines the flow velocity obtainable from the channel. From the results obtained, evidence of the obstruction caused by the turbine mooring anchors and structures between location CP-F and CP-G show in measurements as result show a 10% increase in streamwise velocity downstream the turbine mooring anchors and structures.

Figures 4.17 and 4.18 shows the streamwise velocity profile obtained from measure-

Table 4.6: Results obtained from the CHTTC measurements along the Seven Sisters channel. Measurement locations are as described in Section 3.8.1 and shown in Figure 3.12

Measurement location	**Profile**	**Umean (m/s)**	**Vmean (m/s)**	**Wmean (m/s)**	**ADV correlation (%)**	**SNR**	**TI (%)**
CP-A	A1	2.27	0.21	0.01	89.14	25.46	11.76
	A2	2.44	0.20	0.18	71.21	27.39	21.36
	A3	2.40	0.11	0.40	76.16	28.02	14.22
CP-B	B1	2.73	0.54	0.30	81.62	28.42	11.58
	B2	1.99	0.09	0.03	89.23	25.02	12.54
	B3	2.29	0.45	0.19	86.11	25.83	12.88
CP-C	C1	2.08	-0.21	0.16	88.30	25.89	11.30
	C2	2.19	-0.16	0.12	88.32	25.36	11.55
	C3	2.14	-0.22	0.14	90.99	25.11	10.58
CP-D	D1	2.48	-0.44	0.16	90.74	25.69	9.93
	D2	2.52	-0.38	0.15	89.82	25.51	14.41
CP-E	E1	2.50	0.17	0.19	93.07	25.34	8.50
	E2	2.46	0.63	0.32	93.18	25.30	8.44
	E3	2.00	0.60	0.12	93.56	24.76	10.46
CP-F	F1	1.97	-0.43	0.06	89.81	24.42	12.08
	F2	2.13	-0.46	0.17	91.53	24.50	9.10
	F3	1.95	-0.45	0.05	93.52	24.61	9.55
Mooring anchor location							
CP-G	G1	2.20	0.73	0.09	85.01	28.98	14.46
	G2	2.28	0.22	0.14	92.13	27.50	9.32
Mooring anchors are located between measurement location CP-F and CP-G while HKTs are usually anchored behind measurement location CP-G							

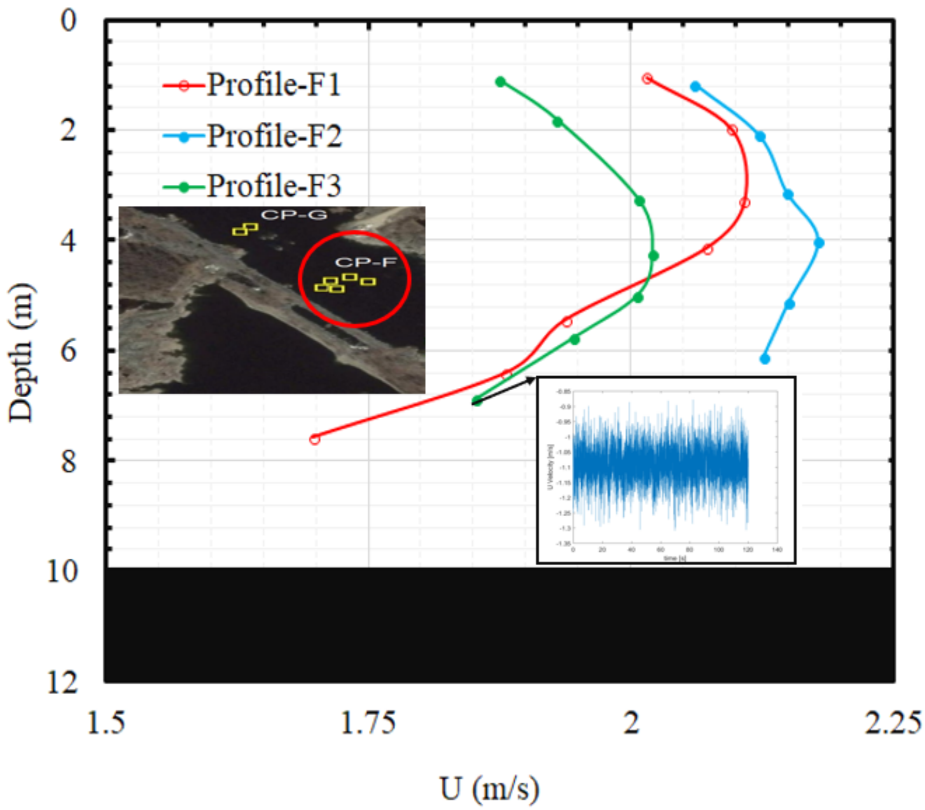

Figure 4.17: Streamwise flow profile obtained from the ADV for points of interest - F1, F2 and F3 within measurement location CP-F. The dark area indicates the bed of the river. The mean value obtained from a time series at the corresponding depth is indicated as a data point along the spline of each profile. An example of one of the time series plots is also shown.

ment location CP-F and CP-G, respectively. From the figures, the profiles obtained agree in trend and magnitude and also with other profiles obtained from other measurement locations in the channel; though not related to this research. However, in Figure 4.18 it can be observed that the increase in streamwise velocity occur between measurement depths of 3 and 6 m as the flow separated by mooring anchors and structures re-attaches downstream. Meanwhile, a near-surface measurement at measurement location CP-F and CP-G also shows an 8.8% increase in streamwise velocity. Mooring anchor geometry and measurement locations can be found in Section 3.8.

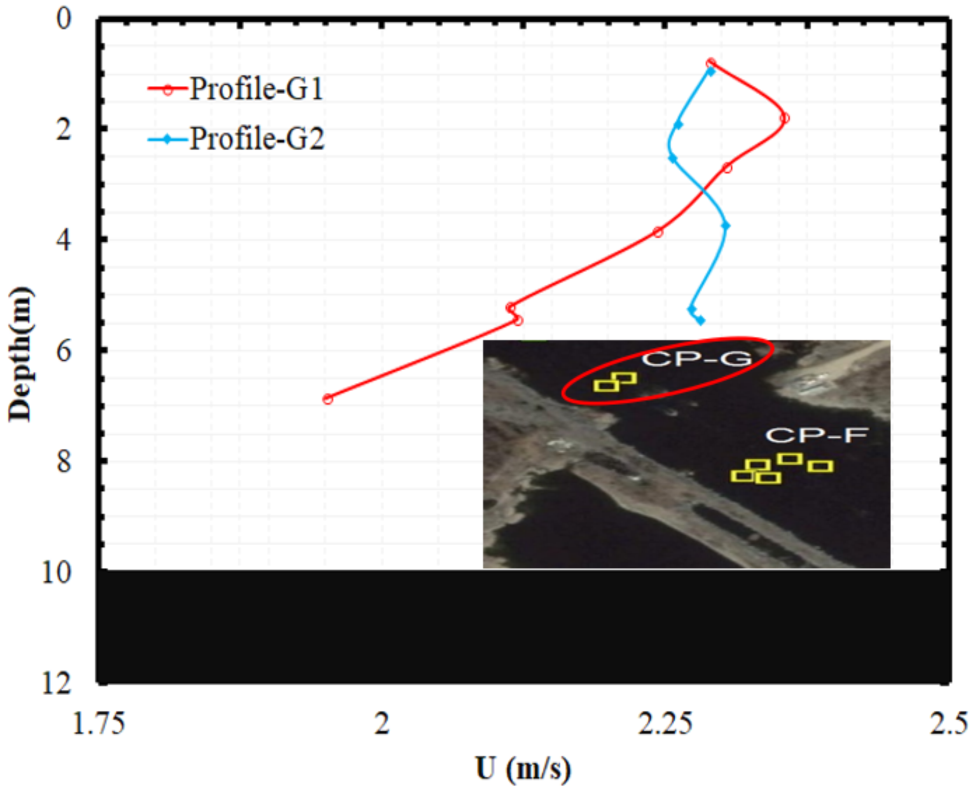

Figure 4.18: Streamwise flow profile obtained from the ADV for points of interest - G1 and G2 within measurement location CP-G. The dark area indicates the bed of the river. The mean value obtained from a time series at the corresponding depth is indicated as a data point along the spline of each profile. The mooring anchors are located at a length to diameter ratio of 15 downstream measurement location CP-F; CP-F and CP-G are separated by a length to diameter ratio of 36.

Figure 4.19 show the spanwise and vertical velocity profiles obtained from measurement location CP-F and CP-G. Result obtained show a 51% and 60% increase in spanwise and vertical velocities, respectively at measurement location CP-G compared to measurement location CP-F. From Figure 4.19a and b, it can seen that the spanwise velocity profiles show a similar trend of decreasing towards the bottom of the channel. Furthermore, from Figure 4.19c it can be seen that the profiles obtained do not a follow a similar trend though they decrease as the channel depth increases while in Figure 4.19d, shows vertical velocity increases with depth. This can be attributed to the flow structures generated by the mooring anchors and structures with magnitude as large as their dimensions.

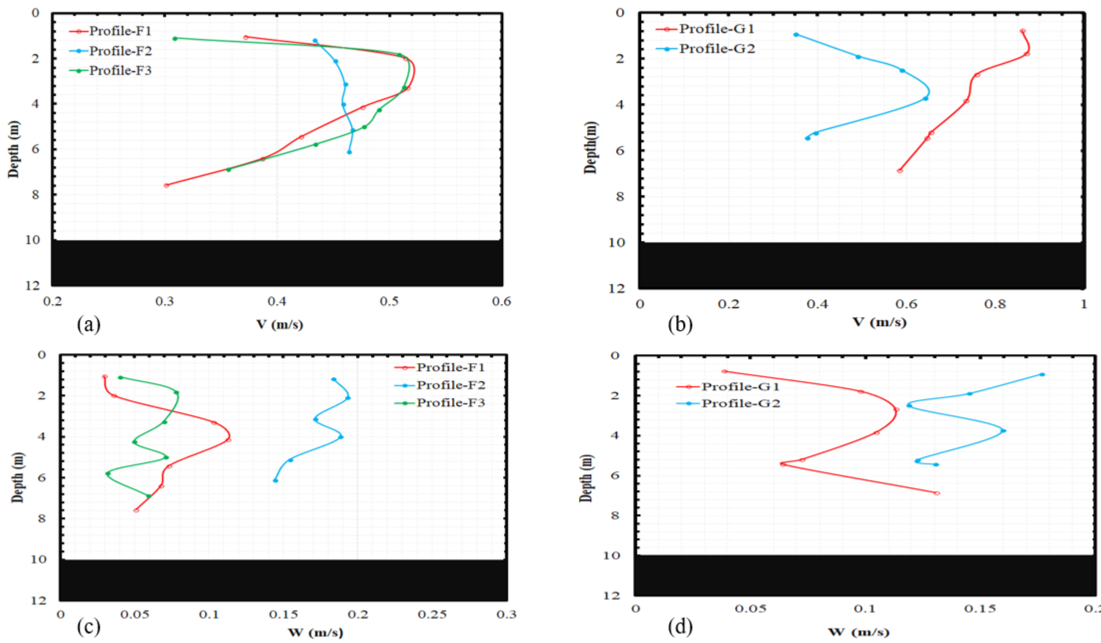

Figure 4.19: Spanwise and vertical velocity profiles obtained from the ADV at the measurement locations CP-F and CP-G: a) spanwise profiles at CP-F, b) spanwise profiles at CP-G, c) vertical profiles at CP-F, and d) vertical profiles at CP-G

Furthermore, from the results obtained and summarized in Table 4.6, it is observed that the obstruction caused by the mooring anchors and structures resulted to an average spanwise and vertical velocity of 0.48 and 0.12 m/s, respectively at measurement location CP-G; a 6% and 25% increase in spanwise and vertical velocity respectively compared to the average values of the same parameters obtained at measurement location CP-F. However, at the time of these tests, the CHTTC did not have turbine whose position could be placed in the water column.

4.6.2 Turbulence statistics

For deployment location, durability and performance of a hydrokinetic turbine, information on turbulence statistics is important. Referred to as the turbulence level in a flow, Turbulence intensity, I, is given by

$$I = \frac{std(U)}{U_{ave}}. \tag{4.1}$$

A turbulence intensity of less than 1% is a low-turbulence [85] which is usually seen in controlled environments like a laboratory facility while a turbulence intensity between 1% and 5% is a medium-turbulence case which is observed in shallow rivers of low velocity and downstream of generating grids that are turbulent [47]. A high-turbulence case is when the turbulence level is between 5% and 20% and is observed near gravel-beds of rivers and channels [86].

From the turbulence intensity data obtained from the measurement locations and shown in Table 4.6, the Seven Sisters Channel has a high turbulence level when the flow is obstructed upstream and downstream of the turbine mooring structures. With an average turbulence intensity of 10% and 12% for measurement location CP-F and CP-G, respectively, an increase of 14% in turbulence intensity is observed in

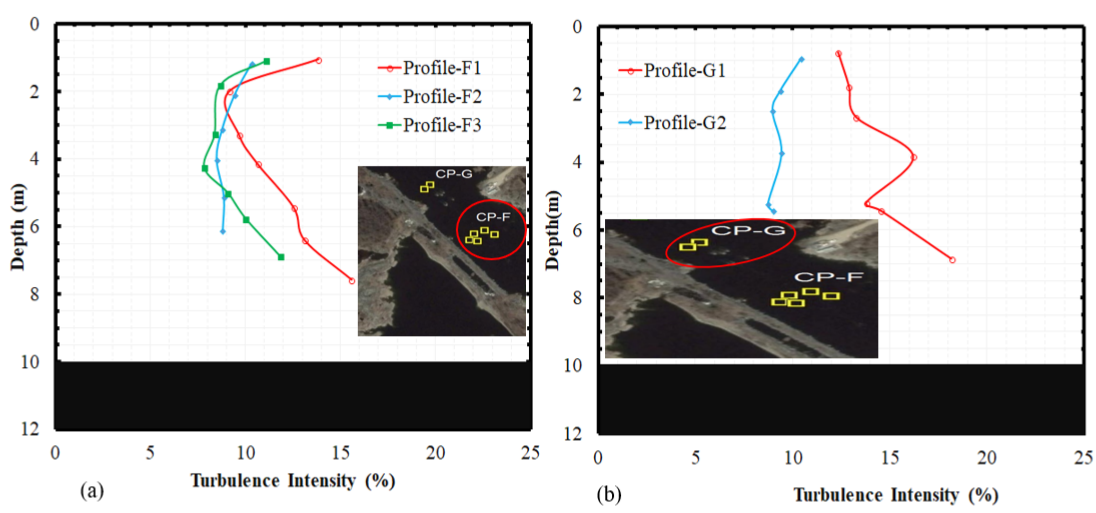

Figure 4.20: Turbulence intensity profiles obtained from the ADV: a) measurement location CP-F, and b) measurement location CP-G with mooring anchors placed as shown in Figure 3.12 length to diameter ratio of 15 from CP-F. Measurement location CP-F and CP-G are 36 length to diameter ratio apart

.

measurement location CP-G compared to CP-F. A near-surface measurement result also show a 9.9% increase in turbulence intensity because of the obstruction caused by the turbine mooring anchors. Change in flow pattern because of the obstruction caused by the turbine mooring anchors and structures resulted to an increase in turbulence intensity as seen in the turbulence intensity profiles obtained using the ADV shown in Figure 4.20. Also, from Figure 4.20, it can be seen from both measurement locations that as the measurement depth increases, the turbulence intensity increases as well. This observation is consistent with literature as seen in a study on turbulence in open channels by Kaji [87].

Comparison between the turbine mooring anchors at the CHTTC and turbine mooring D used in the laboratory experiment which is a scaled model of the mooring anchor at the CHTTC as described in Section 3.3 shows that the mooring anchors impacted the flow around them significantly. From the results obtained and as shown in Table 4.7, it can be seen that the mooring anchors at the CHTTC with an average height of 0.9 m, occupying 9% of the water column impacted the flow pattern resulting to a 10% increase in streamwise velocity between the two measurement locations while the deployment of mooring anchor D which has a 5.5 cm height and occupies 9% of the water height in the water tunnel, resulted to a 24%, 1.03 m/s to 1.35% increase in streamwise velocity.

Furthermore, the turbulence intensity downstream the mooring anchors at the CHTTC shows a 27% increase compared to the turbulence intensity obtained upstream while a 47% increase in turbulence intensity is obtained with mooring anchor D deployed in the water tunnel. These impacts by the mooring anchors on the flow around them can be attributed to the geometry of the anchors as well as the breaking of large eddies generated by the mooring anchors into smaller eddies. Other parameters impacted by the mooring anchors and magnitude of their impact are summarized in Table 4.7.

Table 4.7: Summary of parameters impacted by mooring anchors at the CHTTC and mooring anchor D deployed in the water tunnel

Parameters	**Mooring anchors at CHTTC**			**Mooring anchor D deployed in water tunnel**		
	Upstream value	**Downstream value**	**Percentage increase (%)**	**Upstream value**	**Downstream value**	**Percentage increase (%)**
U	1.89 m/s	2.11 m/s	10	1.03 m/s	1.35 m/s	24
V	0.37 m/s	0.48 m/s	23	0.09 m/s	0.14 m/s	36
W	0.08 m/s	0.13 m/s	38	0.22 m/s	0.31 m/s	29
TI	10%	14%	27	2.65%	5.01%	47

4.6.3 Turbulent kinetic energy

Turbulent flow can be referred to as an irregular pattern of flow caused by predicted or unpredicted flow velocity or pressure change. Flow shear or disruption caused by upstream structures such as bridge piers, mooring anchors and structures, friction and buoyancy are some of the factors that create turbulence in flows which are characterized by different length scales of eddies. Eddies caused by mooring anchors could be large or small depending on the size and geometry of the mooring anchors. Eddies contain some level of energy with large scale eddies containing higher energy level in comparison to small scale eddies [88]. The high energy level contained by large scale eddies is obtained from the mean flow or from one another. Turbulent kinetic energy is seen to be lower in rivers or water bodies were the energy required for turbulence is generated by the mean flow compared to kinetic energy of the mean flow.

The obstruction caused by these mooring anchors and structures leads to disruption in the velocity pattern in the channel which results to a low flow velocity around the structures. This low flow velocity created upstream and around the structures, results to a negative velocity gradient in the steady flow. The energy contained in the large

Table 4.8: Mean flow velocity and turbulent kinetic energy values obtained from measurement locations CP-F and CP-G

Measurement location	**Profile**	**Mean velocity (m/s)**	**Turbulent kinetic energy (m^2/s^2)**
CP-F	F1	1.97	0.09
	F2	2.13	0.06
	F3	1.95	0.05
CP-G	G1	2.19	0.17
	G2	2.28	0.07

eddies and the mean flow cascades into small eddies because of the shear force created by the negative velocity gradient in the steady flow. The high kinetic energy carried by the mean flow is due to the high turbulence level of the channel. From Table 4.8, it can seen that the mean velocity of the flow remained higher than the turbulent kinetic energy in all the profiles upstream and downstream of the turbine mooring structures but decreased in profiles where the turbulent kinetic energy increased. This increase in the turbulent kinetic energy in these profiles can be attributed to energy cascade to small eddies from the mean velocity of the flow.

4.6.4 Reynolds stresses

In theory of turbulence Reynolds stress tensor is a very important concept. Referred to in velocity fluctuations as the average momentum flux due to turbulence, Reynolds stress tensor consists of diagonal components known as the normal stresses and off-diagonal components known as the shear stresses. As a symmetric type of tensor, Reynolds shear stress consists of just three components namely: $\overline{uv}$, $\overline{vw}$ and $\overline{uw}$ where u, v and w, respectively represents the streamwise, spanwise and vertical velocity fluctuation components.

Figures 4.21 and 4.22 shows the Reynolds stress profiles obtained from measurement

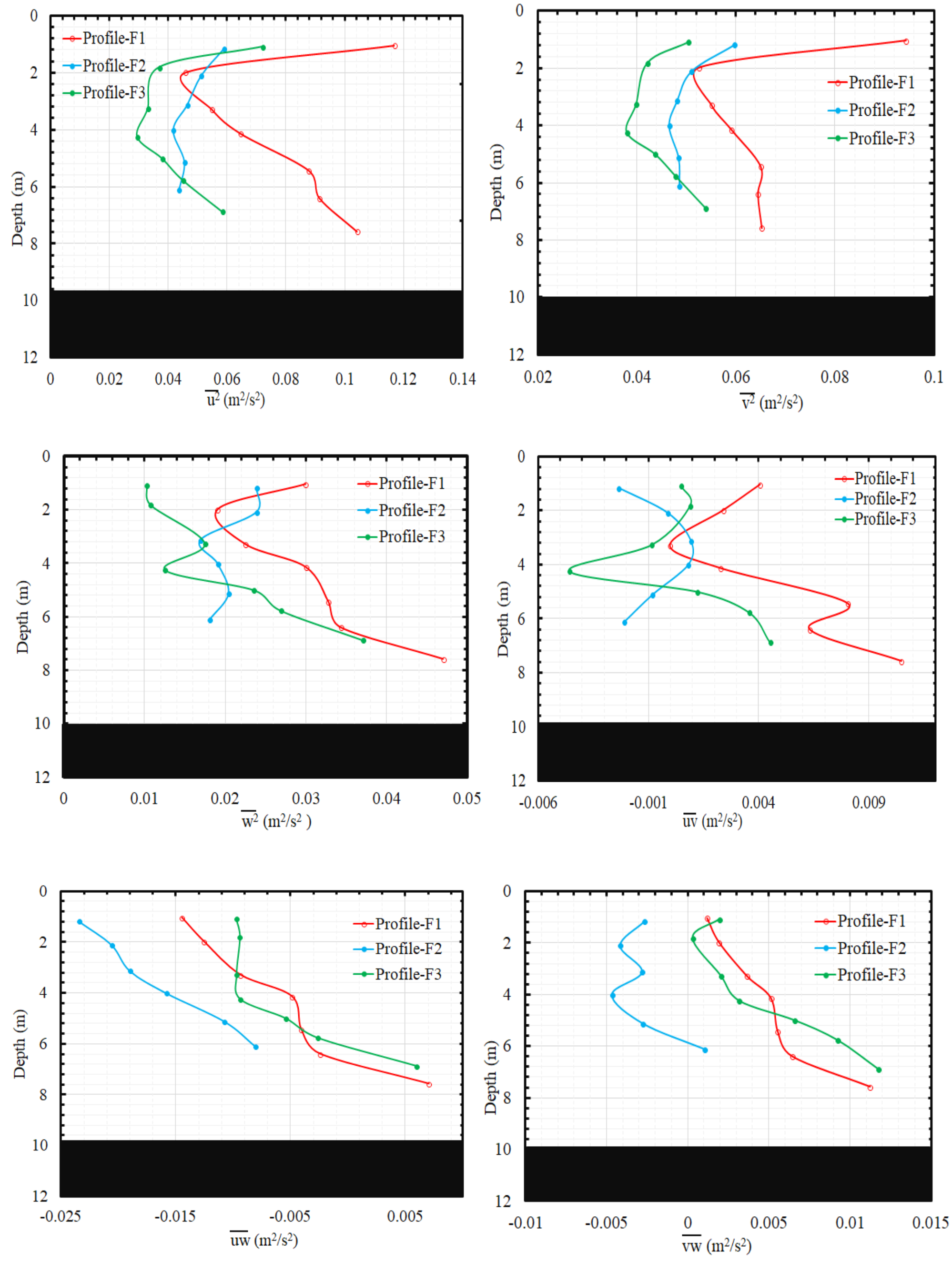

Figure 4.21: Reynolds stress profiles for measurement location CP-F: a) upper row showing Reynolds normal stress components for $\overline{u^2}$, $\overline{v^2}$, $\overline{w^2}$, and b) lower row showing Reynolds shear stress components for $\overline{uv}$, $\overline{uw}$, $\overline{vw}$

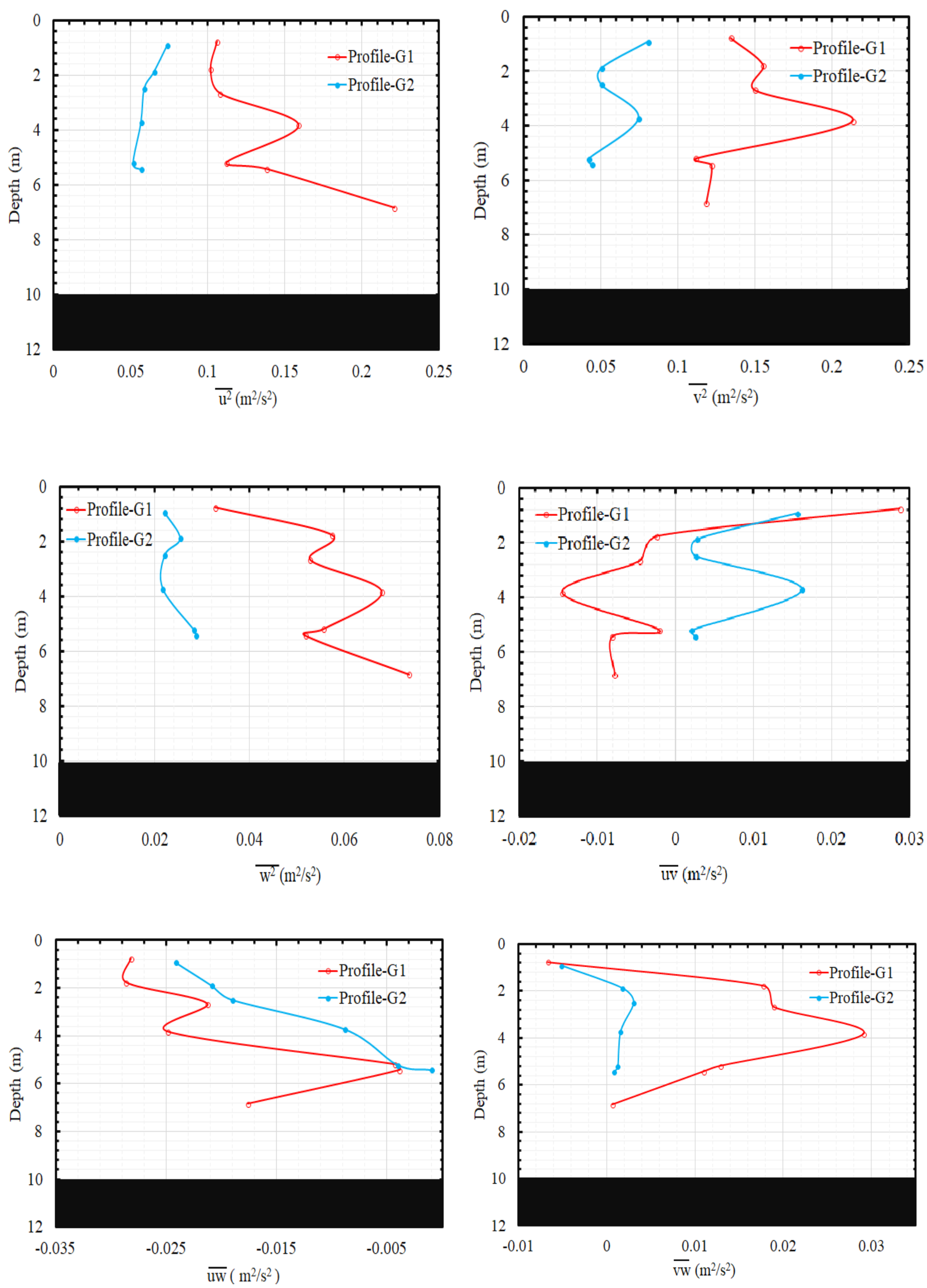

Figure 4.22: Reynolds stress profiles for measurement location CP-G: a) upper row showing Reynolds normal stress components for $\overline{u^2}$, $\overline{v^2}$, $\overline{w^2}$, and b) lower row showing Reynolds shear stress components for $\overline{uv}$, $\overline{uw}$, $\overline{vw}$

location CP-F and CP-G, respectively. From Figure 4.21, it can be seen that the streamwise, spanwise and vertical components of the Reynolds normal stresses agree in trend and magnitude while increasing with an increase in measurement depth. Similar agreement in trend and magnitude is also observed in the Reynolds shear stresses as well. Furthermore, in Figure 4.22, it can be seen the streamwise, spanwise and vertical components of the Reynolds normal stress agree in trend and magnitude while the Reynolds shear stresses disagree.

This disagreement can be attributed to the presence of vertical turbulent eddies, also referred to as boils. These boils originate at the point of flow reattachment and propagate to the water surface due to self-advection with its magnitude depending on the size of the object causing the obstruction [89]. Though boils were physically observed at the water surface during the tests, detailed investigation and analysis were not possible due to lack of underwater thermal camera for flow visualization. Interestingly, Figure 4.21 and 4.22 shows that turbulence is a function of direction and location. It can also be concluded from these plots that the turbulence at the CHTTC is non-homogeneous and non-isotropic.

4.6.5 Power density

Using Equation 1.1 and assuming a coefficient of performance, Cp; which for this study is set to the ideal Betz limit of 0.59 and water density, ρ of 1000 kg/m^3, power density was calculated at each of the measurement locations to determine the power density at each location. From the result obtained and as shown in Table 4.9, it can be seen that measurement location CP-G; the measurement location downstream the mooring anchors and structures with a power density of $3,496$ W/m^2 has more power density compared to measurement location CP-F with a power density of $2,850$ W/m^2 which is a 19% increase in power density between the two measurement locations.

This increase can be attributed to measurement location CP-G having more flow velocity than measurement location CP-F. This increase in flow velocity is invariably because of the turbulence and breaking of eddies caused by the turbine mooring anchors and structures located between measurement location CP-F and CP-G.

Table 4.9: Power density at each measurement location

Measurement location	Max. power density (W/m^2)
CP-A	4,285
CP-B	6,002
CP-C	3,098
CP-D	4,720
CP-E	4,609
CP-F	2,850
CP-G	3,496
Max	**6,002**
Min	**2,850**

Chapter 5

Conclusions and recommendations

5.1 Conclusion

Four turbine mooring anchors geometries were designed, manufactured and the impact of the macro-turbulent structures they generated as well as the macro-turbulent structures generated by surface roughness tested on the performance of 19.8 cm diameter scaled turbine in the water tunnel facility. The turbine was first tested in an unobstructed flow velocity of 1.1 m/s, which corresponds to a Reynolds number of 2.17×10^5, based on rotor diameter to determine the optimum performance parameters of the turbine. Thereafter, surface roughness were distributed at the bottom of the water tunnel facility and each of the turbine mooring anchors geometries deployed 2 and 3 rotor diameters upstream of the turbine. The surface roughness and turbine mooring anchors impacted the flow velocity and pattern, generating macro-turbulent structures.

Furthermore, it was observed that turbine mooring anchors impacted turbine performance more when deployed 3 diameters upstream compared to when they were deployed 2 diameters upstream. This is as result obtained from the experiment showed a 14% to 36% improvement in performance with the turbine mooring anchors deployed 3 diameters upstream compared to a 4% to 34% improvement in performance when the mooring anchors were deployed 2 diameters upstream. Also, the deployment of the mooring anchors impacted the flow velocity in water tunnel as result showed a 10% to 27% increase in streamwise velocity in the water tunnel. Result analysis identified the separation distance between the turbine and mooring anchors, mooring anchor geometries and height as well as the size of the surface roughness as the major factors that impacted the turbine performance.

Finally, field measurement at the CHTTC show temporal variation in the velocity and turbulence intensity due to the turbine mooring structures at the CHTTC. Turbine mooring structure causes obstruction, flow separation and changes the flow pattern in the channel. Measurements 15 and 16 length to diameter ratio upstream and downstream, respectively of the turbine mooring structures show the structures create low local velocity deficit around them. The structures also generates vertical turbulent eddies, also referred to as boils in the order of magnitude of the body or object causing them. Away from the obstruction and negative velocity gradient area, eddies and obstruction effects dissipates and flow velocity increases. Deployment of HKTs in this area will result to enhanced power output as result obtained show a 19% increase in power density between measurement locations CP-F and CP-G.

5.2 Recommendations and future work

The following are recommended for further study on impact of macro-turbulent structures and mooring anchors on the performance of a hydrokinetic turbines:

1. An underwater thermal camera would help gain a better understanding of the boil generation and the distance they travel before being seen at the surface.

2. A study on the effects of these turbine mooring structures on a horizontal HKT deployed a yaw position is recommended. This will help to determine the best position and angle for optimum power output.

3. A Particle Image Velocimetry (PIV) test is recommended to help gain better understanding of flow separation phenomenon. The Plexiglass walls of the test section of the water tunnel will support such test.

Bibliography

[1] NOAA, "co2_data_month_avg_ever." [Online]. Available: ftp://aftp.cmdl.noaa.gov/products/trends/co2/co2_mm_gl.txt

[2] U. Nations, "Population division of the department of economic and social affairs of the united nations secretariat," *World population prospects, Report, United Nations, New York*, "2008".

[3] S. D'Auteuil, "Investigation and development of velocity and turbulence measurement techniques for riverine hydrokinetic turbine sites," Master's thesis, The University of Manitoba, 2017.

[4] D. Gaden, "An investigation of river kinetic turbines: Performance enhancemens, turbine modelling techniques, and an assessment of turbulence models," Master's thesis, The University of Manitoba, 2007.

[5] M. Gney and K. Kaygusuz, "Hydrokinetic energy conversion systems: A technology status review," *Renewable and Sustainable Energy Reviews*, vol. 14, no. 9, pp. 2996 – 3004, 2010.

[6] M. Kaltschmitt, W. Streicher, and A. Wiese, *Renewable energy: technology, economics and environment*. Springer Science & Business Media, 2007.

[7] J. A. Fay, "Energy and the environment," Ph.D. dissertation, Oxford University, 2002.

[8] F. Vanek, L. Albright, and L. Angenent, "Energy systems engineering," *Evaluation & implementation*, 2008.

[9] G. Howard, *Energy revolution: policies for a sustainable future.* Washington DC: Island Press, 2002.

[10] S. Bernad, A. Georgescu, S. C. Georgescu, and R.Susan-Resiga, "Flow investigation in archad turbine," *The publishing house of Romanian Academy*, vol. 9, no. 2/2008, pp. 000 – 000, 2008.

[11] R. Summaries, "Energy information administration, office of integrated analysis and forecasting. us department of energy," 2009.

[12] S. Mohammad, "Effect of shroud on the performance of horizontal axis hydrokinetic turbines," Ph.D. dissertation, The University of Manitoba, 2015.

[13] A. H. Birjandi, E. L. Bibeau, V. Chatoorgoon, and A. Kumar, "Power measurement of hydrokinetic turbines with free-surface and blockage effect," *Ocean Engineering*, vol. 69, pp. 9 – 17, 2013.

[14] F. O. Rourke, F. Boyle, and A. Reynolds, "Tidal energy update 2009," *Applied Energy*, vol. 87, no. 2, pp. 398 – 409, 2010.

[15] P. Fraenkel, "Practical tidal turbine design considerations: a review of technical alternatives and key design decisions leading to the development of the seagen 1.2 mw tidal turbine," in *Proceedings-Fluid Machinery Group-Ocean Power Fluid Machinery Seminar*, 2010.

[16] J. Taylor, "Charting the course: Canada's marine renewable energy technology roadmap," Government of Canada, Tech. Rep., 2011.

[17] A. Birjandi, E. Bibeau, and J. Woods, "Investigation of macro-turbulent flow structures interaction with a vertical hydrokinetic river turbine," *Renewable*

Energy, vol. 48, no. 0, pp. 183 – 192, 2012.

[18] M. Khan, G. Bhuyan, M. Iqbal, and J. Quaicoe, "Hydrokinetic energy conversion systems and assessment of horizontal and vertical axis turbines for river and tidal applications: A technology status review," *Applied Energy*, vol. 86, no. 10, pp. 1823 – 1835, 2009.

[19] O. R. E. Coalition, "Us marine and hydrokinetic renewable energy roadmap," *Executive Summary*, 2011.

[20] T. O. R. E. Group, "Canada's marine renewable energy technology road map," *Executive Summary*, 2011.

[21] A. Betz, "The maximum of the theoretically possible exclusion of the wind by wind motors," *magazine for the entire turbine industry*, vol. 26, no. 307-309, p. 8, 1920.

[22] M. Adaramola and P.-Å. Krogstad, "Experimental investigation of wake effects on wind turbine performance," *Renewable Energy*, vol. 36, no. 8, pp. 2078–2086, 2011.

[23] R. Bedard, "Overview of technology classes and key terminology," in *Proceedings of the Hydrokinetic and Wave Energy Technologies Technical and Environmental Issues Workshop. US Department of Energy, Washington, DC*, 2005, pp. 5–8.

[24] S. Yokosi, "The structure of river turbulence," 1967.

[25] G. H. Matthes, "Macroturbulence in natural stream flow," *Eos, Transactions American Geophysical Union*, vol. 28, no. 2, pp. 255–265, 1947.

[26] H. Sutherland and N. Kelley, "Fatigue damage estimate comparisons for northern european and us wind farm loading environments," in *Proceedings of WindPower*, vol. 95, 1995, p. 177.

[27] M. Hand, D. Simms, L. Fingersh, D. Jager, J. Cotrell, S. Schreck, and S. Larwood, "Unsteady aerodynamics experiment phase vi: wind tunnel test configurations and available data campaigns," National Renewable Energy Lab., Golden, CO.(US), Tech. Rep., 2001.

[28] R. J. Barthelmie, K. Hansen, S. T. Frandsen, O. Rathmann, J. Schepers, W. Schlez, J. Phillips, K. Rados, A. Zervos, E. Politis *et al.*, "Modelling and measuring flow and wind turbine wakes in large wind farms offshore," *Wind Energy*, vol. 12, no. 5, pp. 431–444, 2009.

[29] H. G. Beyer, T. Pahlke, W. Schmidt, H.-P. Waldl, and U. de Witt, "Wake effects in a linear wind farm," *Journal of Wind Engineering and Industrial Aerodynamics*, vol. 51, no. 3, pp. 303–318, 1994.

[30] B. Sanderse, "Aerodynamics of wind turbine wakes," *Energy Research Center of the Netherlands (ECN), ECN-E–09-016, Petten, The Netherlands, Tech. Rep*, vol. 5, no. 15, p. 153, 2009.

[31] T. Maeda, T. Yokota, Y. Shimizu, and K. Adachi, "Wind tunnel study of the interaction between two horizontal axis wind turbines," *Wind Engineering*, vol. 28, no. 2, pp. 197–212, 2004.

[32] E. González-Gorbeña, R. Y. Qassim, and P. C. Rosman, "Optimisation of hydrokinetic turbine array layouts via surrogate modelling," *Renewable Energy*, vol. 93, pp. 45–57, 2016.

[33] N. Troldborg, J. N. Sørensen, and R. Mikkelsen, "Actuator line simulation of wake of wind turbine operating in turbulent inflow," in *Journal of physics: conference series*, vol. 75, no. 1. IOP Publishing, 2007, p. 012063.

[34] J. Michelsen, "Basis3d-a platform for development of multiblock pde solvers. report afm 92-05," 1992.

[35] N. N. Sørensen, “General purpose flow solver applied to flow over hills,” Ph.D. dissertation, Technical University of DenmarkDanmarks Tekniske Universitet, Risø National Laboratory for Sustainable EnergyRisø Nationallaboratoriet for Bæredygtig Energi, Wind Energy DivisionAfdelingen for Vindenergi, Aeroelastic DesignAeroelastisk Design, 1995.

[36] J. Mann, “Wind field simulation,” *Probabilistic engineering mechanics*, vol. 13, no. 4, pp. 269–282, 1998.

[37] J. N. Sørensen and W. Z. Shen, “Computation of wind turbine wakes using combined navier-stokes/actuator-line methodology,” in *1999 European Wind Energy Conference and Exhibition*, 1999, pp. 156–159.

[38] R. J. Barthelmie, S. T. Frandsen, M. Nielsen, S. Pryor, P.-E. Rethore, and H. E. Jørgensen, “Modelling and measurements of power losses and turbulence intensity in wind turbine wakes at middelgrunden offshore wind farm,” *Wind Energy*, vol. 10, no. 6, pp. 517–528, 2007.

[39] E. Segergren, “Direct drive generator for renewable power conversion from water currents,” Ph.D. dissertation, Acta Universitatis Upsaliensis, 2005.

[40] S. B. Elghali, M. Benbouzid, and J. F. Charpentier, “Marine tidal current electric power generation technology: State of the art and current status,” in *Electric Machines & Drives Conference, 2007. IEMDC’07. IEEE International*, vol. 2. IEEE, 2007, pp. 1407–1412.

[41] J. Trinnaman and A. Clarke, *2004 Survey of energy resources.* Elsevier, 2004.

[42] H. Ormberg and K. Larsen, “Coupled analysis of floater motion and mooring dynamics for a turret-moored ship,” *Applied Ocean Research*, vol. 20, no. 1-2, pp. 55–67, 1998.

[43] J. H. VanZwieten Jr, M. G. Seibert, and K. von Ellenrieder, “Anchor selection study for ocean current turbines,” *Journal of Marine Engineering & Technology*, vol. 13, no. 1, pp. 59–73, 2014.

[44] J. VanZwieten, F. Driscoll, A. Leonessa, and G. Deane, “Design of a prototype ocean current turbinepart ii: flight control system,” *Ocean engineering*, vol. 33, no. 11-12, pp. 1522–1551, 2006.

[45] P. Fraenkel, “Tidal currents: a major new source of energy for the millennium,” *Sustainable Developments International*, pp. 107–112, 1999.

[46] A. Papanicolaou and C. Kramer, “The role of relative submergence on cluster microtopography and bedload predictions in mountain streams,” in *Proc. Int. Symp River, Coastal and Estuarine Morphodynamics*, 2005, pp. 4–7.

[47] K. B. Strom and A. N. Papanicolaou, “Adv measurements around a cluster microform in a shallow mountain stream,” *Journal of Hydraulic Engineering*, vol. 133, no. 12, pp. 1379–1389, 2007.

[48] A. Papanicolaou, C. Kramer, A. Tsakiris, T. Stoesser, S. Bomminayuni, and Z. Chen, “Effects of a fully submerged boulder within a boulder array on the mean and turbulent flow fields: Implications to bedload transport,” *Acta Geophysica*, vol. 60, no. 6, pp. 1502–1546, 2012.

[49] A. G. Tsakiris, A. T. Papanicolaou, S. M. Hajimirzaie, and J. H. Buchholz, “Influence of collective boulder array on the surrounding time-averaged and turbulent flow fields,” *Journal of Mountain Science*, vol. 11, no. 6, pp. 1420–1428, 2014.

[50] A. T. Jessup, C. C. Chickadel, S. A. Talke, and A. R. Horner-Devine, “Cohstrex: Coherent structures in rivers and estuaries experiment,” *Coherent Flow Structures at Earth’s Surface*, pp. 215–230, 2013.

[51] R. J. Hardy, J. L. Best, S. N. Lane, and P. E. Carbonneau, “Coherent flow structures in a depth-limited flow over a gravel surface: The role of near-bed turbulence and influence of reynolds number,” *Journal of geophysical research: earth surface*, vol. 114, no. F1, 2009.

[52] R. J. Adrian, “Hairpin vortex organization in wall turbulence,” *Physics of Fluids*, vol. 19, no. 4, p. 041301, 2007.

[53] F. Charlton, P. Brown, and R. Benson, *The hydraulic geometry of some gravel rivers in Britain.* Hydraulics Research Station (Great Britain), 1978.

[54] J. Best, “Kinematics, topology and significance of dune-related macroturbulence: some observations from the laboratory and field,” *Fluvial sedimentology VII*, vol. 35, pp. 41–60, 2005.

[55] G. Marquis and A. Roy, “Turbulent processes at the entrance of a pool using flow visualization,” *River Flow 2006*, pp. 109–17, 2006.

[56] A. B. Shvidchenko and G. Pender, “Macroturbulent structure of open-channel flow over gravel beds,” *Water Resources Research*, vol. 37, no. 3, pp. 709–719, 2001.

[57] A. G. Roy, T. Buffin-Belanger, H. Lamarre, and A. D. Kirkbride, “Size, shape and dynamics of large-scale turbulent flow structures in a gravel-bed river,” *Journal of Fluid Mechanics*, vol. 500, pp. 1–27, 2004.

[58] A. Klaven, “Investigation of the flow turbulent structure,” *Trans. State Hydrol. Inst*, vol. 136, pp. 65–76, 1966.

[59] K. Grishanin, “Dynamics of channel flows,” *Gidrometeoizdat, Leningrad*, p. 311, 1979.

[60] S. J. Kline, W. C. Reynolds, F. Schraub, and P. Runstadler, "The structure of turbulent boundary layers," *Journal of Fluid Mechanics*, vol. 30, no. 4, pp. 741–773, 1967.

[61] A. Grass, R. Stuart, and M. Mansour-Tehrani, "Vortical structures and coherent motion in turbulent flow over smooth and rough boundaries," *Phil. Trans. R. Soc. Lond. A*, vol. 336, no. 1640, pp. 35–65, 1991.

[62] I. Nezu, "Turbulence in open-channel flows," 1993.

[63] A. Talmon, J. Kunen, and G. Ooms, "Simultaneous flow visualization and reynolds-stress measurement in a turbulent boundary layer," *Journal of Fluid Mechanics*, vol. 163, pp. 459–478, 1986.

[64] M. S. Yalin, *River mechanics.* Elsevier, 2015.

[65] A. G. Roy, T. Buffin-Belanger, and S. Deland, "Scales of turbulent coherent flow structures in a gravel-bed river," *Coherent flow structures in open channels*, p. 147, 1996.

[66] V. Nikora and G. Smart, "Turbulence characteristics of new zealand gravel-bed rivers," *Journal of Hydraulic Engineering*, vol. 123, no. 9, pp. 764–773, 1997.

[67] V. I. Nikora and D. G. Goring, "Are weakly mobile-bed flows a special class of wall-bounded flows," in *28th Congress of the International Association for Hydraulic Research, Graz, Austria*, 1999, pp. 22–27.

[68] N. Fujisawa and S. Shibuya, "Observations of dynamic stall on darrieus wind turbine blades," *Journal of Wind Engineering and Industrial Aerodynamics*, vol. 89, no. 2, pp. 201–214, 2001.

[69] A. H. Birjandi, J. Woods, and E. L. Bibeau, "Investigation of macro-turbulent flow structures interaction with a vertical hydrokinetic river turbine," *Renewable*

energy, vol. 48, pp. 183–192, 2012.

[70] A. Müller and A. Gyr, "On the vortex formation in the mixing layer behind dunes," *Journal of Hydraulic Research*, vol. 24, no. 5, pp. 359–375, 1986.

[71] J. G. Venditti and B. O. Bauer, "Turbulent flow over a dune: Green river, colorado," *Earth Surface Processes and Landforms*, vol. 30, no. 3, pp. 289–304, 2005.

[72] J. M. Coleman, "Brahmaputra river: channel processes and sedimentation," *Sedimentary Geology*, vol. 3, no. 2-3, pp. 129–239, 1969.

[73] R. Kostaschuk and M. Church, "Macroturbulence generated by dunes: Fraser river, canada," *Sedimentary Geology*, vol. 85, no. 1-4, pp. 25–37, 1993.

[74] C. C. Chickadel, A. R. Horner-Devine, S. A. Talke, and A. T. Jessup, "Vertical boil propagation from a submerged estuarine sill," *Geophysical Research Letters*, vol. 36, no. 10, 2009.

[75] H. J. Sutherland, P. S. Veers, and T. D. Ashwill, "Fatigue life prediction for wind turbines: A case study on loading spectra and parameter sensitivity," in *Case Studies for Fatigue Education*. ASTM International, 1994.

[76] J. G. Leishman, "Challenges in modeling the unsteady aerodynamics of wind turbines," in *ASME 2002 Wind Energy Symposium*. American Society of Mechanical Engineers, 2002, pp. 141–167.

[77] P. Evans, E. D. Lazarus, A. Mason-Jones, D. M. O'Doherty, and T. O'Doherty, "Wake characteristics of a natural submerged pinnacle and implications for tidal stream turbine installations," *INSERT JOURNAL*, 2015.

[78] K. Soto and C. Escauriaza, "Numerical simulations of marine hydrokinetic devices in complex bathymetries," in *Proceedings of the 11th European Wave*

and Tidal Energy Conference, September. Nantes, France, 2015.

[79] A. Wimshurst and R. Willden, "Tidal power extraction on a streamwise bed slope," *Ocean Engineering*, vol. 125, pp. 70–81, 2016.

[80] C. M. García, M. I. Cantero, Y. Niño, and M. H. García, "Closure to turbulence measurements with acoustic doppler velocimeters by carlos m. garcía, mariano i. cantero, yarko niño, and marcelo h. garcía," *Journal of Hydraulic Engineering*, vol. 133, no. 11, pp. 1289–1292, 2007.

[81] A. Nortek, "Adv operation manual," *Vollen, Norway*, vol. 34, 1998.

[82] A. Birjandi, "Effect of flow and fluid structures on the performance of vertical river hydrokinetic turbines," Ph.D. dissertation, The University of Manitoba, 2012.

[83] L. Myers and A. Bahaj, "Power output performance characteristics of a horizontal axis marine current turbine," *Renewable energy*, vol. 31, no. 2, pp. 197–208, 2006.

[84] P.-Å. Krogstad and J. Lund, "An experimental and numerical study of the performance of a model turbine," *Wind Energy*, vol. 15, no. 3, pp. 443–457, 2012.

[85] M. R. Soltani, A. H. Birjandi, and M. S. Moorani, "Effect of surface contamination on the performance of a section of a wind turbine blade," *Scientia Iranica*, vol. 18, no. 3, pp. 349–357, 2011.

[86] A. C. Wilcox and E. E. Wohl, "Field measurements of three-dimensional hydraulics in a step-pool channel," *Geomorphology*, vol. 83, no. 3-4, pp. 215–231, 2007.

[87] M. H. Asgari Kaji, "Turbulent structure in open channel flow," 2013.

[88] J. Mathieu and J. Scott, *An introduction to turbulent flow.* Cambridge University Press, 2000.

[89] C. C. Chickadel, A. R. Horner-Devine, S. A. Talke, and A. T. Jessup, “Vertical boil propagation from a submerged estuarine sill,” *Geophysical Research Letters*, vol. 36, no. 10, pp. n/a–n/a, 2009, l10601. [Online]. Available: http://dx.doi.org/10.1029/2009GL037278

Appendix A

CHTTC details

The CHTTC, located on the Winnipeg River in Seven Sisters Falls, Manitoba is a national centre focused on providing opportunity for HKT developers and manufacturers in collaboration with researchers at the University of Manitoba to test HKTs in a river. The centre from inception has attracted many HKT companies such as New Energy and Clean current with their prototype designs tested at the centre. Deployment and testing of the HKTs at the CHTTC is facilitated by the anchoring and mooring system at the centre. The anchoring and mooring system at the CHTTC is as shown in Figure 1.5. The collaboration between these companies and the researchers at the University of Manitoba have led to enhanced studies on HKT development. Also, the CHTTC offers consulting services to remote communities. Lots of communities still engage in electricity generation using diesel fuel. Such communities and the CHTTC with its personnel equipped to consult, design energy solutions and in partnership with HKT developers can assist in installing HKTs for such communities.

Furthermore, another type of research being done at the CHTTC amongst others is flow measurements using flow measuring instruments such as the ADV, horizontal and vertical acoustic Doppler current profiler, current meter (Valeport), shear probe etc. This research is of interest to the industry partners and the researchers as it will help determine the impact of the flow structures on the performance of the any HKT been tested at the centre as well as when planning a HKT project. With a Hydro dam which prevents debris coming upstream of the river and a large portion of the channel being man-made removing difficulties associated with HKT planning and deployment, the CHTTC channel can be said to be an ideal location for HKT testing and flow measurements.

Finally, with the CHTTC been close to a dam, the flow velocity along the CHTTC channel is a function of the volumetric discharge from the dam. Information on the water level and volumetric flow rate are available on hourly basis and are accessible to CHTTC personnel. The varying discharge flow rate from the dam enables HKTs to be tested at different flow speeds along the CHTTC channel. Figure A.1 shows the different activities at the CHTTC while additional information on the CHTTC can be found in www.chttc.ca.

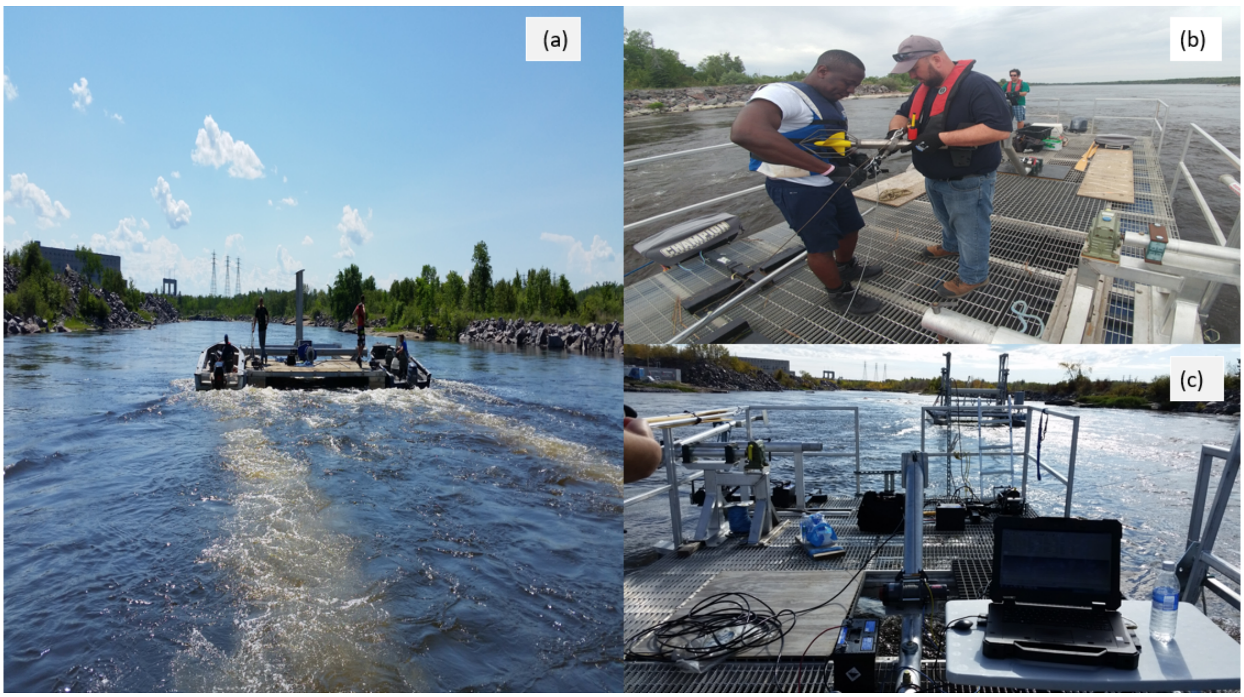

Figure A.1: Different aspects of activities at the CHTTC: (a) testing of New Energy 25 kW HKT at the CHTTC, (b) current meter (Valeport) deployment activity, and (c) flow measurement activity at the CHTTC using acoustic Doppler flow measuring instruments

Appendix B

Fluid mechanics

B.1 Turbine design and operating parameters

The parameters associated with turbine performance or power production from a turbine are grouped into design and operating parameters as shown in Table B.1. These parameters can be further grouped into dimensionless and non-dimensionless parameters.

Understanding these parameters is necessary when comparing fluid flows due to their exhibition of different characteristics, behavioural changes and properties. In order to achieve the desired comparison between different fluid flows, the concept of dimensional analysis is used.

B.1.1 Dimensionless parameters

Dimensionless parameters are introduced when dealing with fluid flows with different characteristics and properties to ensure valid comparison of the fluid flows. Dimensional analysis also helps in the design and manufacturing of small scale turbines by providing geometric or dynamic similarity laws with large scale utility turbines.

Dimensionless parameters are derived by combining two or more parameters and in some cases, two or more dimensionless parameters can be combined to derive a different dimensionless parameter.

Table B.1: Turbine design and operating parameters that should be considered when planning a turbine project

Parameter	**Parameter group**	**Unit**	**Symbol**
Fluid free stream speed	Operating	m/s	U
Fluid density	Operating	kg/m^3	ρ
Turbine diameter	Design	m	D
Rotational speed	Operating	rad/s	
Number of blades	Design		N
Chord length	Design	m	c
Wetted perimeter	Operating	m	P_w
Cross-sectional area	Operating	m^2	A
Turbulence Intensity	Operating		$T.I$
Dynamic viscosity	Operating		μ
Water height	Operating		H
Boundary layer thickness	Operating		δ

A qualitative and quantitative guide to understanding the mechanism of fluid flow can be obtained from dimensional analysis and experiment, respectively. In deriving a dimensionless equation, the terms involved in the equation have to be dimensionally homogeneous[3]. In dimensioning parameters, mass, length and time denoted as M, L and T are often chosen as the fundamental dimensions in deriving every other parameters that may be experienced in a fluid system [3]. Applying these fundamental dimensions, other dimensions can be derived. For example [L^2] and [L^3], are the derived dimensions of area and volume respectively and [] denoting the interest in qualitative rather than quantitative dimensions of the property. Time plays a very important role when dealing with fluid mechanics which leaves

$$Velocity = \frac{Distance}{Time} \tag{B.1}$$

and dimensioned as [LT^{-1}]. Also in fluid dynamics, the basis for derivation of dimension is provided in Newton's second law which states that

$$Force = Mass \times Acceleration \tag{B.2}$$

Where

$$Acceleration = \frac{Velocity}{Time} \tag{B.3}$$

and dimensioning the above equations,

Force = [M][LT^{-1}]/[T];

Force = [MLT^{-2}].

Other parameters encountered in fluid system are dimensioned using this method. A combination of one or two of these groups leads to the formation of dimensionless groups such as Reynolds number, hydraulic radius and Froude number amongst others.

Froude number (Fr) as denoted in Equation B.4 is a member of the dimensionless group in fluid mechanics.

$$Fr = \frac{U_\infty}{\sqrt{gR_h}} \tag{B.4}$$

In determining the type of flow present in an open channel flow, Froude number is an important criterion to consider. It also helps in determining the effects of surface waves and gravity in a fluid. Using Froude number, flow regimes of a flow fluid can be divided into three regimes namely:

- Critical flow- In a critical flow regime, Froude number is equal to one or unity, ($Fr = 1$). This means that the flow is stationary and affected by gravity but in a lesser way compared to super-critical flows.
- Super-critical flows- In this type of flow regime, Froude number is greater than 1, ($Fr > 1$). Flows in this type of regime experience gravitational effects more than critical flows and are characterized by fast fluid motion.
- Sub-critical flow- Sub-critical flows experience Froude number been less than 1, ($Fr < 1$). Gravitational effects are not experienced by flows in such regime and they are characterized by deep fluid motion as against super-critical flows.

Reynolds number is one of the most used dimensionless group member in fluid mechanics. As denoted in equation B.5, it is defined as ratio of a fluids viscous force to its inertial force. Reynolds number helps to determine which regimes: Laminar or Turbulent, a fluid flow belongs to amongst other fluid qualities.

$$Re = \frac{\rho R_h U_\infty}{\mu} \tag{B.5}$$

where ρ = fluid density R_h= hydraulic radius U_∞ = Free stream velocity μ = Dynamic viscosity

With ρ and μ in Equation B.5 above, kinematic viscosity ν , which is denoted as

$$\nu = \frac{\mu}{\rho} \tag{B.6}$$

can be introduced in Equation B.5 above to have an abridged Reynolds number Equation as

$$Re = \frac{R_h U_\infty}{\nu} \tag{B.7}$$

Other dimensionless group members in fluid mechanics that are important in hydrokinetic turbine performance are as listed in table B.2.

Table B.2: Other dimensionless parameters that should be considered when planning a turbine project

Parameter	Symbol	Definition
Aspect ratio	AR	$\frac{L}{2r}$
Preset pitch angle	α_p	–
Solidity	σ	$\frac{Nc}{2r}$
Tip Speed Ratio	λ	$\frac{\omega r}{U}$
Blade Reynolds number	Re_B	$\frac{\rho_c U}{\mu}$
Clearance coefficient	C_λ	$\frac{H}{L}$
Turbine Reynolds number	Re_D	$\frac{2N \times Re}{\sigma}$
Blade relative Reynolds number	Re_{rel}	$Re \times \lambda$